BULLETIN OF RSMU

JUL-AUG 2016 (4) ISSN 2500-1094
VESTNIKRGMU.RU

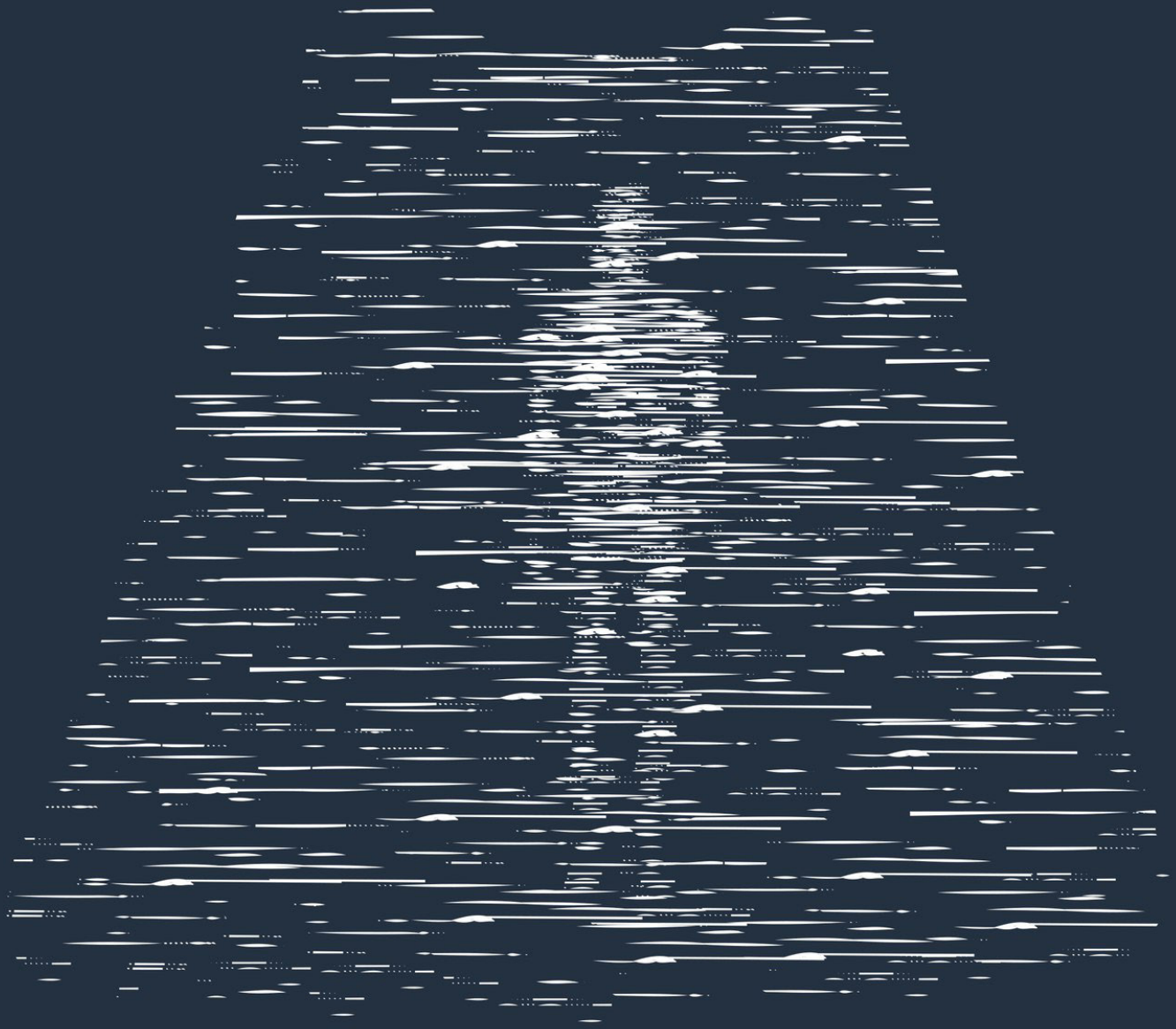

MEDICAL IMAGING REVIEW

BULLETIN OF RUSSIAN STATE MEDICAL UNIVERSITY

Scientific Medical Journal of Pirogov Russian National Research Medical University

ВЕСТНИК РОССИЙСКОГО ГОСУДАРСТВЕННОГО МЕДИЦИНСКОГО УНИВЕРСИТЕТА

Научный медицинский журнал Российского национального исследовательского медицинского университета имени Н. И. Пирогова

The journal is included in the list of the leading peer-reviewed scientific journals and publications approved by the Higher Attestation Commission

The journal is available in Google Scholar.

IF RSCI 2014: 0,134.

Approved for print June 30, 2016.

Address: ul. Ostrovityanova, d. 1, Moscow, Russia, 117997
For papers submission: editor@vestnikrgmu.ru
For collaboration: manager@vestnikrgmu.ru

The mass media registration certificate no. 012769 issued on July 29, 1994
Subscription index in the Rospechat catalog: 46826
Printed by Premium Print
www.premium-print.ru

BULLETIN OF RSMU 4, 2016
ВЕСТНИК РГМУ

CONTENTS
СОДЕРЖАНИЕ

LOOKING INSIDE MAN: MEDICAL IMAGING

Osipov LV[1,a], Dolgushin MB[2,b], Mikhaylov AI[2,b], Epel B[3,c], Rumyantsev KA[4,5,d], Turoverov KK[4,d], Verkhusha VV[5,d], Kulikova EYu[6] ✉

[1] IzoMed Ltd., Moscow, Russia

[2] Department of Positron Emission Tomography,
N. N. Blokhin Russian Cancer Research Center, Moscow, Russia

[3] Department of Radiation and Cellular Oncology,
University of Chicago, Chicago, USA

[4] Laboratory of the Structural Dynamics, Stability and Folding of Proteins,
Institute of Cytology of Russian Academy of Sciences, Saint-Petersburg, Russia

[5] Department of Anatomy and Structural Biology,
Albert Einstein College of Medicine, New York, USA

[6] Pirogov Russian National Research Medical University, Moscow, Russia

[a] ultrasound technologies; [b] tomographic technologies; [c] oximetry; [d] fluorescence imaging

The rapid progress of medical sciences has brought about novel effective medications, new techniques that make surgery less traumatic, artificial materials that serve to replace tissues and organs, and robotic prostheses. Still, treatment success is largely a question of timely and accurate diagnosis and proper patient monitoring. Here, various imaging techniques come in handy. Those are often thought of as tools for anatomy visualization, but in fact, they are often highly effective for the assessment of the functional state of organs and tissues. Imaging techniques are so diverse that it is impossible to cover them all in one review. Therefore, we have decided to touch upon the most common and interesting ones, such as ultrasound imaging, tomography, oximetry and fluorescence imaging.

Keywords: ultrasound imaging, computed tomography, magnetic resonance imaging, positron emission tomography, oximetry *in vivo*, fluorescence imaging *in vivo*

✉ **Correspondence should be addressed:** Elena Kulikova
ul. Ostrovityanova, d. 1, Moscow, Russia, 117997; elena.yu.kulikova@gmail.com

Received: 15.08.2016 **Accepted:** 20.08.2016

ЗАГЛЯНУТЬ В ЧЕЛОВЕКА: ВИЗУАЛИЗАЦИЯ В МЕДИЦИНЕ

Л. В. Осипов[1,a], М. Б. Долгушин[2,b], А. И. Михайлов[2,b], Б. Эпель[3,c], К. А. Румянцев[4,5,d], К. К. Туроверов[4,d], В. В. Верхуша[5,d], Е. Ю. Куликова[6] ✉

[1] ООО «ИзоМед», Москва

[2] Отделение позитронной эмиссионной томографии,
Российский онкологический научный центр имени Н. Н. Блохина, Москва

[3] Отделение радиологии и клеточной онкологии,
Университет Чикаго, Чикаго, США

[4] Лаборатория структурной динамики, стабильности и фолдинга белков,
Институт цитологии РАН, Санкт-Петербург

[5] Отдел анатомии и структурной биологии,
Колледж медицины имени Альберта Эйнштейна, Нью-Йорк, США

[6] Российский национальный исследовательский медицинский университет имени Н. И. Пирогова, Москва

[a] раздел по ультразвуковым технологиям; [b] раздел по томографическим технологиям; [c] раздел по оксиметрии; [d] раздел по флуоресцентной визуализации

Медицина развивается стремительно: разрабатываются новые более эффективные препараты, предлагаются все менее травматичные способы оперативных вмешательств, а для замещения тканей и органов используются искусственные материалы и управляемые протезы. Однако по-прежнему успех лечения во многом определяется своевременным и точным диагностированием заболевания, а также адекватным мониторингом эффективности терапии. Эти задачи решают с применением различных технологий визуализации. Многие ассоциируют их с представлением анатомических структур тела, но в действительности гораздо чаще они позволяют определить функциональное состояние тканей и органов. Разнообразие технологий визуализации велико, и описать их все в одной работе не представляется возможным, поэтому для настоящего обзора были выбраны наиболее распространенные и интересные из них: ультразвуковые и томографические технологии, прижизненная оксиметрия и флуоресцентная визуализация.

Ключевые слова: ультразвуковая визуализация, компьютерная томография, магнитно-резонансная томография, позитронно-эмиссионная томография, оксиметрия *in vivo*, флуоресцентная визуализация *in vivo*

✉ **Для корреспонденции:** Куликова Елена Юрьевна
117997, г. Москва, ул. Островитянова, д. 1; elena.yu.kulikova@gmail.com

Статья поступила: 15.08.2016 **Статья принята к печати:** 20.08.2016

Ultrasound imaging

Ultrasound imaging (USI) is one of the most popular medical imaging techniques. Among the basic operating modes of ultrasound scanners are a two-dimensional B-mode for obtaining grayscale images and various Doppler modes. The latter include a spectral Doppler for blood flow measurements and a two-dimensional color flow mapping that provides information on the hemodynamics in vessels and the heart. Tissue Doppler is used for monitoring moving heart structures (the left ventricle, in the first place). In certain areas of application, ultrasound imaging in B-mode may seem less informative, compared to other visualization techniques, but Doppler scans have a huge advantage here, as they allow obtaining information in real time.

The basic ultrasound modes are constantly evolving. For better visualization of malignant tumors and other blastomas, B-mode elastography is being gradually introduced into clinical practice. It maps tissue stiffness in the scanned area for further comparison. There are two approaches to stiffness evaluation. The first one is compression-based; a compressive force is applied to the scanned area (such as breasts or the prostate gland), and ultrasound images before and after compression are compared. The second technique makes use of shear waves generated after slight tissue compression or by a pushing acoustic pulse in a prescribed direction [1, 2]. Both approaches have their own advantages, and premium-class ultrasound machines support both of these modes.

A major drawback of Doppler techniques is that they are angle-dependent, which may cause artifacts and hinder interpretation of blood flow and cardiac motion images. To overcome this limitation, new methods are being actively developed. For example, a vector image of blood flow in the heart was successfully obtained using complex processing algorithms for Doppler scans of blood flow and left ventricular wall movements.

Non-Doppler imaging is also evolving, including a B-flow technique and speckle-tracking echocardiograpy. The former is used for blood flow visualization and detection of plaques in blood vessels, while the latter assists in analyzing the motion of heart tissues [1].

Transducers for ultrasound scanners

High image quality is extremely important in USI, especially when studying deep tissues or working with complicated cases. Surveys of European ultrasonographers have revealed that most of them are not satisfied with the image quality of their scanners [3]. Here, development of novel transducers for ultrasound scanners can be a solution.

Matrix arrays are becoming increasingly popular. Unlike conventional transducers that make use of a one-dimensional array of piezoelectric elements, whose number n varies from 64 to 256, matrix transducers have a two-dimensional array of n x m active elements. They allow for controlled focusing during transmission and continuous focusing during reception in both the scan plane and the one perpendicular to it, thus forming a narrow beam of transmitted pulses and condensed diagram for received echoes from all scanned depths and improving contrast resolution. High 3D scanning rate and a capability to produce 4D images (3D in real time) by generating several acoustic beams at a time are crucial for full matrix array transducers [1]. The resulting volumetric images can be further used by cardiologists, gynecologists, obstetricians and surgeons.

Another promising approach to transducer manufacturing makes use of monocrystal transducers in which piezoceramics is replaced with artificial crystals; they exhibit better performance and allow for deeper scanning and higher resolution.

Micro-electro-mechanical systems (MEMS) are a conceptually different basis for transducer manufacturing. For example, piezoelectric micromachined ultrasound transducers (pMUT) contain tiny matrix arrays of miniature elements and can be used for transesophageal echocardiography; microsized matrix arrays find their application in high-frequency catheter probes designed to obtain volumetric images of internal heart structures. Another method (Capacitive micro-fabricated ultrasound transducers, cMUT) makes use of capacitive elements with a flexible membrane that improve transducer sensitivity and resolution [4].

Transmit and receive units

A key requirement for modern ultrasound scanners is a wide bandwidth of transmit/receive frequencies that allows for short pulses and, subsequently, a higher resolution in B-mode and color Doppler modes. But as the frequency increases, the tissues attenuate the signal more and the imaging depth decreases. The problem could be solved by increasing pulse energy, but it is not safe. To overcome this limitation, “complex” signals can be used, such as encoded pulse sequences. They are long and allow for larger scan depth in case of high-frequency probes; owing to the compression algorithm, high resolution capacity is retained.

Multi-angle imaging is increasingly used in high-class scanning systems that repeatedly scan one particular area at changing beam angles. Then, the obtained images are summed up for better contrast resolution, more accurate tissue differentiation and clearer visualization of organ borders. Obviously, the frame rate does not benefit here and decreases by the number of projections used.

Adaptive modes and automated measurements

The variety of operating modes and settings available for ultrasound imaging is unsurpassed. Clinicians are looking forward to ultrasound machines that would be easy to operate, especially paramedics and general practitioners who use this imaging technique for bedside testing (the so-called point-of-care applications). Manufacturers offer different preset modes in which settings are selected automatically depending on a diagnostic task or a scanned organ. Ultrasound machines can automatically select continuous focusing in the reception mode and frequency depending on the scan depth, maintain the same level of mappable maximum echo intensity at various depths, evaluate some important diagnostic parameters and subsequently compute diagnostic indices, measure intima-media thickness, etc.

A good example of an adaptive mode that considerably improves image quality is automated evaluation of sound propagation speed in the scanned area used later for image formation. Unlike focusing in the reception mode, continuous focusing in the transmission mode is normally impossible. Synthetic aperture ultrasound is an advanced technique that allows for dynamic focusing at transmission and forms an image after the incoming data are postprocessed [1]. The synthetic aperture technique provides higher image resolution without reducing the frame rate.

Automated measurements and computations make the work of the ultrasonographer much easier and are already

employed in cardiology, angiology, obstetrics, urology and other medical fields. However, they demand exceptional image quality. Most often, high contrast resolution and distinct contours are a must for accurate measurements. For example, special radiofrequency techniques are used for fine measurements of arterial diameter changes to assess vascular elasticity and evaluate intima-media thickness, which is important in monitoring atherosclerosis progression.

Tomography

Discovered in 1895, X-radiation was long a basis for all radiology techniques and is still used for obtaining planar images in roentgenography, mammography and fluoroscopy. The next evolutionary step in the development of medical imaging was tomography, a method based on obtaining cross-sectional images of internal structures of the scanned object by simultaneous translation of the X-ray tube and the plate (detector). The image quality remained poor until Godfrey Hounsfield and Allan Cormack invented computed tomography in 1969–1971. A combination of computer technologies and the X-ray left the planar images far behind.

Computed tomography

Computed tomography (CT) is a noninvasive technique for cross-sectional imaging based on the measurement of X-ray attenuation in tissues of various densities and complex mathematical (computer) processing of the collected data. CT is currently the most common tomography technique for human body scanning.

The evolution of CT is connected with the increasing number of detectors and simultaneously captured projections, that makes the procedure faster and expands scanning area per rotation. Early scanners utilized a step-by-step principle with one rotation of the X-ray tube per slice and a single X-ray tube interacting with one (first generation scanners; processing time of 4 minutes per slice) or several (second generation scanners; processing time of 20 seconds per slice) detectors [1]. Then, helical computed tomography was introduced (HCT; third generation scanners): the tube and the detectors simultaneously completed one clockwise rotation per table increment making the scanning procedure shorter. Further increase in the number of detectors and superimposition of layers substantially reduces imaging time and improves quality of reconstructed images [5].

Fourth generation scanners (multislice spiral computed tomography (MSCT) have several rows of stationary detectors attached to a ring (gantry). The X-ray tube rotates at high speed (up to 0.33 seconds per rotation) sending out a modified-shape beam to the multiple detector rows (up to 320 detector rows can simultaneously capture multiple cross-sections). Widely used premium-class scanners have 64 or 128 rows of detectors, while standard scanners used in clinical routine have 16 to 32 detector rows. After manufacturers stopped the “who can install more detectors” race, they turned to improving the techniques for image reconstruction, which determined further MSCT evolution. Unlike SCT, MSCT is capable of generating isotropic images of submillimeter-thick sections (0.5 mm) and retaining their quality during the subsequent reconstruction in different planes and correction of density data. This inspired the development of virtual endoscopy techniques, such as virtual colonography and bronchoscopy, that provide for highly accurate endoscopic images and can be used to perform virtual intravascular endoscopy, given that improved data postprocessing techniques are available [6].

Owing to higher scan rates, we can now assess the accumulation dynamics of radiographic contrast agents using higher spatial resolution. CT-angiography is almost in no way inferior to a direct angiographic examination, but in contrast to it, is noninvasive. Today, it is not only a routine technique for the evaluation of various blood flow defects (stenosis, aneurisms, total occlusions), but also a tool for the detection of vessel wall abnormalities (atherosclerotic plaques) where direct angiography is not an option. Using modern reconstruction techniques, we can obtain high-quality images at low absorbed radiation doses [7].

CT-perfusion makes use of tissue density measurements after intravenous administration of a radiographic contrast agent. The incoming data are mathematically processed and a number of blood flow parameters are calculated, the major being velocity, volume and time. Several methods can be applied to analyze a time-dependent profile of contrast agent concentration and evaluate tissue hemodynamics. A variety of obtained hemodynamic characteristics serve to differentiate between benign and malignant tumors, detect iatrogenic changes, grade tumor malignancy and estimate the extent of organ damage in patients with blood circulation disorders [8].

Of particular interest is dual energy CT that employs two X-ray sources, as its name implies. For heart scans (the heart is an object in motion), acquisition time is very short and must be synchronized with the cardiac rhythm. In MSCT, the minimal time required to collect all data from a non-moving slice (tube rotation time of 0.33 seconds) is 173 seconds, which means that tube half-turn provides for a sufficient temporal resolution in patients with normal heart beat (65-80 beats per second). However, patients with cardiac pathology often have elevated heart rates and are arrhythmic. Two X-ray tubes positioned at a 90° angle ensure a 83-second temporal resolution, which is a quarter of the tube full turn. Thus, obtaining high-quality images of the heart becomes possible even in patients with elevated heart rates [9].

Dual energy scanners have another important advantage: each tube can switch between different voltages and currents. Coupled with complex computations, such design ensures a better differentiation between tissues with similar densities, reduces the number of artifacts caused by nearby objects of various densities (improves quality of angiographic images and visualization of vascular flow and neoplasms located close to bones or metal implants), and allows for contrast enhancement quantification without native imaging. Tissues absorb radiation differently in the presence of iodinated contrast agents, which explains the effects listed above, while absorption properties of hydroxyapatites (a bone mineral) and metals do not change [10].

There are methods of computer data processing that can determine content of various salts in the scanned area by measuring changes in its absorption properties at different energy levels. They have already found their application in clinical routine, e.g., in the diagnosis of gout based on determining monosodium urate depositions [11].

Magnetic resonance imaging

Magnetic resonance imaging (MRI) is s a technique that uses the phenomenon of nuclear magnetic resonance for visualization of internal organs and tissues. The method is based on measuring the atomic nuclei electromagnetic response (hydrogen nuclei in most cases) excited by various

combinations of electromagnetic waves in a static magnetic field (0.5–3.0 Tesla) [12, 13].

MRI was initially used for brain scans (it is still the "gold standard" in neuroimaging) and was later employed to visualize other body regions. Advances in virtual coil emulation methods that use individual elements of surface coils allowed for automatic expansion of scanning areas to larger anatomic regions, including the whole body. In case of a whole-body MRI, a moving table and built-in receiver coils makes manual repositioning of the patient unnecessary [13].

Unlike CT, MRI does not expose patients to ionizing radiation and provides higher resolution for soft tissue scans, one of the reasons being its ability to suppress a signal from some tissue types. Organ-specific magnetic resonance contrast agents (gadoxetic acid for liver scans or superparamagnetic iron oxide nanoparticles for lymph node imaging) make MRI a "molecular"-oriented imaging technique, just like positron emission tomography (PET) [12, 13].

Diffusion-weighted imaging (DWI) is a form of MRI based on recording mobility (the area a particle covers per unit time) of protons labeled with radiofrequency pulses. This method allows for a semiquantitative evaluation of random Brownian motion (temperature-dependent migration) of water molecules in the body. Using DWI, we can assess the integrity of cell membranes and the intercellular matrix. DWI has found its application in the diagnosis of acute cerebral ischemias, such as acute and peracute stroke, where a CT scan is not an option. DWI is extensively used for the differential diagnosis of brain tumors and demyelinating diseases; whole-body DWI is a highly effective and sensitive method of cancer staging and a good screening technique for individuals at high risk for cancer or its relapse (combined with PET-CT, DWI reduces the radiation dose a patient is exposed to) [14].

DWI has also found its application in tractography. By measuring diffusion tensor, we can calculate its direction; then, upon collecting data on the geometric structure of tissues, we can understand in which direction large bundles of nerve and muscle fibers run. This information is valuable if a surgical treatment of brain and spinal cord tumors is planned or possible neurological risks must be assessed [15].

Magnetic resonance spectroscopy (MRS) is a technique that provides information on tissue biochemistry by measuring concentrations of different metabolites. For MRS, any nucleus with an odd atomic number can be used, though the best signal is generated by hydrogen nuclei. The technique was first suggested in the 1970s, but its evolution was long inhibited by the lack of adequate equipment [16]. Since MRS has strict requirements for field heterogeneity and is highly sensitive to organ motion, it is mostly used for brain and prostate gland scans. It is known that metabolic imbalances in tissues occur prior to clinical manifestations of the disease; because of that, MRS data can assist in the early diagnosis [17]. Owing to improved data processing algorithms, it is now possible to convert standard spectroscopy data to metabolic maps of large brain regions [18].

Magnetic resonance angiography (MRA) is used to visualize blood vessels anatomy and assess functional specifics of blood circulation. This technique is based on differentiating between signals from moving blood protons and static surrounding tissues. MRA allows obtaining vessel images without administering contrast agents to the patient [19].

A relatively new technique for the assessment of hemodynamics and perfusion of brain matter is perfusion MRI. It is more beneficial than CT-perfusion as it does not use X-radiation and does not need contrast agents for enhanced images, which is very important when performing scans on children [8, 20].

Functional MRI (fMRI) is a technique for mapping cortical activity of the brain; it can be used to examine individual anatomy/features of a patient's brain and image regions responsible for motion, vision, speech, memory and other high cortical functions. This technique registers increased blood flow in activated cortex areas [21].

Imaging capacities of modern MR scanners have offered a perfect solution to the problem of brain anatomy visualization (including blood and cerebrospinal fluid flow) and to some extent now assist in the assessment of brain functional state.

Positron emission tomography

PET was first introduced into clinical practice more than 30 years ago and was primarily used in neurology and cardiology. Since the 2000s, it has been in increasing demand in oncology: over 90 % of all PET scans are performed on cancer patients [22].

The physical principle behind this technique is registration of emission from a radiopharmaceutical (RF) accumulated in tissues. Healthy and pathologic tissues accumulate RFs differently depending (though not exclusively) on their functional state. The most common RF is ^{18}F-fluorodeoxyglucose (^{18}F-FDG) [22]. A combination of radionuclide technologies and tomography (PET-CT, PET-MRI) improves spatial visualization of anatomic structures and yields a wealth of information on tumor metabolism, thus solving a number of medical tasks. Those include early detection of disease progression or the spread of neoplasms, assessment of tumor response to treatment, differentiation between malignant and benign tumors and non-neoplastic lesions [23]. Figure 1 shows contribution of various imaging methods to the diagnosis of non-Hodgkin lymphoma [24].

^{18}F-FDG PET has proved to be highly effective in the diagnosis of lung, esophageal and colorectal cancers, head and neck tumors. An ^{18}F-FDG PET-CT scan is a "gold standard" in the diagnosis of melanoma and lymphomas and in screening for occult primary lesions in patients with metastatic cancer. Ordering an ^{18}F-FDG PET scan for patients with well-differentiated breast cancer (BC), thyroid, pancreatic, ovarian or testicular cancers and sarcomas is disputable [20]. In case of kidney, prostate or bladder cancer, hepatocellular carcinomas and neuroendocrine or brain tumors, ^{18}F-FDG PET is not quite informative, which can be compensated for by using other RFs. We are providing some examples below.

In case of brain tumors, the most commonly used radiotracers are those with negligible accumulation in the intact brain matter that reflect amino acid metabolism. The most popular RF is ^{11}C-methionine; it exhibits an almost 90% specificity in the diagnosis of intracranial tumors. ^{18}F-fluoroethyl-tyrosine is a next-generation radiotracer with a longer half-life; therefore, it can be used for a wider range of tasks. ^{18}F-thymidine reflects the dynamics of DNA assembly and helps to assess cell proliferation in tumors treated with anticancer drugs. A very interesting formulation is ^{11}C-sodium butyrate, a fatty amino acid with unique properties that allows for the assessment of both tumor hemodynamics (the extent of vascularization) and its metabolism [25]. Choline-containing agents labeled with ^{11}C or ^{18}F provide information on the formation of membrane complexes (phospholipids) and acetylcholine receptors. It is known that fast renewal and formation of cell membranes are typical for rapidly growing malignant tumors, and the pattern of RF accumulation can reflect this process [26].

When ordered for patients with breast cancer, PET does not play a role of the initial diagnostic procedure, but is used to assess biological activity of the initial neoplasm, detect regional and distant metastases and local recurrences and estimate treatment efficacy; for these purposes, PET is normally enhanced with ^{18}F-FDG [27]. However, some BC types are better detected with ^{18}F-fluoroestradiol that has affinity to estrogen receptors. Another RF, ^{18}F-Galacto-RGD, helps to visualize invasive ductal carcinomas and is used when a planned treatment includes angiogenesis inhibitors [28].

As a prostate cancer diagnostic tool, ^{18}F-FDG PET-CT exhibits limited efficacy, because ^{18}F-FDG is accumulated in the benign hyperplastic tissue of the gland. ^{18}F-choline and ^{11}C-choline that have become quite popular over the past few years are used instead. A PET-CT scan enhanced with choline-containing agents serves to detect cancer recurrences after radiation therapy, brachytherapy and prostatectomy (in case of a biochemical recurrence), as these treatments can seriously affect MRI results [29]. PET-CT is effective for verifying the diagnosis of regional prostate cancer and detecting metastases in regional lymph nodes. To detect distant metastases (bone metastases in particular), a number of examinations are normally carried out, including the whole body MRI, bone scintigraphy, liver ultrasound scanning and some others; conveniently, PET-CT can replace all of them [30]. Choline-containing radiotracers are not the only RFs assisting in prostate cancer diagnosing. Another novel PET tracer is ^{18}F-fluoro-dihydrotestosterone (FDHT). ^{18}F-FDHT PET rely on the increased expression of androgen receptors typical for both cancer and normal cells of the prostate gland [31]; therefore, it would be a better option to use FDHT for treatment monitoring but not for diagnosing primary prostate cancer. ^{68}Ga-PSMA is a radiotracer derived from a prostate-specific membrane antigen. It is highly specific and can be used if treatment with radioactive Y-90- or Lu-177-PSMA is planned [32].

Sensitivity of ^{18}F-FDG PET is too low to diagnose neuroendocrine tumors of various localization. Here, other RFs are employed: ^{18}F-luoro-L-dihydroxyphenylalanine, ^{11}C-hydroxy-L-tryptophan and somatostatin receptor ligands labeled with ^{68}Ga (^{68}Ga-DOTA-TOC, ^{68}Ga-DOTA-NOC, ^{68}Ga-DOTA-TATE) [33]. Comparative efficacy studies of scintigraphy and PET enhanced with similar peptides demonstrate high sensitivity and specificity of the latter, while a combination of PET and CT makes the procedure more informative [34].

If there is a suspicion of bone metastases, ^{18}F-NaF (sodium fluoride) can be used for PET-CT instead of ^{18}F-FDG. Its diagnostic value is similar to that of 99mTc-exametazime used for SPECT. A significant advantage of ^{18}F-NaF-PET-CT over bone scintigraphy is a lower radiation dose and higher spatial resolution, makes it possible to detect even the smallest metastases in the bones [35].

EPR oximetry in spectroscopy mode *in vivo*

Electron paramagnetic resonance (EPR) imaging is a rapidly evolving technique for visualization of spatial distribution of paramagnetic centers (PCs), molecules with unpaired electrons, spin labels and spin probes (SPs), and exploration of their kinetic properties, spectral parameters and relaxivity. EPR imaging is similar to magnetic resonance imaging; however, it has its own unique features [36]. For example, EPR imaging makes use of a 658 times weaker magnetic field, which eliminates the need for expensive superconducting magnets. Spatial distribution of PCs is detected using a linear magnetic field gradient G superimposed on the static magnetic field B_0. An additional magnetic field applied to PCs allows encoding their position.

High concentrations of PCs are rarely found in nature; therefore, EPR imaging employs various spin probes to obtain images. Depending on the problem PCs are synthesized for, they can be sensitive to various chemical and physical factors: viscosity, temperature, pH, redox potential and pO_2 partial pressure. PCs are administered intravenously or intra-arterially; in some cases, such as in monitoring malignant tumors, they are injected straight into the area of interest. Probes easily enter the intercellular volume and are cleared from the body in 10–50 minutes [37].

Oximetry is a major application area for modern EPR imaging. Molecular oxygen is essential for maintaining cellular balance. To function normally, tissues need adequate oxygen supply. Based on O_2 levels, a wide variety of conditions can be diagnosed. When dealing with cancers, it is important to know spatial distribution of oxygen in the tumor, because pO_2 levels

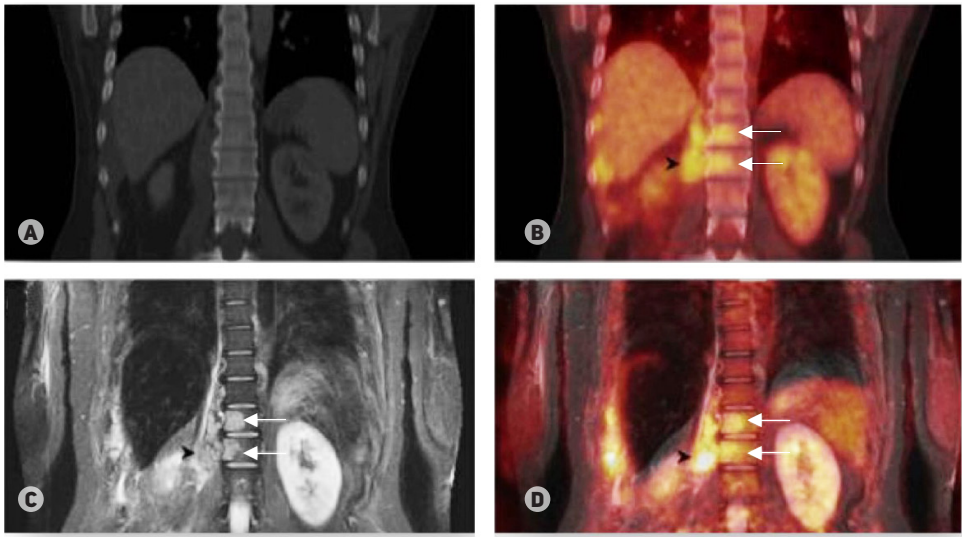

Fig. 1. Non-Hodgkin lymphoma spread to the bone marrow. Computed tomography in the bone window **(A)** detects paravertebral tumor masses, but does not see lesion-infiltrated vertebrae, while magnetic resonance imaging (C) can detect these lesions (shown by arrows) confirmed by hybrid technologies: PET-CT **(B)** and ^{18}F-fluorodeoxyglucose-enhanced PET-MRI **(D)**. Thus, MRI is more sensitive in the diagnosis of bone marrow lesions and detects the first signs of bone destruction and plasma cell infiltrates before osteoclast hyperstimulation can be observed (Buchender et al. [24])

largely determine tumor sensitivity to radiation or chemotherapy [38, 39]. Development of more accurate methods for pO_2 visualization in tissues can greatly widen the range of the targeted treatment applications in biology and medicine [40].

Recent advances in EPR oxymetry are linked to the use of triarylmethyl radicals as spin probes with narrow EPR lines, which contributes to the improvement of the image spatial resolution (0.5–1.0 mm) [41]. The SP rates of longitudinal (spin-lattice) and transverse relaxation are linearly dependent on pO_2 and allow detecting pO_2 levels with a 1 mmHg precision. The major drawback of this technique is that it requires SPs that have not yet been approved for clinical use.

To demonstrate practical application of EPR oximetry, we are providing the results of a study by Epel et al. [42] below. It was a preclinical study of oxygen-guided spatially modulated radiation therapy of tumors. The experiment was carried out on mice with a grown fibrosarcoma. The idea behind the study was as follows: lethal radiation dose for well-oxygenated malignant tissues is 3 times lower than for tissues with < 10 mmHg pO_2, therefore radiation dosage for different tumor regions can be varied. The radiation plan was delivered in two steps. First, 30 % tumor control dose (TCD_{30}) was delivered to the whole tumor. This dose is sufficient to kill well-oxygenated tumor cells with 99 % probability. Then, an additional dose boost was delivered to hypoxic tumor regions resistant to radiation. The cumulative radiation dose for these regions was comparable to TCD98. The second step required submillimeter precision of radiation delivery. In this study, treatment was delivered using a novel animal radiation therapy system (XRAD225Cx micro-CT/radiation therapy delivery system) and a set of 5 beams projecting at different angles. The beams were shaped using tungsten-infused plastic blocks printed on a 3D printer. Figure 2 shows stages of their fabrication based on EPR imaging data. Beam calculations take only 30 minutes after EPR data have been obtained. Time between EPR measurements and radiation therapy onset is critical here, as tissue oxygenation levels can change. Preliminary studies have demonstrated high efficacy of this technique.

Last year, National Institutes of Health, USA, funded pioneer clinical trials in which EPR oximetry in spectroscopy mode was used to predict radiation treatment efficacy. The success of the project and the inspiring results of our work have paved the way for the introduction of this technique into clinical practice. An EPR imager is a simple device and can be easily integrated into standard irradiators for better cancer treatment.

Fluorescence imaging

Fluorescence imaging is a universal technique for the analysis of various biological systems, from single molecules to whole organisms. Over the past two decades, the use of GFP-like fluorescent proteins (FPs) has made it possible to image dynamic processes inside cells and subsequently advanced the development of novel microscopy techniques. Currently, researchers are focusing on the development of genetically encoded optical biomarkers with near-infrared (NIR) light absorption and emission spectra in the so called 650–900 nm “optical window” of living tissues, where light is no longer absorbed by the hemoglobin of red blood cells and skin melanin, and is not yet absorbed by water molecules. Such properties are important for noninvasive imaging of dynamic processes occurring in deep tissues of mammals. Novel fluorescent biomarkers can find their application in basic research in biology and medicine, since they can replace X-ray in certain cases. However, attempts to obtain GFP-like FPs that would satisfy the spectral requirements described above have so far been unsuccessful.

The use of bacterial phytochrome complexes with biliverdin (BV, a product of heme catabolism present in animal and human tissues) as fluorescent biomarkers has proved to be the solution. Over the last few years, a number of bacterial phytochrome-based NIR FPs have been obtained capable of permanent fluorescence, photoactivation or split-system formation [43–48].

Specifically, NIR FPs of the iRFP family allowed for the visualization of small tumors during early stages and investigation of their growth and metastasis in model organisms [43, 49]. iRFP713 was successfully used for monitoring tumors located in deep organs, such as liver, prostate gland, brain, and intraosseous tumors [50]. Fluorescence imaging combined with computed tomography was used to observe inflammatory breast cancer progression and formation of its metastases in lymph nodes [51] and to detect migration pathways of melanoma cells [50].

NIR FPs have a great potential as biomarkers for preclinical studies of anticancer drugs and for visualization of tumor regression and recurrence upon treatment [52].

The ability to image labeled cells across the whole body of an animal makes NIR FPs promising biomarkers for stem cell research. Labeling cardiac progenitor cells with iRFP713 protein allowed for the visualization of myocardial repair in ischemic mice [53]. The ability of transplanted iRFP713-labeled bone marrow cells to restore haematopoiesis in X-ray irradiated mice was also shown [54].

Zero cytotoxicity of iRFP proteins encourages their use for labeling of not only individual cell lines or organs, but the whole organisms. Recently, a line of transgenic mice has been obtained with high expression of iRFP713 protein in all tissues and organs, including brain, heart, lungs, liver, kidneys, spleen, pancreas, thymus, bone and adipose tissue [54]. iRFP713 expression in the primary culture of hippocampal and retinal neurons of mice helped to visualize neurons and characterize their metabolism [55].

NIR FPs ability to effectively bind endogenous BV in protozoa is instrumental in testing novel antiparasitic drugs ex vivo and *in vivo* during preclinical studies. iRFP713-expressing cells of several *Leishmania* species were successfully used for the selection of potentially effective antiparasitic drugs, and for a several week observation of infection progression in mice [56].

Spectrally different NIR FPs allow for simultaneous observations of several tissues and organs in model organisms. The use of a pair of biomarkers of the iRFP family (iRFP670 and iRFP720) in a living mouse allowed for the simultaneous visualization of two closely located tumors labeled with different biomarkers [43]. An example of such imaging technique is shown in fig. 3. Owing to mathematical algorithms for image processing incorporated into modern microscopes and bioimaging systems, up to 5 spectrally different NIR FPs can be used simultaneously [43].

Photoactivated NIR FPs (PAiRFPs) have an advantage of ensuring highly sensitive bioimaging against strong autofluorescence background in tissues. To obtain images with high contrast ratio, a differential method is applied: a background signal is subtracted by comparing object’s images before and after PAiRFP photoactivation in tissue cells. Since PAiRFPs can be photoactivated, they are also used for selective photolabeling and short-term observations of the dynamics of groups of cells *in vivo* [46].

To study protein-protein interaction in cell cultures and living organisms, a novel iSplit NIR-sensor was developed whose

fluorescence is induced by interaction of complementary components, which drives the assembly of functional NIR FPs. Despite the irreversibility of complementation, iSplit can reflect the dynamics of rare recurring protein interactions due to a relatively rapid degradation of assembled complexes [47]. The advantage of another NIR split-sensor of protein interaction, IFP PCA, is reversibility of complementation. Its use allowed for the exploration of the interaction of several pairs of proteins in yeast and animal cells [57]. However, IFP PCA brightness in animal cells is an order of magnitude lower than that of iSplit, which requires the addition or injection of an extra amount of BV.

CONCLUSION

The variety of medical imaging techniques is impressive. Moreover, one and the same technique can enjoy multiple applications. However, all of them are designed to image the functional state of tissues and organs in the first place, facilitating the choice of the best treatment or allowing for the assessment of its efficacy.

In ultrasound imaging, high image quality is crucial and is an evolution vector for modern ultrasound scanners. Volumetric images (3D and 4D) have not yet enjoyed their widest application in the clinical setting. Their efficacy has not been proved yet, there are certain limitations to their use in some branches of medical science; clinicians often fail to interpret their results, and many clinics just do not have the appropriate state-of-art equipment. However, some clinicians believe that future belongs to volumetric images [58]. Another trend in US technologies is an increasing use of portable point-of-care US-scanners [58].

CT is evolving in the direction of more effective techniques for image reconstruction. New radiopharmaceuticals for PET and MRI enhancement are regularly tested. We might expect a boom of PET-MRI studies in the nearest future: combined modalities were introduced just a few years ago following the development of novel probes in 2010. PET-MRI provides for a better examination accuracy and a lower radiation dose a patient is exposed to [59]. Integrated PET-MRI can yield interesting results in the assessment of brain functions when enhanced with a combination of different radiotracers and used with specialized MRI protocols [60].

Oximetry *in vivo* is used in various areas of medical research, but its potential is most likely to be fully realized in measuring oxygen levels in malignant tumors for elaborating the best radiation therapy plan. Its clinical efficacy is expected to be proved in the next few years.

Studies that employed bacterial phytochrome-based NIR FPs demonstrate a high potential of these optical biomarkers for noninvasive bioimaging *in vivo* and suggest they could be used in preclinical trials [57, 61, 62].

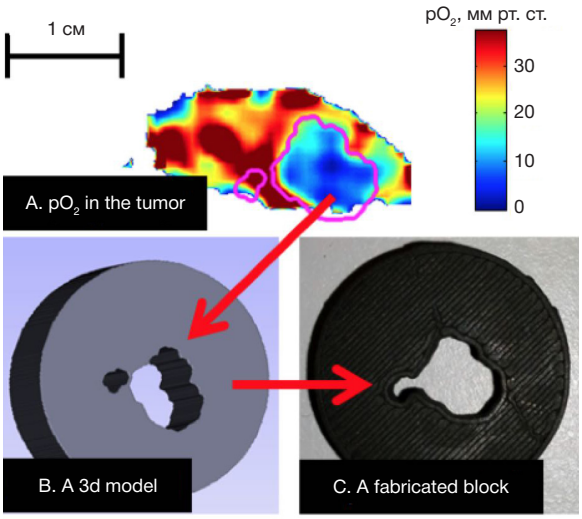

Fig. 2. Fabrication of blocks for targeted irradiation of a malignant tumor based on oxygen distribution in the tissue. **(A)** Slice of 3D image of pO_2 levels in different regions of mouse fibrosarcoma; a projection of tumor area selected for irradiation is outlined in magenta. **(B)** Computer model of the irradiation block. **(C)** Irradiation block printed on 3D printer (Epel et al. [42])

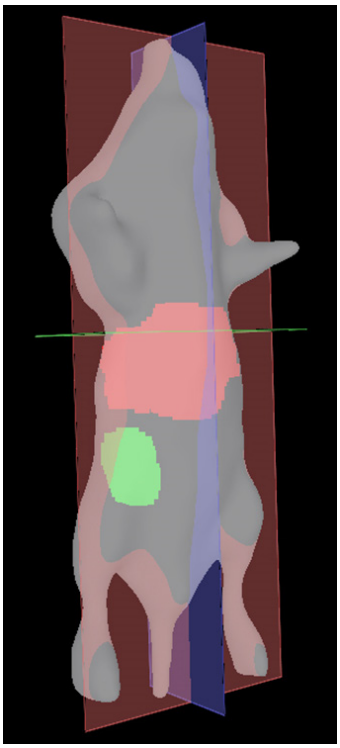

Fig. 3. Diffusion fluorescence image of a live mouse with a transplanted tumor and adenoviral infection in the liver. Tumor cells express iRFP670 protein, liver cells express iRFP713 protein. The liver and the tumor are shown in green and red pseudocolors, respectively (Scherbakova, Verkhusha, [43])

References

1. Osipov LV. Ul'trazvukovye diagnosticheskie pribory: rezhimy, metody i tekhnologii. Moscow: Izomed; 2011. 316 p. Russian.
2. Osipov LV. Tekhnologii elastografii v ul'trazvukovoy diagnostike. Obzor. Meditsinskiy alfavit: Diagnosticheskaya radiologiya i onkoterapiya. 2013; 3–4: 5–22. Russian.
3. Medimaging International staff writers. Poll's Findings Reveal Adaptable Imaging Systems to Transform Ultrasound Imaging. MedImaging.net. 2013 Sep 30.
4. Tai A. XDclear Transducer Technology [Internet]. GE Healthcare; c2016– [cited: 2016 Aug]. Available from: http://www3.gehealthcare.com/en.
5. Seeram E. Computed tomography: physical principles, clinical applications, and quality control. 4th ed. Saunders; 2015. 576 p.
6. Sun Z. Coronary Virtual Intravascular Endoscopy. In: Tintoiu IC, Underwood MJ, Cook SP, Kitabata H, Abbas A, editors. Coronary Graft Failure. Springer International Publishing; 2016. p. 555–70.
7. Schuhbaeck A, Achenbach S, Layritz C, Eisentopf J, Hecker F, Pflederer T, et al. Image quality of ultra-low radiation exposure

coronary CT angiography with an effective dose <0.1 mSv using high-pitch spiral acquisition and raw data-based iterative reconstruction. Eur Radiol. 2013; 23 (3): 597–606.
8. Bammer R. MR and CT Perfusion and Pharmacokinetic Imaging: Clinical Applications and Theory. Lippincott Williams and Wilkins; 2016. 1296 p.
9. Carrascosa PM, Garcia MJ, Cury RC, Leipsic JA. Dual-Energy CT. In: Carrascosa PM, Cury RC, Garcia MJ, Leipsic JA, editors. Dual-Energy CT in Cardiovascular Imaging. Springer International Publishing; 2015. p. 3–9.
10. Patino M, Prochowski A, Agrawal MD, Simeone FJ, Gupta R, Hahn PF, et al. Material Separation Using Dual-Energy CT: Current and Emerging Applications. Radiographics. 2016; 36 (4): 1087–105.
11. Fritz J, Henes JC, Fuld MK, Fishman EK, Horger MS. Dual-Energy Computed Tomography of the Knee, Ankle, and Foot: Noninvasive Diagnosis of Gout and Quantification of Monosodium Urate in Tendons and Ligaments. Semin Musculoskelet Radiol. 2016; 20 (1): 130–6.
12. Hashemi RH, Bradley WG, Lisanti CJ. MRI: The Basics. 3d ed. Lippincott Williams and Wilkins; 2012. 400 p.
13. Westbrook C, Roth CK, Talbot J. MRI in Practice. 4th ed. John Wiley and Sons; 2011. 456 p.
14. Taouli B, Beer AJ, Chenevert T, Collins D, Lehman C, Matos C, et al. Diffusion-weighted imaging outside the brain: Consensus statement from an ISMRM-sponsored workshop. J Magn Reson Imaging. 2016; 44 (3): 521–40.
15. Leote J, Nunes R, Cerqueira L, Ferreira HA. Corticospinal MRI tractography in space-occupying brain lesions by diffusion tensor and kurtosis imaging methods. EJNMMI phys. 2015; 2 (Suppl 1): A82.
16. Pinker K, Stadlbauer A, Bogner W, Gruber S, Helbich TH. Molecular imaging of cancer: MR spectroscopy and beyond. Eur J Radiol. 2012; 81 (3): 566–77.
17. Rosen Y, Lenkinski RE. Recent advances in magnetic resonance neurospectroscopy. Neurotherapeutics. 2007; 4 (3): 330–45.
18. Mabray MC, Barajas RF Jr, Cha S. Modern Brain Tumor Imaging. Brain Tumor Res Treat. 2015; 3 (1): 8–23.
19. Schulz J, Boyacioğlu R, Norris DG. Multiband multislab 3D time-of-flight magnetic resonance angiography for reduced acquisition time and improved sensitivity. Magn Reson Med. 2016; 75 (4): 1662–8.
20. Griffith B, Jain R. Perfusion imaging in neuro-oncology: basic techniques and clinical applications. Radiol Clin North Am. 2015; 53 (3): 497–511.
21. Uludağ K, Uğurbil K, Berliner L, editors. FMRI: From Nuclear Spins to Brain Functions. Springer US; 2015. 929 p.
22. Weissleder R. Molecular imaging in cancer. Science. 2006; 312 (5777): 1168–71.
23. Part 4: FDA-Approved PET/CT Tracers. In: Savir-Baruch B, Barron BJ. RadTool Nuclear Medicine Flash Facts. Springer International Publishing; 2016. 181–92.
24. Buchbender C, Heusner TA, Lauenstein TC, Bokisch A, Antoch G. Oncologic PET/MRI, part 2: bone tumors, soft-tissue tumors, melanoma, and lymphoma. J Nucl Med. 2012; 53 (8): 1244–52.
25. Tripathi RP. Recent trends in Molecular Imaging: PET/CT in Neurology. Ann Natl Acad Med Sci (India). 2014; 50 (1–2): 34–44.
26. Dolgushin MB, Odzharova AA, Tulin PE, Vikhrova NB, Nevzorov DI, Menkov MA, et al. [Use of ^{18}F-choline PET in Cerebral Gliomas]. Medical Visualization. 2014; 3: 73–83. Russian.
27. Lebron L, Greenspan D, Pandit-Taskar N. PET imaging of breast cancer: role in patient management. PET clin. 2015; Apr; 10 (2): 159–95.
28. Kurihara H, Shimizu C, Miyakita Y, Yoshida M, Hamada A, Kanayama Y, et al. Molecular imaging using PET for breast cancer. Breast Cancer. 2016; 23 (1): 24–32.
29. Mikhaylov AI, Tulin PE. Dvukhetapnaya PET/KT s 18F-ftorkholinom pri biokhimicheskikh retsidivakh raka predstatel'noy zhelezy. Evraziyskiy onkologicheskiy zhurnal. 2016; 2 (4): 388. Russian.
30. Dolgushin MB, Odzharova AA, Mikhailov AI, Shiryaev SV, Tulin PE, Nevzorov DI, et al. [Dual-stage ^{18}F-fluorocholine PET/CT scanning for biochemical recurrences of prostate cancer]. Cancer Urology.. 2015; 11 (2): 46–54. Russian.
31. Prosper A, Jadvar H. A Guided Tour of PET in Prostate Cancer. J Nucl Med. 2016; 57 (Suppl 2): 1319.
32. Barwick T. PET/CT imaging in prostate cancer. Cancer Imaging. 2015; 15 (Suppl 1): O15.
33. Ambrosini V, et al. PET/CT in Neuroendocrine Tumours. In: Ambrosini V, Fanti S, editors. PET/CT in Neuroendocrine Tumors. Springer International Publishing; 2016. p. 45–53.
34. Dolgushin MB, Shiryaev SV, Odzharova AA, Mikhaylov AI, Tulin PE, Nevzorov DI. PET-diagnostika v onkologii. Vestnik Moskovskogo onkologicheskogo obshchestva. 2015; 12 (603 Suppl): 63–74. Russian.
35. Jambor I, Kuisma A, Ramadan S, Huovinen R, Sandell M, Kajander S, et al. Prospective evaluation of planar bone scintigraphy, SPECT, SPECT/CT, 18F-NaF PET/CT and whole body 1.5 T MRI, including DWI, for the detection of bone metastases in high risk breast and prostate cancer patients: SKELETA clinical trial. Acta Oncol. 2016; 55 (1): 59–67.
36. Epel B, Halpern H. Electron paramagnetic resonance oxygen imaging in vivo. In: Gilbert BC, Murphy DM, Chechik V, editors. Electron Paramagnetic Resonance. Vol. 23. RSC Publishing; 2013. p. 180–208.
37. Matsumoto K, English S, Yoo J, Yamada K, Devasaharyam N, Cook JA, et al. Pharmacokinetics of a triarylmethyl-type paramagnetic spin probe used in EPR oximetry. Magnet Reson Med. 2004; 52 (4): 885–92.
38. Elas M, Bell R, Hleihel D, Barth ED, McFaul C, Haney CR, et al. Electron paramagnetic resonance oxygen image hypoxic fraction plus radiation dose strongly correlates with tumor cure in FSA fibrosarcomas. Int J Radiat Oncol Biol Phys. 2008; 71 (2): 542–9.
39. Elas M, Magwood JM, Butler B, Li C, Wardak R, Barth ED, et al. EPR Oxygen Images Predict Tumor Control by a 50 % Tumor Control Radiation Dose. Cancer Res. 2013; 73 (17): 5328–35.
40. Tatum JL, Kelloff GJ, Gillies RJ, Arbeit JM, Brown JM, Chao KS, et al. Hypoxia: Importance in tumor biology, noninvasive measurement by imaging, and value of its measurement in the management of cancer therapy. Int J Radiat Biol. 2006; 82 (10): 699–757.
41. Ardenkjaer-Larsen JH, Laursen I, Leunbach I, Ehnholm G, Wistrand LG, Petersson JS, et al. EPR and DNP properties of certain novel single electron contrast agents intended for oximetric imaging. J Magn Reson 1998; 133 (1): 1–12.
42. Epel B, Maggio C, Pelizzari C, Halpern HJ. Tumor oxygen-guided radiation therapy optimization. In: Oxygen Transport to Tissue XXXIX. Advances in Experimental Medicine and Biology. Springer. [In prep.].
43. Shcherbakova DM, Verkhusha VV. Near-infrared fluorescent proteins for multicolor in vivo imaging. Nat Methods. 2013; 10 (8): 751–4.
44. Shcherbakova DM, Baloban M, Pletnev S, Malashkevich VN, Xiao H, Dauter Z, et al. Molecular Basis of Spectral Diversity in Near-Infrared Phytochrome-Based Fluorescent Proteins. Chem Biol. 2015; 22 (11): 1540–51.
45. Rumyantsev KA, Shcherbakova DM, Zakharova NI, Emelyanov AV, Turoverov KK, Verkhusha VV. Minimal domain of bacterial phytochrome required for chromophore binding and fluorescence. Sci Rep. 2015; 5: 18348.
46. Piatkevich KD, Subach FV, Verkhusha VV. Far-red light photoactivatable near-infrared fluorescent proteins engineered from a bacterial phytochrome. Nat Commun. 2013; 4: 2153.
47. Filonov GS, Verkhusha VV. A near-infrared BiFC reporter for in vivo imaging of protein-protein interactions. Chem Biol. 2013; 20 (8): 1078–86.
48. Tchekanda E, Sivanesan D, Michnick SW. An infrared reporter to detect spatiotemporal dynamics of protein-protein interactions. Nat Methods. 2014; 11 (6): 641–4.
49. Lu Y, Darne CD, Tan IC, Wu G, Wilganowski N, Robinson H, et al. In vivo imaging of orthotopic prostate cancer with far-red gene reporter fluorescence tomography and in vivo and ex vivo validation. J Biomed Opt. 2013, 18 (10): 101305.
50. Jiguet-Jiglaire C, Cayol M, Mathieu S, Jeanneau C, Bouvier-Labit C, Ouafik L, et al. Noninvasive near-infrared fluorescent protein-based imaging of tumor progression and metastases in

deep organs and intraosseous tissues. J Biomed Opt. 2014, 19 (1): 16019.
51. Agollah GD, Wu G, Sevick-Muraca EM, Kwon S. In vivo lymphatic imaging of a human inflammatory breast cancer model. J Cancer. 2014; 5 (9): 774–83.
52. Condeelis J, Weissleder R. In vivo imaging in cancer. Cold Spring Harb Perspect Biol. 2010 Dec; 2 (12): a003848.
53. Wang Y, Zhou M, Wang X, Qin G, Weintraub NL, Tang Y. Assessing in vitro stem-cell function and tracking engraftment of stem cells in ischaemic hearts by using novel iRFP gene labelling. J Cell Mol Med. 2014; 18 (9): 1889–94.
54. Tran MT, Tanaka J, Hamada M, Sugiyama Y, Sakaguchi S, Nakamura M, et al. In vivo image analysis using iRFP transgenic mice. Exp Anim. 2014; 63 (3): 311–9.
55. Fyk-Kolodziej B, Hellmer CB, Ichinose T. Marking cells with infrared fluorescent proteins to preserve photoresponsiveness in the retina. Biotechniques. 2014;, 57 (5): 245–53.
56. Calvo-Alvarez, E.; Stamatakis, K.; Punzon, C.; Alvarez-Velilla, R.; Tejeria, A.; Escudero-Martinez, J. M.; Perez-Pertejo, Y.; Fresno, M.; Balana-Fouce, R.; Reguera, R. M. Infrared fluorescent imaging as a potent tool for in vitro, ex vivo and in vivo models of visceral leishmaniasis. PLoS Negl Trop Dis. 2015; 9 (3): e0003666.
57. Yao J, Kaberniuk AA, Li L, Shcherbakova DM, Zhang R, Wang L, et al. Multiscale photoacoustic tomography using reversibly switchable bacterial phytochrome as a near-infrared photochromic probe. Nat Methods. 2016, 13 (1): 67–73.
58. Zagoudis J, Fornell D. The Latest in Ultrasound Technology. Diagnostic and Interventional Cardiology [Internet]. 2016 Feb 12. Available from: http://www.dicardiology.com/article/latest-ultrasound-technology.
59. Kwon HW, Becker AK, Goo JM, Cheon GJ. FDG Whole-Body PET/MRI in Oncology: A Systematic Review. Nucl Med Mol Imaging. Epub 2016 Apr 7.
60. Vandenberghe S, Marsden PK. PET-MRI: a review of challenges and solutions in the development of integrated multimodality imaging. Phys Med Biol. 2015; 60 (4): R115–54.
61. Deliolanis NC, Ale A, Morscher S, Burton NC, Schaefer K, Radrich K, et al. Deep-tissue reporter-gene imaging with fluorescence and optoacoustic tomography: a performance overview. Mol Imaging Biol. 2014; 16 (5): 652–60.
62. Krumholz A, Shcherbakova DM, Xia J, Wang LV, Verkhusha VV. Multicontrast photoacoustic in vivo imaging using near-infrared fluorescent proteins. Sci Rep. 2014; 4: 3939.

Литература

1. Осипов Л. В. Ультразвуковые диагностические приборы: режимы, методы и технологии. М.: Изомед; 2011. 316 с.
2. Осипов Л. В. Технологии эластографии в ультразвуковой диагностике. Обзор. Медицинский алфавит: Диагностическая радиология и онкотерапия. 2013; 3–4: 5–22.
3. Medimaging International staff writers. Poll's Findings Reveal Adaptable Imaging Systems to Transform Ultrasound Imaging. MedImaging.net. 2013 Sep 30.
4. Tai A. XDclear Transducer Technology [Интернет]. GE Healthcare; c2016– [дата обращения: август 2016 г.]. Доступно по ссылке: http://www3.gehealthcare.com/en.
5. Seeram E. Computed tomography: physical principles, clinical applications, and quality control. 4th ed. Saunders; 2015. 576 p.
6. Sun Z. Coronary Virtual Intravascular Endoscopy. In: Tintoiu IC, Underwood MJ, Cook SP, Kitabata H, Abbas A, editors. Coronary Graft Failure. Springer International Publishing; 2016. p. 555–70.
7. Schuhbaeck A, Achenbach S, Layritz C, Eisentopf J, Hecker F, Pflederer T, et al. Image quality of ultra-low radiation exposure coronary CT angiography with an effective dose <0.1 mSv using high-pitch spiral acquisition and raw data-based iterative reconstruction. Eur Radiol. 2013; 23 (3): 597–606.
8. Bammer R. MR and CT Perfusion and Pharmacokinetic Imaging: Clinical Applications and Theory. Lippincott Williams and Wilkins; 2016. 1296 p.
9. Carrascosa PM, Garcia MJ, Cury RC, Leipsic JA. Dual-Energy CT. In: Carrascosa PM, Cury RC, Garcia MJ, Leipsic JA, editors. Dual-Energy CT in Cardiovascular Imaging. Springer International Publishing; 2015. p. 3–9.
10. Patino M, Prochowski A, Agrawal MD, Simeone FJ, Gupta R, Hahn PF, et al. Material Separation Using Dual-Energy CT: Current and Emerging Applications. Radiographics. 2016; 36 (4): 1087–105.
11. Fritz J, Henes JC, Fuld MK, Fishman EK, Horger MS. Dual-Energy Computed Tomography of the Knee, Ankle, and Foot: Noninvasive Diagnosis of Gout and Quantification of Monosodium Urate in Tendons and Ligaments. Semin Musculoskelet Radiol. 2016; 20 (1): 130–6.
12. Hashemi RH, Bradley WG, Lisanti CJ. MRI: The Basics. 3d ed. Lippincott Williams and Wilkins; 2012. 400 p.
13. Westbrook C, Roth CK, Talbot J. MRI in Practice. 4th ed. John Wiley and Sons; 2011. 456 p.
14. Taouli B, Beer AJ, Chenevert T, Collins D, Lehman C, Matos C, et al. Diffusion-weighted imaging outside the brain: Consensus statement from an ISMRM-sponsored workshop. J Magn Reson Imaging. 2016; 44 (3): 521–40.
15. Leote J, Nunes R, Cerqueira L, Ferreira HA. Corticospinal MRI tractography in space-occupying brain lesions by diffusion tensor and kurtosis imaging methods. EJNMMI phys. 2015; 2 (Suppl 1): A82.
16. Pinker K, Stadlbauer A, Bogner W, Gruber S, Helbich TH. Molecular imaging of cancer: MR spectroscopy and beyond. Eur J Radiol. 2012; 81 (3): 566–77.
17. Rosen Y, Lenkinski RE. Recent advances in magnetic resonance neurospectroscopy. Neurotherapeutics. 2007; 4 (3): 330–45.
18. Mabray MC, Barajas RF Jr, Cha S. Modern Brain Tumor Imaging. Brain Tumor Res Treat. 2015; 3 (1): 8–23.
19. Schulz J, Boyacioğlu R, Norris DG. Multiband multislab 3D time-of-flight magnetic resonance angiography for reduced acquisition time and improved sensitivity. Magn Reson Med. 2016; 75 (4): 1662–8.
20. Griffith B, Jain R. Perfusion imaging in neuro-oncology: basic techniques and clinical applications. Radiol Clin North Am. 2015; 53 (3): 497–511.
21. Uludağ K, Uğurbil K, Berliner L, editors. FMRI: From Nuclear Spins to Brain Functions. Springer US; 2015. 929 p.
22. Weissleder R. Molecular imaging in cancer. Science. 2006; 312 (5777): 1168–71.
23. Part 4: FDA-Approved PET/CT Tracers. In: Savir-Baruch B, Barron BJ. RadTool Nuclear Medicine Flash Facts. Springer International Publishing; 2016. 181–92.
24. Buchbender C, Heusner TA, Lauenstein TC, Bokisch A, Antoch G. Oncologic PET/MRI, part 2: bone tumors, soft-tissue tumors, melanoma, and lymphoma. J Nucl Med. 2012; 53 (8): 1244–52.
25. Tripathi RP. Recent trends in Molecular Imaging: PET/CT in Neurology. Ann Natl Acad Med Sci (India). 2014; 50 (1–2): 34–44.
26. Долгушин М. Б., Оджарова А. А., Тулин П. Е., Вихрова Н. Б., Невзоров Д. И., Меньков М. А. и др. ПЭТ с ^{18}F-фторхолином при исследовании глиальных опухолей головного мозга. Медицинская визуализация. 2014; 3: 73–83.
27. Lebron L, Greenspan D, Pandit-Taskar N. PET imaging of breast cancer: role in patient management. PET clin. 2015; Apr; 10 (2): 159–95.
28. Kurihara H, Shimizu C, Miyakita Y, Yoshida M, Hamada A, Kanayama Y, et al. Molecular imaging using PET for breast cancer. Breast Cancer. 2016; 23 (1): 24–32.
29. Михайлов А. И., Тулин П. Е. Двухэтапная ПЭТ/КТ с 18F-фторхолином при биохимических рецидивах рака предстательной железы. Евразийский онкологический журнал. 2016; 2 (4): 388.
30. Долгушин М. Б., Оджарова А. А., Михайлов А. И., Ширяев С. В., Тулин П. Е., Невзоров Д. И. и др. ПЭТ/КТ с ^{18}F-фторхо-

лином в режиме двухэтапного сканирования при биохимических рецидивах рака предстательной железы. Онкоурология. 2015; 11 (2): 46–54.
31. Prosper A, Jadvar H. A Guided Tour of PET in Prostate Cancer. J Nucl Med. 2016; 57 (Suppl 2): 1319.
32. Barwick T. PET/CT imaging in prostate cancer. Cancer Imaging. 2015; 15 (Suppl 1): O15.
33. Ambrosini V, et al. PET/CT in Neuroendocrine Tumours. In: Ambrosini V, Fanti S, editors. PET/CT in Neuroendocrine Tumors. Springer International Publishing; 2016. p. 45–53.
34. Долгушин М. Б., Ширяев С. В., Оджарова А. А., Тулин П. Е., Невзоров Д. И. ПЭТ-диагностика в онкологии. Вестник Московского онкологического общества. 2015; 12 (603 Приложение): 63–74.
35. Jambor I, Kuisma A, Ramadan S, Huovinen R, Sandell M, Kajander S, et al. Prospective evaluation of planar bone scintigraphy, SPECT, SPECT/CT, 18F-NaF PET/CT and whole body 1.5 T MRI, including DWI, for the detection of bone metastases in high risk breast and prostate cancer patients: SKELETA clinical trial. Acta Oncol. 2016; 55 (1): 59–67.
36. Epel B, Halpern H. Electron paramagnetic resonance oxygen imaging in vivo. In: Gilbert BC, Murphy DM, Chechik V, editors. Electron Paramagnetic Resonance. Vol. 23. RSC Publishing; 2013. p. 180–208.
37. Matsumoto K, English S, Yoo J, Yamada K, Devasaharyam N, Cook JA, et al. Pharmacokinetics of a triarylmethyl-type paramagnetic spin probe used in EPR oximetry. Magnet Reson Med. 2004; 52 (4): 885–92.
38. Elas M, Bell R, Hleihel D, Barth ED, McFaul C, Haney CR, et al. Electron paramagnetic resonance oxygen image hypoxic fraction plus radiation dose strongly correlates with tumor cure in FSA fibrosarcomas. Int J Radiat Oncol Biol Phys. 2008; 71 (2): 542–9.
39. Elas M, Magwood JM, Butler B, Li C, Wardak R, Barth ED, et al. EPR Oxygen Images Predict Tumor Control by a 50 % Tumor Control Radiation Dose. Cancer Res. 2013; 73 (17): 5328–35.
40. Tatum JL, Kelloff GJ, Gillies RJ, Arbeit JM, Brown JM, Chao KS, et al. Hypoxia: Importance in tumor biology, noninvasive measurement by imaging, and value of its measurement in the management of cancer therapy. Int J Radiat Biol. 2006; 82 (10): 699–757.
41. Ardenkjaer-Larsen JH, Laursen I, Leunbach I, Ehnholm G, Wistrand LG, Petersson JS, et al. EPR and DNP properties of certain novel single electron contrast agents intended for oximetric imaging. J Magn Reson 1998; 133 (1): 1–12.
42. Epel B, Maggio C, Pelizzari C, Halpern HJ. Tumor oxygen-guided radiation therapy optimization. In: Oxygen Transport to Tissue XXXIX. Advances in Experimental Medicine and Biology. Springer. [In prep.].
43. Shcherbakova DM, Verkhusha VV. Near-infrared fluorescent proteins for multicolor in vivo imaging. Nat Methods. 2013; 10 (8): 751–4.
44. Shcherbakova DM, Baloban M, Pletnev S, Malashkevich VN, Xiao H, Dauter Z, et al. Molecular Basis of Spectral Diversity in Near-Infrared Phytochrome-Based Fluorescent Proteins. Chem Biol. 2015; 22 (11): 1540–51.
45. Rumyantsev KA, Shcherbakova DM, Zakharova NI, Emelyanov AV, Turoverov KK, Verkhusha VV. Minimal domain of bacterial phytochrome required for chromophore binding and fluorescence. Sci Rep. 2015; 5: 18348.
46. Piatkevich KD, Subach FV, Verkhusha VV. Far-red light photoactivatable near-infrared fluorescent proteins engineered from a bacterial phytochrome. Nat Commun. 2013; 4: 2153.
47. Filonov GS, Verkhusha VV. A near-infrared BiFC reporter for in vivo imaging of protein-protein interactions. Chem Biol. 2013; 20 (8): 1078–86.
48. Tchekanda E, Sivanesan D, Michnick SW. An infrared reporter to detect spatiotemporal dynamics of protein-protein interactions. Nat Methods. 2014; 11 (6): 641–4.
49. Lu Y, Darne CD, Tan IC, Wu G, Wilganowski N, Robinson H, et al. In vivo imaging of orthotopic prostate cancer with far-red gene reporter fluorescence tomography and in vivo and ex vivo validation. J Biomed Opt. 2013, 18 (10): 101305.
50. Jiguet-Jiglaire C, Cayol M, Mathieu S, Jeanneau C, Bouvier-Labit C, Ouafik L, et al. Noninvasive near-infrared fluorescent protein-based imaging of tumor progression and metastases in deep organs and intraosseous tissues. J Biomed Opt. 2014, 19 (1): 16019.
51. Agollah GD, Wu G, Sevick-Muraca EM, Kwon S. In vivo lymphatic imaging of a human inflammatory breast cancer model. J Cancer. 2014; 5 (9): 774–83.
52. Condeelis J, Weissleder R. In vivo imaging in cancer. Cold Spring Harb Perspect Biol. 2010 Dec; 2 (12): a003848.
53. Wang Y, Zhou M, Wang X, Qin G, Weintraub NL, Tang Y. Assessing in vitro stem-cell function and tracking engraftment of stem cells in ischaemic hearts by using novel iRFP gene labelling. J Cell Mol Med. 2014; 18 (9): 1889–94.
54. Tran MT, Tanaka J, Hamada M, Sugiyama Y, Sakaguchi S, Nakamura M, et al. In vivo image analysis using iRFP transgenic mice. Exp Anim. 2014; 63 (3): 311–9.
55. Fyk-Kolodziej B, Hellmer CB, Ichinose T. Marking cells with infrared fluorescent proteins to preserve photoresponsiveness in the retina. Biotechniques. 2014;, 57 (5): 245–53.
56. Calvo-Alvarez, E.; Stamatakis, K.; Punzon, C.; Alvarez-Velilla, R.; Tejeria, A.; Escudero-Martinez, J. M.; Perez-Pertejo, Y.; Fresno, M.; Balana-Fouce, R.; Reguera, R. M. Infrared fluorescent imaging as a potent tool for in vitro, ex vivo and in vivo models of visceral leishmaniasis. PLoS Negl Trop Dis. 2015; 9 (3): e0003666.
57. Yao J, Kaberniuk AA, Li L, Shcherbakova DM, Zhang R, Wang L, et al. Multiscale photoacoustic tomography using reversibly switchable bacterial phytochrome as a near-infrared photochromic probe. Nat Methods. 2016, 13 (1): 67–73.
58. Zagoudis J, Fornell D. The Latest in Ultrasound Technology. Diagnostic and Interventional Cardiology [Интернет]. 12 февраля 2016 г. Доступно по ссылке: http://www.dicardiology.com/article/latest-ultrasound-technology.
59. Kwon HW, Becker AK, Goo JM, Cheon GJ. FDG Whole-Body PET/MRI in Oncology: A Systematic Review. Nucl Med Mol Imaging. Epub 2016 Apr 7.
60. Vandenberghe S, Marsden PK. PET-MRI: a review of challenges and solutions in the development of integrated multimodality imaging. Phys Med Biol. 2015; 60 (4): R115–54.
61. Deliolanis NC, Ale A, Morscher S, Burton NC, Schaefer K, Radrich K, et al. Deep-tissue reporter-gene imaging with fluorescence and optoacoustic tomography: a performance overview. Mol Imaging Biol. 2014; 16 (5): 652–60.
62. Krumholz A, Shcherbakova DM, Xia J, Wang LV, Verkhusha VV. Multicontrast photoacoustic in vivo imaging using near-infrared fluorescent proteins. Sci Rep. 2014; 4: 3939.

FLUORESCENCE IMAGING OF ACTIN CYTOSKELETON CHANGES IN CANCER CELLS UPON CHEMOTHERAPY

Klementieva NV[1]✉, Furman OE[1,2], Mishin AS[1,3], Lukyanov KA[1,3], Zagaynova EV[1]

[1] Research Institute of Biomedical Technologies,
Nizhny Novgorod State Medical Academy, Nizhny Novgorod, Russia

[2] Lobachevsky State University of Nizhny Novgorod – National Research University, Nizhny Novgorod, Russia

[3] Laboratory of Biophotonics, Department of Genetics and Postgenomic Technologies,
M. M. Shemyakin and Yu. A. Ovchinnikov Institute of Bioorganic Chemistry, Russian Academy of Sciences, Moscow, Russia

Structural organization of actin and actin-binding proteins can be a hallmark of aggressiveness among various populations of solid tumor cells. Here, we studied the impact of chemotherapeutic drugs (paclitaxel and cisplatin) on actin and alpha-actinin structural patterns in human cervical adenocarcinoma cell culture HeLa Kyoto using total internal reflection fluorescence microscopy and single-molecule localization super-resolution microscopy. It was shown that paclitaxel causes disruption of actin cytoskeleton in cancer cells, both for actin and alpha-actinin. We observed disappearance of stress fibers, accumulation of filaments in the cell cortex and morphological changes in focal contacts. With cisplatin, we detected a lower number of thin actin bundles and more dense arrangement of alpha-actinin. Our results suggest that the actin cytoskeleton is a potential target for antitumor chemotherapy.

Keywords: actin, alpha-actinin, microfilaments, cervical carcinoma cell culture, paclitaxel, cisplatin, fluorescence imaging

Funding: this work was supported by the Russian Science Foundation (project no. 14-25-00129).

Acknowledgement: authors thank the IBCH Core Facility for the equipment.

✉ **Correspondence should be addressed:** Natalia Klementieva
pl. Minina i Pozharskogo, d. 10/1, Nizhny Novgorod, Russia, 603005; nvklementieva@gmail.com

Received: 15.08.2016 **Accepted:** 25.08.2016

ФЛУОРЕСЦЕНТНАЯ ВИЗУАЛИЗАЦИЯ ИЗМЕНЕНИЙ АКТИНОВОГО ЦИТОСКЕЛЕТА В ОПУХОЛЕВЫХ КЛЕТКАХ ПОД ВОЗДЕЙСТВИЕМ ХИМИОТЕРАПЕВТИЧЕСКИХ АГЕНТОВ

Н. В. Клементьева[1]✉, О. Е. Фурман[1,2], А. С. Мишин[1,3], К. А. Лукьянов[1,3], Е. В. Загайнова[1]

[1] Научно-исследовательский институт биомедицинских технологий,
Нижегородская государственная медицинская академия, Нижний Новгород

[2] Нижегородский национальный исследовательский государственный университет имени Н. И. Лобачевского, Нижний Новгород

[3] Лаборатория биофотоники, отдел геномики и постгеномных технологий,
Институт биоорганической химии имени академиков М. М. Шемякина и Ю. А. Овчинникова РАН, Москва

Структурные особенности организации актина и актин-связывающих белков могут служить критериями оценки агрессивности различных популяций клеток злокачественных солидных опухолей. В настоящей работе мы изучили воздействие химиотерапевтических препаратов паклитаксел и цисплатин на структуру актина и альфа-актинина клеток рака шейки матки человека HeLa Kyoto с помощью флуоресцентной микроскопии полного внутреннего отражения и микроскопии сверхвысокого разрешения с детекцией одиночных молекул. Было показано, что паклитаксел вызывает существенные нарушения структуры актинового цитоскелета опухолевых клеток, затрагивающие как актин, так и альфа-актинин: исчезновение стресс-фибрилл, сосредоточение филаментов в кортикальном слое клеток, изменения морфологии фокальных контактов. Для цисплатина удалось детектировать сниженное содержание тонких волокон актина и более компактное расположение альфа-актинина. Полученные данные позволяют рассматривать актиновый цитоскелет как дополнительную мишень противоопухолевой химиотерапии.

Ключевые слова: актин, альфа-актинин, микрофиламенты, культура клеток рака шейки матки, паклитаксел, цисплатин, флуоресцентная визуализация

Финансирование: работа выполнена при поддержке Российского научного фонда (проект № 14-25-00129).

Благодарности: авторы благодарят Центр коллективного пользования ИБХ РАН за предоставленное оборудование.

✉ **Для корреспонденции:** Клементьева Наталия Владимировна
603005, г. Нижний Новгород, пл. Минина и Пожарского, д. 10/1; nvklementieva@gmail.com

Статья поступила: 15.08.2016 **Статья принята к печати:** 25.08.2016

Actin and actin-binding proteins are the cytoskeleton components forming microfilaments. They are involved in a variety of processes, such as cell growth, motility, division, transcription regulation, cell-matrix and cell-cell interactions. The actin cytoskeleton participates in signal transduction cascades and intracellular transport of proteins and organelles [1]. Energy-dependent polymerization and depolymerization of actin occur continuously inside the cell. The assembly of new actin filaments is accompanied by the formation of specialized structures, such as stress fibers, filopodia, lamellipodia. Actin cytoskeleton rearrangements can manifest cell dysfunction and its malignant transformation [2]. Cancer cells use various mechanisms including changes in adhesive and mechanical properties to support tumor survival and growth. The actin cytoskeleton structure can determine cancer cell stiffness, motility and invasion capacity [3].

Studying the structure of the actin cytoskeleton is essential for understanding the mechanism of antitumor drug action. For example, the effect of small interfering RNA inhibitors on cancer cell survival was demonstrated through visualization of actin cytoskeleton rearrangements [4]. The actin pattern also served as a criterion to assess the sensitivity of lung cancer cells to chemotherapy [5]. Moreover, actin itself can be used as a therapeutic target due to its potential to regulate tumor growth and metastasis formation [6, 7]. However, compounds that disrupt microfilament organization are highly toxic and have not been approved for clinical use yet.

Evaluation of actin cytoskeleton response to treatment with clinically approved anticancer drugs is a promising area of research. As a rule, malignant tumors are heterogeneous. Antitumor treatment outcome largely depends on the elimination of the most aggressive cell subpopulations. It has been shown that the most marked changes in the actin cytoskeleton occur in cells with metastatic capacity [8, 9]. Understanding the actin cytoskeleton dynamics in response to standard chemotherapy is important to detect potentially metastatic cells inside the tumor.

The aim of this work was to study structural changes in the actin cytoskeleton in cancer cells upon treatment with chemotherapy drugs paclitaxel and cisplatin widely used in clinical practice.

METHODS

We used HeLa Kyoto (human cervical cancer) cell line as a model system. The cells were cultured in Dulbecco's Modified Eagle's medium (PanEco, Russia) supplemented with 10 % fetal bovine serum (HyClone, GE Healthcare Life Sciences, USA), 2 mM glutamine (PanEco), 50 μg/ml streptomycin (PanEco), and 50 units/ml penicillin (PanEco) in an atmosphere of 5 % CO_2 at 37 °C.

For our experiment, we selected paclitaxel (Taxol) by Bristol-Mayers Squibb, USA, and cisplatin (Cisplatin-Teva) by Teva Pharmachemie, Netherlands. Cytochalasin D (Enzo Life Sciences, USA), an inhibitor of actin polymerization, was used as a control compound. To calculate LC50 of the chemotherapy drugs we applied the MTT assay [10], with drug-incubation period of 24 hours. Optical density of staining was measured on a Synergy Mx plate reader (BioTek, USA) at the wavelength of 570 and 630 nm.

200, 000 cells were seeded on 35 mm glass-bottom dishes (Fluorodish by WPI Inc., USA). The next day the culture medium was replaced with fresh medium containing chemotherapy drug (LC50), and cells were incubated for 24 hours under standard conditions. Cells without the adding drug were used as a control. Cells were then washed once with DPBS solution (PanEco), placed in 1 ml of FluoroBrite DMEM culture medium (Thermo Fisher Scientific, USA) and stained.

SiR-actin probe (Spirochrome, Switzerland) at 0.5 μM concentration and Hoechst 33342 (Molecular Probes, Thermo Fisher Scientific) at 5 μg/ml concentration were used to stain actin and nuclei, respectively. After 30-minute staining, fluorescence imaging was performed. SiR-actin [11] allowed for endogenous actin labeling in live cells without the need for fixation or wash procedure. The control and three experimental samples (with paclitaxel, cisplatin or cytochalasin D) were imaged; each sample was assessed in 10 fields of view.

For alpha-actinin labeling, we used pTagRFP-actinin expression vector (Evrogen, Russia). Cells were transiently transfected with pTagRFP-actinin using the X-tremeGene 9 reagent (Roche, USA) according to the manufacturer's protocol. The day after transfection, cells were incubated with the chemotherapy drugs (LC_{50}) for 24 hours. Cells were washed in DPBS solution and placed into 1 ml MEM culture medium (Sigma-Aldrich, USA). Then, fluorescence microscopy was performed. The control and three experimental samples (with paclitaxel, cisplatin and cytochalasin D) were studied. Each sample was assessed in 5–6 fields of view.

Fluorescence imaging was carried out on a Nikon Eclipse Ti inverted microscope (Nikon, Japan) equipped with 100X Apo TIRF/1.49 oil objective (Nikon) and EM-CCD-camera iXon3 DU-897 (Andor, UK). To collect a fluorescence signal from SiR-actin, we used a C-NSTORM QUAD filter (Nikon) and 640-nm laser (power density of 7.8 W/cm^2). To detect Hoechst 33342 fluorescence, a Nikon Intensilight fluorescence lamp and a BV-2A filter were used. Actin cytoskeleton was visualized by total internal reflection fluorescence microscopy (TIRF). TIRF-mode allows for the observation of thin layers (less than 200 nm) close to the cell membrane and ensures the highest signal-to-noise ratio; it is optimal for super-resolution single- molecule localization microscopy. Data processing was done with Fiji software [12]. TagRFP-based super-resolution microscopy was performed as described previously [13].

RESULTS

First, we determined the concentrations of chemotherapy drugs for treatment. Based on MTT assay results, viability/drug concentration curves for HeLa Kyoto cell culture were obtained. LC_{50} values for paclitaxel, cisplatin and cytochalasin D were 45 μM, 7 μM and 12.5 μM, respectively.

Then, we assessed the effect of chemotherapy drugs on the actin cytoskeleton of cancer cells using fluorescence microscopy. Fig. 1A shows typical HeLa Kyoto cells stained with SiR-actin (the control sample). Their actin cytoskeleton represents an extensive network of long stress fibers running across the cytoplasm in various directions. There are protrusions at the leading edge of the cell, as actin is enriched in the cell cortex. The image also shows a web-like meshwork of thin microfilaments that fill the entire cytoplasm. Cells under cytochalasin D treatment do not contain typical stress fibers. Their formation is driven by assembly of microfilaments from actin monomers, but in the presence of cytochalasin D this process is impeded. Here, short filaments along with dotted actin structures evenly distributed over the cytoplasm are typical. Stress fibers are rare and can be found near the plasma membrane only. Cells are more rounded and do not have protrusions at the leading edge (fig. 2B). No significant

damage to the microfilament organization is observed in cells treated with cisplatin. Here, HeLa Kyoto cells have a typical irregular shape with numerous stress fibers commonly found in spread cells. However, unlike the control sample, cells do not contain a network of thin microfilaments; no actin enrichment is found in the cell cortex after cisplatin treatment (fig. 1C). The paclitaxel sample reveals a more dramatic reorganization of the actin cytoskeleton, as compared to the cisplatin sample. For example, cells have almost no cytoplasmic protrusion and tend to be more round. Actin is mainly accumulated in the cell cortex. Microfilament fibers are rare, and stress fibers are absent (fig. 1D). Notably, the majority of cells are multinucleated.

A more accurate analysis of actin cytoskeleton changes was performed using super-resolution single-molecule localization fluorescence microscopy. We visualized a fine structure of the actin-binding protein alpha-actinin. In the control sample, cells show a typical pattern of alpha-actinin distribution along the actin bundles. Alpha-actinin completely fills the cytoplasm forming slight thickening at focal adhesion sites (fig. 2A). Cytochalasin D triggers complete disorganization of alpha-actinin, which is in accordance with actin aggregation and the absence of long stress fibers observed by TIRF microscopy. Isolated alpha-actinin structures of 200–250 nm in diameter are evenly distributed throughout the cell (fig. 2B). Cells treated with paclitaxel become round and lack protrusions and stress fibers. Alpha-actinin is accumulated in the cell cortex. The subdiffraction-resolution image shows substantial thickening and convergence of alpha-actinin fibrils at focal adhesion sites (fig. 2C). The least conspicuous changes are induced by cisplatin. Here, cells have an irregular shape and a common dotted cytoskeleton (fig. 2D). The structural changes include a more dense packing of alpha-actinin.

DISCUSSION

In this work, we have studied the effect of chemotherapy drugs paclitaxel and cisplatin on the actin cytoskeleton structure.

Paclitaxel belongs to the taxane family. Its mechanism of action is associated with the disruption of tubulin system; stabilization of microtubule assembly inhibits cell proliferation. Murakami et al. [14] have shown that taxane-based therapy reduces alpha-actin content in the stromal cells of breast tumors. Our findings demonstrate that, besides microtubules, microfilament system of cervical cancer cells also responds to paclitaxel treatment. Significant reorganization of actin structures observed (the appearance of rare thin curved filaments in the absence of stress fibers) is in agreement with the results obtained with MCF7 breast cancer cells treated with taxanes [15].

Interestingly, the majority of cells became multinucleated after incubation with paclitaxel. Its binding to beta-tubulin increases the number of cells in the G2/M phase and induces apoptosis and polyploidy [16, 17]. Actin skeleton rearrangements detected in HeLa Kyoto cell line could be indirectly related to the multinucleated phenotype. It is known that in normal multinucleated cells, such as osteoclasts, actin undergoes significant changes and represents isolated podosome-forming structures [18]. Giant multinucleated cells have been observed in HeLa-derived cell culture where actin is mainly accumulated in microspikes at the ventral face of the cell and in dotted podosome-like structures [19].

No direct link between the therapeutic effect of cisplatin and its impact on the actin filament rearrangement has been established. The mechanism of cisplatin action is associated with the ability of platinum ions to form intrastrand cross-links with DNA purine bases. As a result, DNA repair is inhibited and DNA damage induces apoptosis in cancer cells [20]. Nevertheless, the issue of cancer cell resistance to cisplatin and the role of actin in this process have been studied. For example, cisplatin-resistance cancer cells demonstrate changes in the expression of some cytoskeletal proteins, including actin, manifesting as abnormal actin-filamin dynamics [21, 22]. Sharma et al. observed conspicuous difference in the organization and mechanical properties of actin filaments in cisplatin-resistant ovarian cancer cells (OVCAR5), compared to the sensitive cells [23]. In their work, super-resolution microscopy was used for actin visualization that allowed them to detect specific patterns at the subdiffraction level, such as individual bundles or extensions of the cell at focal adhesion

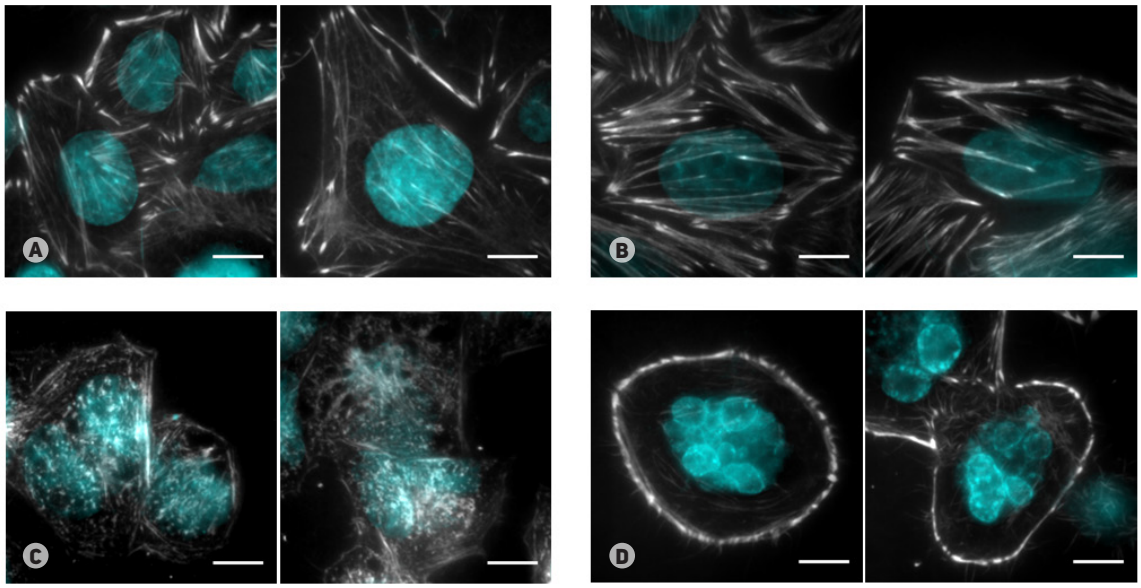

Fig. 1. Effects of chemotherapy drugs (LC_{50}) on the actin structure in HeLa Kyoto cervical cancer cells. **(A)** The control sample. **(B)** Cells incubated with cytochalasin D. **(C)** Cells incubated with cisplatin. **(D)** Cells incubated with paclitaxel

Fluorescence TIRF microscopy. Staining with SiR-actin (Spirochrome, Switzerland) and Hoechst 33342 (Thermo Fisher Scientific, USA). The actin cytoskeleton and the nuclei are shown in grey and blue, respectively. The scale bar is 10 μm.

sites. According to our findings, cisplatin has a weaker effect on the actin cytoskeleton of HeLa Kyoto cells, compared to paclitaxel. At the same time, super-resolution microscopy data indicate a high packing density of microfilaments that can potentially disrupt normal functioning of cancer cells.

CONCLUSIONS

We have studied the effect of two chemotherapy drugs (paclitaxel and cisplatin) on the actin cytoskeleton in HeLa Kyoto cervical cancer cells using fluorescence microscopy. We have found that paclitaxel leads to massive reorganization of the actin skeleton expressed as disassembly of stress fibers, actin accumulation in the cell cortex, thickening and convergence of focal adhesion sites. Cisplatin caused smaller changes, namely, reduction in the number of thin microfilament bundles and denser packing of alpha-actinin. We observed structural changes of actin cytoskeleton induced by chemotherapy drugs not specifically targeting it. In this light, actin might be considered as an additional target for anticancer therapy. Such reorganization of the microfilament system may affect metastatic and invasive capacities of cancer cells within solid tumor *in vivo*. We are planning to study the effect of chemotherapy on the actin cytoskeleton structure in a mouse tumor model.

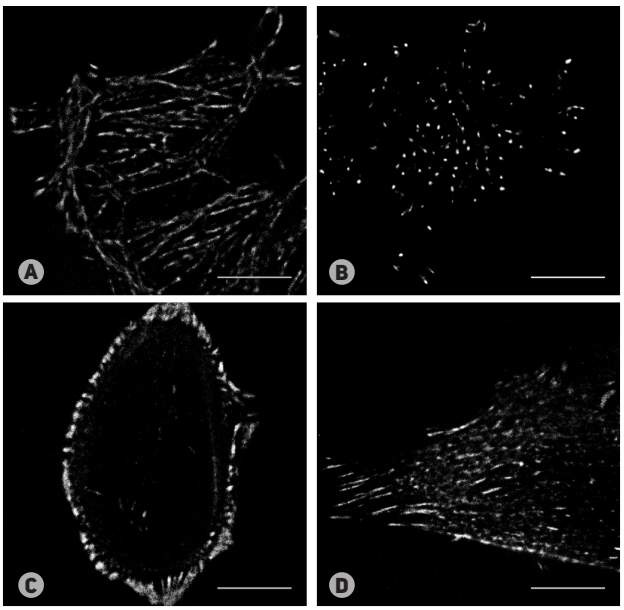

Fig. 2. Super-resolution single-molecule localization fluorescence microscopy of alpha-actinin labeled with fluorescent protein TagRFP in HeLa Kyoto cervical cancer cells. **(A)** The control sample. **(B)**. Cells incubated with cytochalasin D. **(C)** Cells incubated with paclitaxel. **(D)** Cells incubated with cisplatin The chemotherapy drugs were added at LC_{50}. The scale bar is 10 μm.

References

1. Bezanilla M, Gladfelter AS, Kovar DR, Wei-Lih L. Cytoskeletal dynamics: A view from the membrane. J Cell Biol. 2015; May 11; 209 (3): 329–37.
2. Shutova MS, Alexandrova AY. [Comparative research of normal and transformed fibroblast spreading. The role of microfilament polymerization and actin-myosin contractility]. Tsitologiya. 2010; 52 (1): 41–51. Russian.
3. Stevenson RP, Veltman D, Machesky LM. Actin-bundling proteins in cancer progression at a glance. J Cell Sci. 2012; 125 (Pt 5): 1073–9.
4. Groth-Pedersen L, Aits S, Corcelle-Termeau E, Petersen NHT, Nylandsted J, Jäättelä M. Identification of Cytoskeleton-Associated Proteins Essential for Lysosomal Stability and Survival of Human Cancer Cells. PLoS One. 2012; 7 (10): e45381.
5. Chen QY, Xu LQ, Jiao DM, Yao QH, Wang YY, Hu HZ, et. al. Silencing of Rac1 modifies lung cancer cell migration, invasion and actin cytoskeleton rearrangements and enhances chemosensitivity to antitumor drugs. Int J Mol Med. 2011 Nov; 28 (5): 769–76.
6. Bonello TT, Stehn JR, Gunning PW. New approaches to targeting the actin cytoskeleton for chemotherapy. Future Med Chem. 2009 Oct; 1 (7): 1311–31.
7. Brayford S, Schevzov G, Vos J, Gunning P. The Role of the Actin Cytoskeleton in Cancer and Its Potential Use as a Therapeutic Target. In: Schatten H, editor. The Cytoskeleton in Health and Disease. Luxemburg: Springer Science + Business Media; 2015. p. 373–91.
8. Gross SR. Actin binding proteins: their ups and downs in metastatic life. Cell Adh Migr. 2013 Mar–Apr; 7 (2): 199–213.
9. Nürnberg A, Kitzing T, Grosse R. Nucleating actin for invasion. Nat Rev Cancer. 2011; 11 (3): 177–87.
10. Mosmann T. Rapid colorimetric assay for cellular growth and survival: application to proliferation and cytotoxicity assays. J Immunol Methods. 1983 Dec 16; 65 (1–2): 55–63.
11. Lukinavičius G, Reymond L, D'Este E, Masharina A, Göttfert F, Ta H, et al. Fluorogenic probes for live-cell imaging of the cytoskeleton. Nat Methods. 2014 Jul; 11 (7): 731–3.
12. Schindelin J, Arganda-Carreras I, Frise E, Kaynig V, Longair M, Pietzsch T, et al. Fiji: an open-source platform for biological-image analysis. Nat Methods. 2012 Jun; 9 (7): 676–82.
13. Klementieva NV, Bozhanova NG, Mishina NM, Zagaynova EV, Lukyanov KA, Mishin AS. Common fluorescent proteins for single-molecule localization microscopy. Proc SPIE. 2015 Jul; 9536 (953609): [6 p.] Available from: http://dx.doi.org/10.1117/12.2184924.
14. Murakami M, Ernsting MJ, Undzys E, Holwell N, Foltz WD, Li SD. Docetaxel conjugate nanoparticles that target α-smooth muscle actin-expressing stromal cells suppress breast cancer metastasis. Cancer Res. 2013 Aug 1; 73 (15): 4862–71.
15. Rosenblum MD, Shivers RR. "Rings" of F-actin form around the nucleus in cultured human MCF7 adenocarcinoma cells upon exposure to both taxol and taxotere. Comp Biochem Physiol C Pharmacol Toxicol Endocrinol. 2000; 125 (1): 121–31.
16. Bottone MG, Soldani C, Tognon G, Gorrini C, Lazzè MC, Brison O, et al. Multiple effects of paclitaxel are modulated by a high c-myc amplification level. Exp Cell Res. 2003 Oct 15; 290 (1): 49–59.
17. Torres K, Horwitz SB. Mechanisms of Taxol-induced cell death are concentration dependent. Cancer Res. 1998 Aug 15; 58 (16): 3620–6.
18. Takito J, Otsuka H, Yanagisawa N, Arai H, Shiga M, Inoue M, et al. Regulation of Osteoclast Multinucleation by the Actin Cytoskeleton Signaling Network. J Cell Physiol. 2015 Feb; 230 (2): 395–405.
19. Dutartre H, Davoust J, Gorvel JP, Chavrier P. Cytokinesis arrest and redistribution of actin-cytoskeleton regulatory components in cells expressing the Rho GTPase CDC42Hs. J Cell Sci. 1996 Feb; 109 (Pt 2): 367–77.
20. Dasari S, Tchounwou PB. Cisplatin in cancer therapy: molecular mechanisms of action. Eur J Pharmacol. 2014; 740: 364–78.
21. Shen DW, Liang XJ, Gawinowicz MA, Gottesman MM. Identification of cytoskeletal [14C]carboplatin-binding proteins reveals reduced expression and disorganization of actin and filamin in cisplatin-resistant cell lines. Mol Pharmacol. 2004 Oct; 66 (4): 789–93.
22. Shen DW, Pouliot LM, Hall MD, Gottesman MM. Cisplatin resistance: a cellular self-defense mechanism resulting from multiple epigenetic and genetic changes. Pharmacol Rev. 2012

Jul; 64 (3): 706–21.
23. Sharma S, Santiskulvong C, Bentolila LA, Rao J, Dorigo O, Gimzewski JK. Correlative nanomechanical profiling with super-resolution F-actin imaging reveals novel insights into mechanisms of cisplatin resistance in ovarian cancer cells. Nanomedicine. 2012 Jul; 8 (5): 757–66.

Литература

1. Bezanilla M, Gladfelter AS, Kovar DR, Wei-Lih L. Cytoskeletal dynamics: A view from the membrane. J Cell Biol. 2015; May 11; 209 (3): 329–37.
2. Шутова М. С., Александрова А. Ю. Сравнительное исследование распластывания нормальных и трансформированных фибробластов. Роль полимеризации микрофиламентов и актин-миозинового сокращения. Цитология. 2010; 52 (1): 41–51.
3. Stevenson RP, Veltman D, Machesky LM. Actin-bundling proteins in cancer progression at a glance. J Cell Sci. 2012; 125 (Pt 5): 1073–9.
4. Groth-Pedersen L, Aits S, Corcelle-Termeau E, Petersen NHT, Nylandsted J, Jäättelä M. Identification of Cytoskeleton-Associated Proteins Essential for Lysosomal Stability and Survival of Human Cancer Cells. PLoS One. 2012; 7 (10): e45381.
5. Chen QY, Xu LQ, Jiao DM, Yao QH, Wang YY, Hu HZ, et. al. Silencing of Rac1 modifies lung cancer cell migration, invasion and actin cytoskeleton rearrangements and enhances chemosensitivity to antitumor drugs. Int J Mol Med. 2011 Nov; 28 (5): 769–76.
6. Bonello TT, Stehn JR, Gunning PW. New approaches to targeting the actin cytoskeleton for chemotherapy. Future Med Chem. 2009 Oct; 1 (7): 1311–31.
7. Brayford S, Schevzov G, Vos J, Gunning P. The Role of the Actin Cytoskeleton in Cancer and Its Potential Use as a Therapeutic Target. В книге: Schatten H, editor. The Cytoskeleton in Health and Disease. Luxemburg: Springer Science + Business Media; 2015. p. 373–91.
8. Gross SR. Actin binding proteins: their ups and downs in metastatic life. Cell Adh Migr. 2013 Mar–Apr; 7 (2): 199–213.
9. Nürnberg A, Kitzing T, Grosse R. Nucleating actin for invasion. Nat Rev Cancer. 2011; 11 (3): 177–87.
10. Mosmann T. Rapid colorimetric assay for cellular growth and survival: application to proliferation and cytotoxicity assays. J Immunol Methods. 1983 Dec 16; 65 (1–2): 55–63.
11. Lukinavičius G, Reymond L, D'Este E, Masharina A, Göttfert F, Ta H, et al. Fluorogenic probes for live-cell imaging of the cytoskeleton. Nat Methods. 2014 Jul; 11 (7): 731–3.
12. Schindelin J, Arganda-Carreras I, Frise E, Kaynig V, Longair M, Pietzsch T, et al. Fiji: an open-source platform for biological-image analysis. Nat Methods. 2012 Jun; 9 (7): 676–82.
13. Klementieva NV, Bozhanova NG, Mishina NM, Zagaynova EV, Lukyanov KA, Mishin AS. Common fluorescent proteins for single-molecule localization microscopy. Proc SPIE. 2015 Jul; 9536 (953609): [6 p.] Доступно по ссылке: http://dx.doi.org/10.1117/12.2184924.
14. Murakami M, Ernsting MJ, Undzys E, Holwell N, Foltz WD, Li SD. Docetaxel conjugate nanoparticles that target α-smooth muscle actin-expressing stromal cells suppress breast cancer metastasis. Cancer Res. 2013 Aug 1; 73 (15): 4862–71.
15. Rosenblum MD, Shivers RR. "Rings" of F-actin form around the nucleus in cultured human MCF7 adenocarcinoma cells upon exposure to both taxol and taxotere. Comp Biochem Physiol C Pharmacol Toxicol Endocrinol. 2000; 125 (1): 121–31.
16. Bottone MG, Soldani C, Tognon G, Gorrini C, Lazzè MC, Brison O, et al. Multiple effects of paclitaxel are modulated by a high c-myc amplification level. Exp Cell Res. 2003 Oct 15; 290 (1): 49–59.
17. Torres K, Horwitz SB. Mechanisms of Taxol-induced cell death are concentration dependent. Cancer Res. 1998 Aug 15; 58 (16): 3620–6.
18. Takito J, Otsuka H, Yanagisawa N, Arai H, Shiga M, Inoue M, et al. Regulation of Osteoclast Multinucleation by the Actin Cytoskeleton Signaling Network. J Cell Physiol. 2015 Feb; 230 (2): 395–405.
19. Dutartre H, Davoust J, Gorvel JP, Chavrier P. Cytokinesis arrest and redistribution of actin-cytoskeleton regulatory components in cells expressing the Rho GTPase CDC42Hs. J Cell Sci. 1996 Feb; 109 (Pt 2): 367–77.
20. Dasari S, Tchounwou PB. Cisplatin in cancer therapy: molecular mechanisms of action. Eur J Pharmacol. 2014; 740: 364–78.
21. Shen DW, Liang XJ, Gawinowicz MA, Gottesman MM. Identification of cytoskeletal [14C]carboplatin-binding proteins reveals reduced expression and disorganization of actin and filamin in cisplatin-resistant cell lines. Mol Pharmacol. 2004 Oct; 66 (4): 789–93.
22. Shen DW, Pouliot LM, Hall MD, Gottesman MM. Cisplatin resistance: a cellular self-defense mechanism resulting from multiple epigenetic and genetic changes. Pharmacol Rev. 2012 Jul; 64 (3): 706–21.
23. Sharma S, Santiskulvong C, Bentolila LA, Rao J, Dorigo O, Gimzewski JK. Correlative nanomechanical profiling with super-resolution F-actin imaging reveals novel insights into mechanisms of cisplatin resistance in ovarian cancer cells. Nanomedicine. 2012 Jul; 8 (5): 757–66.

MULTIMODAL OPTICAL COHERENCE TOMOGRAPHY IN THE ASSESSMENT OF CANCER TREATMENT EFFICACY

Sirotkina MA[1] ✉, Kiseleva EB[1], Gubarkova EV[1], Buyanova NL[1], Elagin VV[1], Zaitsev VYu[1,2], Matveev LA[1,2], Matveev AL[1,2], Kirillin MYu[2], Gelikonov GV[1,2], Gelikonov VM[1,2], Kuznetsov SS[1], Zagaynova EV[1], Gladkova ND[1]

[1] Nizhny Novgorod State Medical Academy, Nizhny Novgorod, Russia

[2] Institute of Applied Physics, Russian Academy of Sciences, Nizhny Novgorod, Russia

One of the challenges faced by modern medicine is finding new methods of functional imaging of biological tissues in patients that allow detection of early tumor response to treatment. One of such methods proposed in this work is multimodal optical coherence tomography (MM OCT). It combines cross-polarization OCT (CP OCT) for visualization of tissue structure and assessment of connective tissue health, OCT-based microangiography (OCT MA) for visualization of the vasculature, and OCT-based elastography for measuring tissue stiffness. The efficacy of this method was tested during the course of photodynamic therapy (PDT), as major PDT targets are cellular and vascular components of a tumor. The experiments were carried out on the CT26 colon carcinoma transplanted into the mouse ear. It was shown that the efficacy of PDT can be assessed using MM OCT. For example, CP OCT can help differentiate between necrotic and intact tumors; OCT MA detects blood circulation defects that lead to slower blood circulation or circulatory stagnation followed by tumor death. OCT-based elastography is helpful in assessing stiffness of normal and pathological tissues.

Keywords: multimodal optical coherence tomography, cross-scattering, microangiography, elastography, photodynamic therapy, CT26 colon carcinoma, experimental tumor

Funding: this work was supported by the Ministry of Education and Science of the Russian Federation (grant no. 14.B25.31.0015), numerical processing of CP OCT images was supported by grant no. 15-32-20250 of the Russian Foundation for Basic Research, algorithm modification and development of software/hardware OCT-system for mapping microcirculation and elastography images was supported by the grant of the President of the Russian Federation for young scientists (no. MK-6504.2016.2) and the grant of the Russian Foundation for Basic Research (no. 16-02-00642-a).

Acknowledgements: authors thank professor Alex Vitkin of University of Toronto (Toronto, Canada), the leading scientist of the Russian Federation Government Mega-grant 14.B25.31.0015.

✉ **Correspondence should be addressed:** Marina Sirotkina
pl. Minina i Pozharskogo, d. 10/1, Nizhny Novgorod, Russia, 603950; sirotkina_m@mail.ru

Recieved: 15.08.2016 **Accepted:** 25.08.2016

ПРИМЕНЕНИЕ МУЛЬТИМОДАЛЬНОЙ ОПТИЧЕСКОЙ КОГЕРЕНТНОЙ ТОМОГРАФИИ В ОЦЕНКЕ ЭФФЕКТИВНОСТИ ТЕРАПИИ РАКА

М. А. Сироткина[1] ✉, Е. Б. Киселева[1], Е. В. Губарькова[1], Н. Л. Буянова[1], В. В. Елагин[1], В. Ю. Зайцев[1,2], Л. А. Матвеев[1,2], А. Л. Матвеев[1,2], М. Ю. Кириллин[2], Г. В. Геликонов[1,2], В. М. Геликонов[1,2], С. С. Кузнецов[1], Е. В. Загайнова[1], Н. Д. Гладкова[1]

[1] Нижегородская государственная медицинская академия, Нижний Новгород

[2] Институт прикладной физики РАН, Нижний Новгород

Поиск новых способов прижизненной функциональной визуализации биологических тканей, которые позволяют выявлять ранний ответ опухоли на выбранную терапию с целью коррекции курса лечения, — актуальная задача современной медицины. В качестве такого способа в работе предложена мультимодальная оптическая когерентная томография (ММ ОКТ), которая сочетает в себе кросс-поляризационную ОКТ (КП ОКТ) для визуализации структуры ткани и оценки состояния соединительнотканного компонента, ОКТ-микроангиографию (ОКТ МА) для визуализации сосудистого русла и ОКТ-эластографию для изучения жесткости ткани. Эффективность метода проверяли на примере действия фотодинамической терапии (ФДТ), поскольку основными мишенями ФДТ являются клеточный и сосудистый компоненты опухоли. В качестве объекта исследования была выбрана карцинома кишечника мыши CT26, локализованная на ухе мыши. Показано, что с помощью ММ ОКТ можно оценить эффективность ФДТ, а именно: по КП ОКТ — отличить опухоль с некрозом от интактной опухоли, по ОКТ МА — выявить расстройства кровообращения, приводящие к замедлению или остановке кровотока и дальнейшей гибели опухоли, а по ОКТ-эластографии — определить жесткость нормальной и патологической ткани.

Ключевые слова: мультимодальная оптическая когерентная томография, кросс-рассеяние, микроангиография, эластография, фотодинамическая терапия, карцинома кишечника CT26, экспериментальная опухоль

Финансирование: работа выполнена при финансовой поддержке гранта Министерства образования и науки РФ (договор № 14.B25.31.0015); числовая обработка КП ОКТ-изображений поддержана грантом Российского фонда фундаментальных исследований (проект № 15-32-20250); модификация алгоритма и разработка программно-аппаратного ОКТ-комплекса для картирования микроциркуляторных и эластографических изображений поддержана грантом Президента РФ для молодых ученых № МК-6504.2016.2 и грантом Российского фонда фундаментальных исследований № 16-02-00642-а.

Благодарности: авторы благодарят профессора Алекса Виткина из Университета Торонто (Торонто, Канада) — ведущего ученого мегагранта, в рамках которого выполнена работа.

✉ **Для корреспонденции:** Сироткина Марина Александровна
603950, г. Нижний Новгород, пл. Минина и Пожарского, д. 10/1; sirotkina_m@mail.ru

Статья получена: 15.08.2016 **Статья принята в печать:** 25.08.2016

In spite of advances in the diagnosis and treatment of cancer, mortality in cancer patients is still high. Tumor heterogeneity remains a challenge that largely affects treatment progress [1]. Patients with tumors of the same type often respond differently to identical therapies. Thus, detecting early tumor response to treatment is crucial for introducing timely adjustments to a treatment plan. The literature reports studies aimed at finding criteria for the assessment of antitumor therapy efficacy [2], but no reliable models have been suggested so far.

Optical coherence tomography (OCT) is a noninvasive diagnostic tool for imaging in turbid media. OCT utilizes backscattering, permitting scan depth of 1–2 mm, and forms 2D and 3D images. This technique is based on the low coherence interferometry with a broad bandwidth light source in the near-infrared wavelength range (the so-called therapeutic transparency window of 0.7–1.3 μm) [3–5]. OCT is not damaging to the organism, since its power output is only 3–5 mW. Compared to nuclear magnetic resonance imaging and high frequency ultrasound scanning, it has a higher spatial resolution (up to 15 μm), is more cost-effective and easier to use. Clinically, it is used for early diagnosis of neoplasia, resection margin definition prior to excision and for monitoring patients with previous cancers in order to timely detect recurrences [6].

The application of this technique is not limited to standard tissue visualization. It can also be used for blood circulation and vasculature structure imaging. It is very important for biological and medical research, as it allows obtaining data on tissue functioning *in vivo*. Such data can influence the choice of cancer therapy, as some treatments induce vascular damage in tumors [7]. Therefore, a lot of research laboratories are now working on optimizing OCT techniques for intravital microvascular imaging. Among the most promising methods of detection, visualization and quantitative assessment/monitoring of tissue microcirculation are those based on speckle variance [8].

Mechanical properties of biological tissues are related to their structure and functions that change in the presence of pathology or during the course of treatment. The last 15 years have seen the increasing focus on OCT-based tissue stiffness measuring (tissue elasticity mapping). Optical coherence elastogrpahy has been demonstrated *in vivo* [9] and recommended for tumor detection in soft tissues [10]. Some researchers have described the potential of this method for differentiating between malignant and healthy breast tissues [14, 15]. At the moment, there are no OCT scanners for elastographic mapping on the market. In Russia, there are a number of research centers in Nizhniy Novgorod, Saratov and St. Petersburg that work on OCT optimization, but only a few researchers from the Institute of Applied Physics of RAS (Nizhny Novgorod) and Nizhny Novgorod State Medical Academy (NNSMA) work with optical coherence elastogrpahy [16].

A combination of the methods described above forms a multimodal OCT that can be an effective tool for monitoring tumor response to therapy and interpreting new findings, thus driving us toward personalized treatment. The aim of this work was to test the feasibility of three OCT modalities for the assessment of tumor response to therapy.

METHODS

Animal model

The study was carried out on the experimental model of murine CT26 colon carcinoma. The tumor cell suspension (200,000 cells in 20 μl phosphate buffer) was inoculated intracutaneously into the external auricle tissue of 8-month old female BALB/c mice (weight of 20–22 g). An ear tumor model is characterized by a surface growth, a relatively small size (several millimeters in diameter) and good accessibility for visual examination and optical bioimaging. The experiment was approved by the Ethics Committee of NNSMA (protocol no. 14 dated December 10, 2013).

Photodynamic therapy

We decided on the short-term (from several hours up to several days) photodynamic therapy (PDT) that affects both vascular and cellular tumor components. PTD was introduced 10–14 days after the inoculation when the tumor size was 3.5–4.0 mm and its vasculature was well formed. The animals received 5 mg/kg i. v. Fotoditazin by Veta-Grand, Russia. One hour after the photosensitizer injection, the tumor was exposed to the diode laser radiation with a wavelength of 659 nm; the dosage used was 75 J/cm2 (100 mW/cm^2). The experimental group consisted of 10 animals; the control group included 5 mice.

Multimodal optical coherence tomography

The tumor response to PDT was assessed by MM OCT using the system developed by the Institute of Applied Physics, RAS. System parameters were as follows: operating wavelength of 1.3 μm, power output of 15 mW, transverse spatial resolution of 25 μm, axial resolution of 15 μm, scanning depth of up to 1.7 μm. Probing radiation was circularly polarized, scanning speed was 20,000 A-scans per second.

We performed noncontact MM OCT scanning by positioning the optical probe at 1.5 cm distance from the studied surface.

2D images (B-scans) of 4 × 4 mm were obtained in the cross-polarization OCT (CP OCT) mode. The scans consisted of 2 pseudocolor images: the top co-polarized image showing the intensity of backscattered waves that preserved the initial level of polarization, and the bottom cross-polarized image showing the intensity of backscattered waves that changed their initial polarization to orthogonal. In most cases, cross-scattering is observed in highly organized anisotropic structures, such as collagen and elastic fibers [17]. The CP OCT mode allows recording 3D images in co- and cross-polarization modes, each of them of 4 × 4 × 2 mm in size (the figures correspond to planar dimensions and depth).

Quantitative processing of CP OCT images included computing of the integral depolarization factor (IDF) for the manually selected area of interest (selection was based on histological analysis results and qualitative attributes of CP OCT images). IDF calculation algorithm was previously developed by the authors of this work and described in [18]. We had used it for the assessment of the functional state of collagen fibers in various tissues (bladder and oral mucosa, aorta and coronary arteries). Its calculation is based on the averaged ratio of OCT signal intensities in cross- and co-polarization modes.

Tissue stiffness was assessed using optical coherence elastogrpahy. To extract information from the OCT signal, we used an improved (hybrid) phase-sensitive approach to strain estimation [16]. The probe was slightly pressed to the studied surface (a tissue compression method used for data acquisition), and the deformities in the probe vicinity were registered. Elastographic mapping is based on the analysis of spatial heterogeneity of changes in the OCT signal phase in the tissue induced by its motion. On the resulting pseudocolor images, stiffer areas (those with little deformation) are shown in blue, and soft areas, where deformation is considerable, are shown in red.

The microvasculature was studied using OCT-based microangiography (OCT MA). Vascular network visualization is based on the time-related alterations of OCT signal amplitude and phase shown on the series of pixelated OCT images of the same tissue region. The areas where the signal changes rapidly indicate the presence of flowing liquid (blood). The areas of pixels with stable values of amplitudes and phases mean there is no liquid there. Thus, OCT MA can be used for the visualization of both normal blood circulation and stasis, as in PDT-induced thrombosis. OCT MA scans were obtained from the area of 2 x 2 mm^3. The pattern was highly sensitive making it possible to visualize small blood vessels. Processed OCT MA images were a projection of the maximum signal intensity (a vascular network top view, full depth imaging) [19].

Fluorescence microscopy

The data on the vascular network structure obtained with OCT MA were verified by fluorescence microscopy on the Axio Zoom.V16 stereomicroscope (Zeiss, Germany) using FITC fluorophore conjugated to dextran (Sigma-Aldrich, USA). 50 mg/kg fluorophore were injected i. v. into the tail vein. Images were obtained within 10 minutes after fluorophore administration.

Histological analysis

Tumor cell death and blood circulation defects were verified by light microscopy 2 days after PDT. Samples were fixated in 10 % neutral buffered formalin. 7 μm thick histological sections were prepared using the Leica SM 2000 R sliding microtome (Leica Biosystems, Germany). To study tumor tissue morphology, the sections were deparaffinized and stained with hematoxylin and eosin.

RESULTS

MM OCT imaging of mouse ear tissue

CP OCT

Ear tissue is a layered structure consisting of the epidermis, the dermis with cutaneous appendages, and the cartilage (fig. 1A). In the co-polarization mode, CP OCT images of healthy ear tissue show a layered structure with the cartilage in the middle represented as a thin line of a low intensity signal; on the both sides of it are dermis layers of a high intensity signal. The epidermis is visualized above the dermis as a very thin line of a low intensity signal (fig. 1B). In the cross-polarization mode, the image is also layered, but the signal intensity of the co-polarized layers described above is an order of magnitude weaker, because this mode can only "see" a signal from optically anisotropic structures, such as collagen or elastic fibers of the dermis and the cartilage. As the tumor grows in the dermis, the total volume of the tissue above the cartilage gradually increases, and CP OCT scans show deformation of tissue layers. Images obtained by noncontact scanning show a small protuberance in the tumor site (fig. 1D). Dense tumor cells do not cross-polarize or cross-scatter the probing radiation. The signal intensity around the tumor is reduced due to the disrupted organization of dermal collagen (fig. 1D).

OCT MA

OCT MA was used to visualize the structure of the vascular network of healthy ear tissues (fig. 2B) and the area where the CT26 tumor had been transplanted (fig. 2G). Images of normal tissue show large blood vessels, i. e., arterioles and venules. In the presence of pathology, smaller blood vessels can be visualized forming a dense interwoven network. Such imaging specifics can be related to the formation of new blood vessels in the tumor or to the increased blood flow velocity in the already existing vessels. We are still working on the interpretation of this fact. The vascular network structures in healthy and pathological tissues visualized on OCT MA images are identical to those seen on fluorescence microscopy images (fig. 2C, 2E), which indicates that data obtained with OCT MA are accurate. Thus, OCT MA can be used to differentiate between normal and pathological tissues.

Optical coherence elastography

Examples of *in vivo* elastographic deformation mapping in lab animals using manual probing are presented in fig. 3. Fig. 3A and 3B show structured and elastographic images of healthy ear tissue. The structured image (fig. 3A) shows that tissue in the selected frame is morphologically heterogenic and the OCT signal is scattered evenly; as a result, the elastographic map reflects uniform strain distribution (fig. 3B). The same area looks 2.0–2.5 times thicker in the structured image of the ear tissue sample with the transplanted tumor (fig. 3C) and is characterized by reduced scattering of probing signal. The elastographic map (fig. 3G) shows that tumor site is presented as a clearly outlined deformation zone.

CT26 tumor growth in the mouse ear

CT26 tumor growth was studied using CP OCT and OCT MA. As the tumor grows, the CP OCT images demonstrate that signal intensity drops and reaches its minimum on day 14 after tumor inoculation. The signal penetration depth also decreases (fig. 4, top row). OCT MA images show that as the tumor grows in size, the number of blood vessels also increases (fig. 4, bottom row).

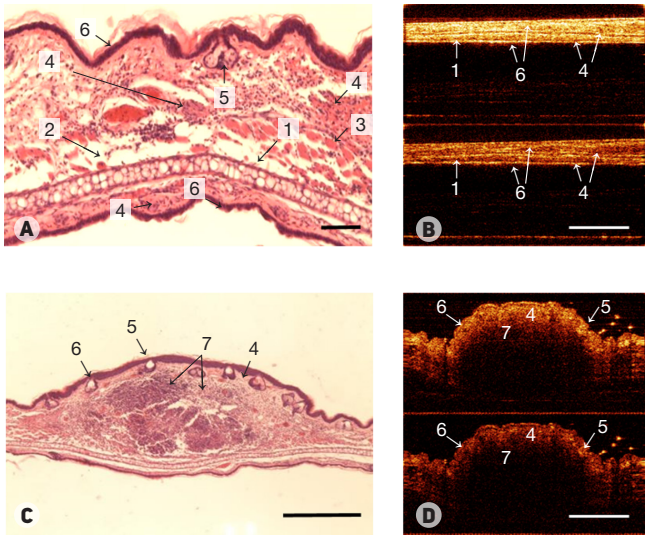

Fig. 1. Visualization of healthy tissue **(A, B)** and CT26 colon carcinoma transplanted into the mouse ear **(C, D)**

(A) and **(C)** are histological sections (the scale bars are 100 μm and 500 μm, respectively). **(B)** and **(D)** are images obtained with cross-polarized optical coherence tomography (the scale bar is 1 μm). 1 — the cartilage; 2 — the adipocyte layer; 3 — the cross-striated muscle; 4 — the dermis; 5 — hair follicles; 6 — the epidermis; 7 — the tumor tissue.

Tumor response to photodynamic treatment

Analysis of histological sections

PDT causes damage to malignant cells and disrupts blood flow to the tumor. On day 2 after the treatment necrotic lesions were detected covering about 60 % of the whole tumor. Along with tissue necrosis, we observed blood circulation defects: stasis, sludge syndrome, thrombosis and hemorrhage.

Analysis of CP OCT images

The damaging effect of PDT on tumor cells and vasculature is supposed to affect optical properties of the tumor. Fig. 5 shows depolarization factor maps for the experimental (PDT) and control groups. In the controls, the tumor was characterized by low values of depolarization factor (fig. 5A) suggesting low cross-scattering capacity of the tissue. In tumors treated with PDT, IDF maps show increased cross-scattering (fig. 5B): IDF values increase from 0.020 ± 0.007 to 0.036 ± 0.013. We conclude that prevalence of necrotic lesions in the tumor formed by the deposition of inflammatory cells, destroyed collagen fibers and true tumor cells leads to the increased number of cross-scatter sites and a higher IDF.

Analysis of OCT MA images

OCT MA-based monitoring of the tumor vascular network within a few hours after the treatment demonstrates the instant response of the vasculature to radiation: the majority of blood vessels are not visualized during the procedure (fig. 6B). 24 h after PDT, the vessels are not visualized on OCT MA (fig. 6C). The obtained results confirm that in the presence of blood circulation abnormalities that significantly reduce blood flow or cause stasis, OCT MA does not visualize blood vessels. Fluorescence microscopy images also do not show the vascular network (fig. 6E).

DISCUSSION

In this work, we present the results of the first multimodal OCT-based complex study of normal and pathological tissues. We obtained and analyzed OCT images of tissue structure and vascular network and maps of stiffness distribution

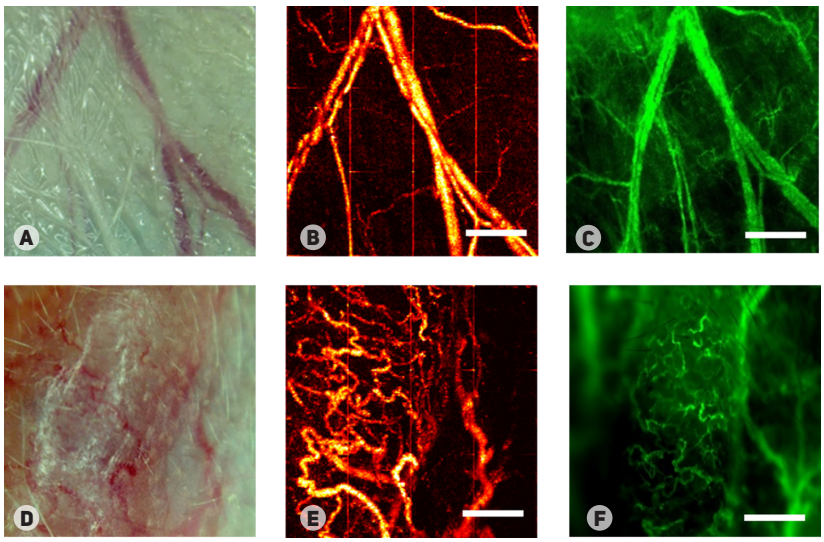

Fig. 2. Visualization of a vascular network of healthy tissue **(A–C)** and CT26 colon carcinoma transplanted into the mouse ear **(D–F)**
(A) and **(B)** are microphotographs, **(C)** and **(D)** are images obtained with OCT-based microangiography, **(E)** and **(F)** are fluorescence microscopy images. The scale bar is 0.5 mm.

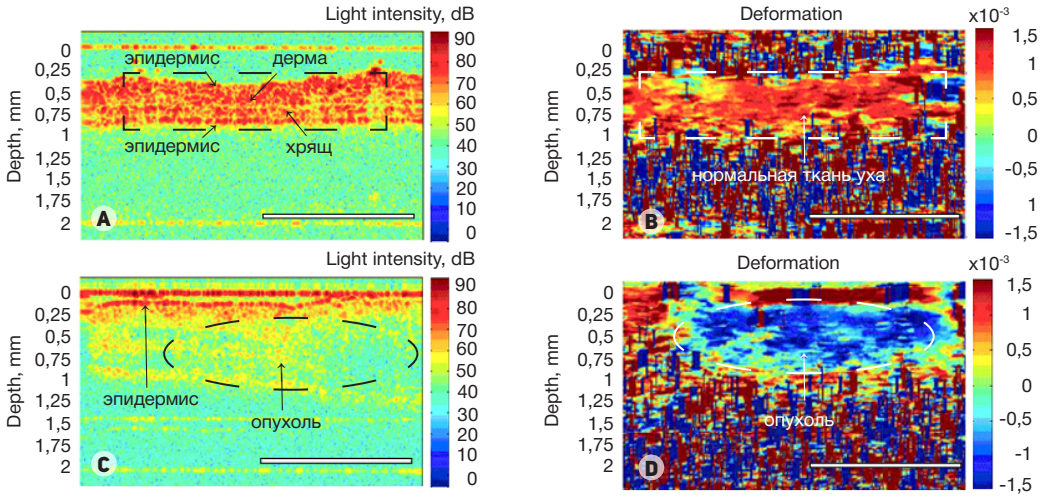

Fig. 3. Structured *in vivo* OCT images **(A, C)** and elastographic deformation maps **(B, D)** of healthy tissues of the mouse ear **(A, B)** and CT26 colon carcinoma transplanted into the mouse ear **(C, D)** (the scale bar is 1 mm)

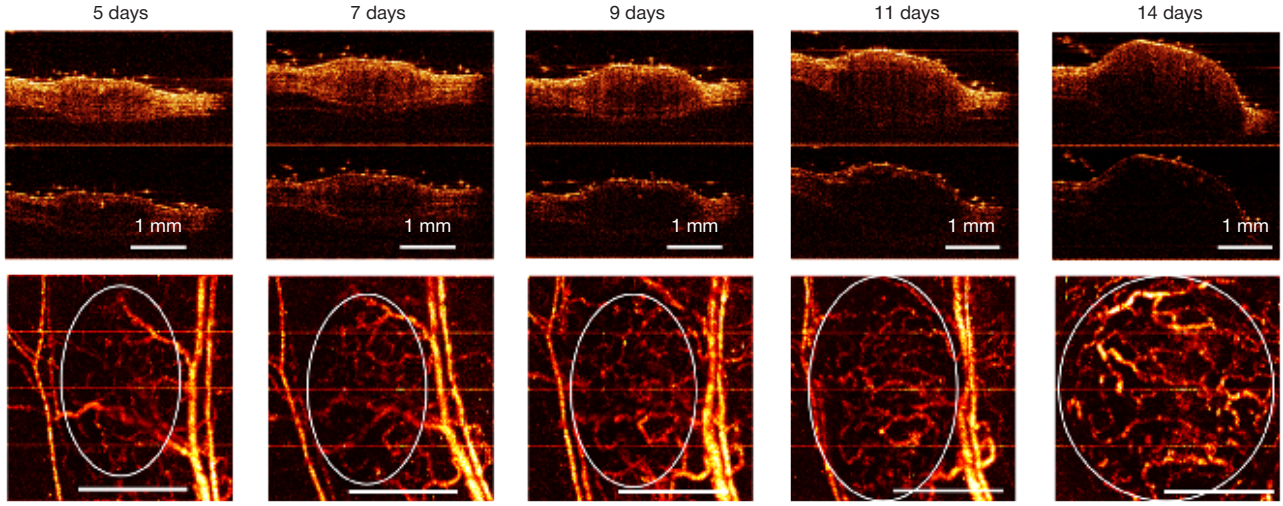

Fig. 4. MM OCT-based monitoring of CT26 colon carcinoma transplanted into the mouse ear
Top row: CP OCT images; bottom row: OCT MA images. The tumor site is circled.

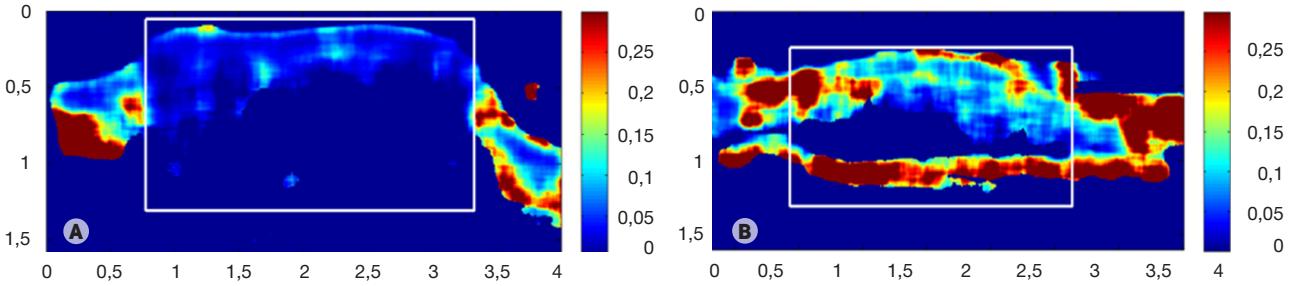

Fig. 5. Depolarization maps based on B-scans. **(A)** — tumor before photodynamic therapy, **(B)** — tumor after photodynamic therapy

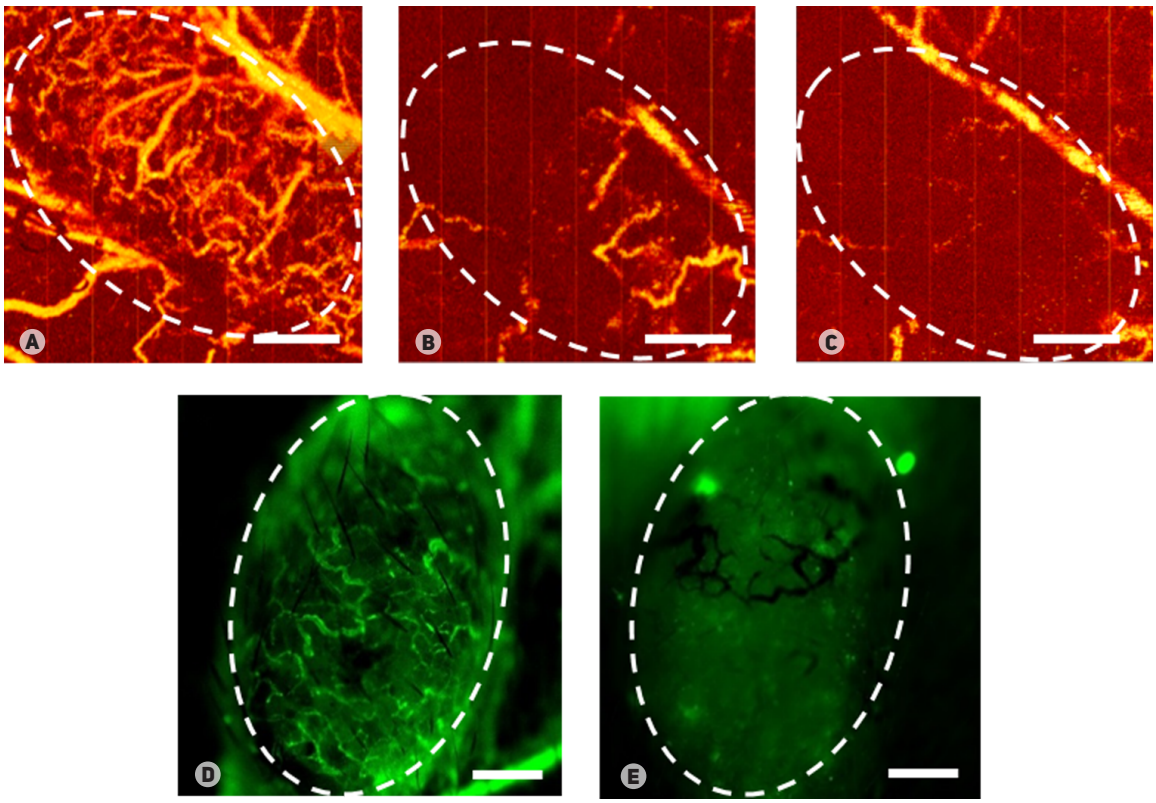

Fig. 6. Visualization of the vascular response of CT26 colon carcinoma transplanted into the mouse ear to photodynamic therapy on OCT MA **(A–C)** and fluorescence microscopy **(D, E)**. **(A)** and **(D)** — before treatment, **(B)** — immediately after treatment, **(C)** and **(E)** — 24 h after treatment. The scale bar is 0.5 mm. The tumor site is marked with a dotted circle

(elastographic OCT images). A possibility of using MM OCT for the assessment of antitumor treatment was demonstrated convincingly. Other researchers explore isolated OCT modalities. For example, optical coherence elastography and its application in ophthalmology have been studied in the USA since 2000 [14, 15, 20, 21]. The leading positions in this area of research are held by the Australian team of D. Sampson [12, 22]. An outstanding contribution to the improvement of OCT-based visualization of tissue microcirculation (capillary vessels, in particular) has been made by the research groups headed by M. Leahy [23], R. Wang [24] and A. Vitkin [25]. Vascular response to PDT has also been studied [26, 27].

At the moment, OCT is a verified method for visual assessment of structural changes in skin cancers treated with PDT and a follow-up tool for monitoring tumor margins [28, 29]. However, certain changes in the tumor cell profile registered on OCT images are not visible to the unaided eye; here, quantitative assessment of OCT images can be more reliable. This approach has largely contributed to the diagnosis accuracy [18]. IDF calculation for the assessment of tumor response to PDT helps to accurately analyze the obtained images, describe the underlying mechanism of tumor cell death and stroma degradation and understand the role of inflammatory cells in this process.

MM OCT monitoring of tumor growth detected gradual development of the vascular network in the tumor. Apparently, the degree of tumor vascularization can influence the choice of treatment plan: in well vascularized tumors the photosensitizer will accumulate in larger concentrations, and such tumors can be successfully destroyed with PDT that affects the vasculature.
We have demonstrated that simultaneous use of three OCT modalities in tumor studies provides information on both the structure of tissue consisting of collagen fibers and blood vessels and its stiffness. Altogether, these data are important for the accurate assessment of tumor response to therapy. We believe that particular focus should be drawn to studying the tumor prior to treatment, as initial imaging results can influence the choice of treatment strategy. For example, poorly vascularized tumors are most likely hypoxic; here, radiation or PDT will be ineffective, chemotherapy drugs will not accumulate in the tumor properly, and targeted delivery of medication will be required.

CONCLUSIONS

We have demonstrated the potential of multimodal optical coherence tomography as a basis for the personalized antitumor treatment using photodynamic therapy as an example. Based on the analysis of scattering and polarizing properties of tissues, CP OCT provides data on tissue structure and collagen fibers and detects necrotic lesions in the tumor. OCT MA allows real time visualization of the vasculature in normal and tumor tissues and can be used to assess the functional state of blood vessels. Observing the response of tumor vasculature to treatment right after its completion allows for the adjustments to the treatment plan in case the vascular response is absent. We have tested a novel robust method of obtaining elastographic images that can be employed to generate deformation maps in vivo using manual probing, which is highly important for clinical studies. The complex assessment of tissues based on MM OCT is a huge step towards personalized treatment of cancers.

References

1. Casas A, Di Venosa G, Hasan T, Al Batlle. Mechanisms of resistance to photodynamic therapy. Curr Med Chem. 2011; 18 (16): 2486–515.
2. Mallidi S, Watanabe K, Timerman D, Schoenfeld D, Hasan T. Prediction of Tumor Recurrence and Therapy Monitoring Using Ultrasound-Guided Photoacoustic Imaging. Theranostics. 2015 Jan 1; 5 (3): 289–301.
3. Huang D, Swanson EA, Lin CP, Schuman S, Stinson WG, Chang W, et al. Optical coherence tomography. Science. 1991 Nov 22; 254 (5035): 1178–81.
4. Schmitt JM, Xiang SH. Cross-polarized backscatter in optical coherence tomography of biological tissue. Opt Lett. 1998 Jul 1; 23 (13): 1060–2.
5. Bouma BE, Tearney GJ. Clinical imaging with optical coherence tomography. Acad Radiol. 2002 Aug; 9 (8): 942–53.
6. Zagaynova EV, Gladkova ND, Shakhova NM, Streltsova OS, Kuznetsova IA, Yanvareva IA, et al. Optical Coherence Tomography Monitoring of Surgery in Oncology. In: Popp J, Tuchin V, Chiou A, Heinemann SH, editors. Handbook of Biophotonics. Wiley-VCH; 2012. p. 337–76.
7. Enfield J, Jonathan E, Leahy M. In vivo imaging of the microcirculation of the volar forearm using correlation mapping optical coherence tomography (cmOCT). Biomed Opt Express. 2011; 2 (5): 1184–93.
8. Mariampillai A, Leung MK, Jarvi M, Standish BA, Lee K, Wilson BC, et al. Optimized speckle variance OCT imaging of microvasculature. Opt Lett. 2010; 35 (8): 1257–9.
9. Kennedy BF, Hillman TR, McLaughlin RA, Quirk BC, Sampson DD. In vivo dynamic optical coherence elastography using a ring actuator. Opt Express. 2009; 17 (24): 21762–72.
10. Wang S, Li J, Manapuram RK, Menodiado FM, Ingram DR, Twa MD, et al. Noncontact measurement of elasticity for the detection of soft-tissue tumors using phase-sensitive optical coherence tomography combined with a focused air-puff system. Opt Lett. 2012; 37 (24): 5184–6.
11. Srivastava A, Verma Y, Rao K, Gupta P. Determination of elastic properties of resected human breast tissue samples using optical coherence tomographic elastography. Strain. 2011; Feb 1; 47 (1): 75–87.
12. Kennedy KM, McLaughlin RA, Kennedy BF, Tien A, Latham B, Saunders CM, et al. Needle optical coherence elastography for the measurement of microscale mechanical contrast deep within human breast tissues. J Biomed Opt. 2013; 18 (12): 121510.
13. Kennedy BF, McLaughlin RA, Kennedy KM, Chin L, Wijesinghe P, Curatolo A, et al. Investigation of Optical Coherence Micro-elastography as a Method to Visualize Cancers in Human Breast Tissue. Cancer Res. 2015; 75 (16): 3236–45.
14. Wang S, Larin KV, Li J, Vantipalli S, Manapuram RK, Aglyamov S, et al. A focused air-pulse system for optical-coherence-tomography-based measurements of tissue elasticity. Laser Physics Letters. 2013; 10 (7): 075605.
15. Nguyen TM, Song S, Arnal B, Wong EY, Huang Z, Wang RK, et al. Shear wave pulse compression for dynamic elastography using phase-sensitive optical coherence tomography. J Biomed Opt. 2014; 19 (1): 016013.
16. Zaitsev VY, Matveyev AL, Matveev LA, Gelikonov GV, Gubarkova EV, Gladkova ND, et al. Hybrid method of strain estimation in optical coherence elastography using combined sub-wavelength phase measurements and supra-pixel displacement tracking. J Biophotonics. 2016; 9 (5): 499–509.
17. Gubarkova EV, Dudenkova VV, Feldchtein FI, Timofeeva LB, Kiseleva EB, Kuznetsov SS, et al. Multi-modal optical imaging characterization of atherosclerotic plaques. J Biophotonics. 2015 Nov 25. doi: 10.1002/jbio.201500223.

18. Kiseleva E, Kirillin M, Feldchtein F, Vitkin A, Sergeeva E, Zagaynova E, et al. Differential diagnosis of human bladder mucosa pathologies in vivo with cross-polarization optical coherence tomography. Biomed Opt Express. 2015; Apr 1; 6 (4): 1464–76.
19. Matveev LA, Zaitsev VYu, Gelikonov GV, Matveyev AL, Moiseev AA, Ksenofontov SYu, et al. Hybrid M-mode-like OCT imaging of three-dimensional microvasculature in vivo using reference-free processing of complex valued B-scans. Opt Lett. 2015; 40 (7): 1472–5.
20. Rogowska J, Patel N, Plummer S, Brezinski ME. Quantitative optical coherence tomographic elastography: method for assessing arterial mechanical properties. Br J Radiol. 2006; 79 (945): 707–11.
21. Song S, Huang Z, Nguyen TM, Wong EY, Arnal B, O'Donnell M, et al. Shear modulus imaging by direct visualization of propagating shear waves with phase-sensitive optical coherence tomography. J Biomed Opt. 2013; 18 (12): 121509.
22. Adie SG, Kennedy BF, Armstrong JJ, Alexandrov SA, Sampson DD. Audio frequency in vivo optical coherence elastography. Phys Med Biol. 2009; 54 (10): 3129–39.
23. Jonathan E, Enfield J, Leahy MJ. Correlation mapping method for generating microcirculation morphology from optical coherence tomography (OCT) intensity images. J Biophotonics. 2011; Sep; 4 (9): 583–7.
24. Jung Y, Dziennis S, Zhi Z, Reif R, Zheng Y, Wang RK. Tracking Dynamic Microvascular Changes during Healing after Complete Biopsy Punch on the Mouse Pinna Using Optical Microangiography. PLoS ONE. 2013; 8 (2): e57976.
25. Li H, Standish BA, Mariampillai A, Munce NR, Mao Y, Chiu S, et al. Feasibility of Interstitial Doppler Optical Coherence Tomography for In Vivo Detection of Microvascular Changes During Photodynamic Therapy. Lasers Surg Med. 2006; Sep 1; 38 (8): 754–61.
26. Standish BA, Lee KKC, Jin X, Mariampillai A, Munce NR, Wood MFG, et al. Interstitial Doppler Optical Coherence Tomography as a Local Tumor Necrosis Predictor in Photodynamic Therapy of Prostatic Carcinoma: An In vivo Study. Cancer Res. 2008; Dec 1; 68 (23): 9987–95.
27. Standish BA, Yang VX, Munce NR, Wong Kee Song LM, Gardiner G, Lin A, et al. Doppler optical coherence tomography monitoring of microvascular tissue response during photodynamic therapy in an animal model of Barrett's esophagus. Gastrointest Endosc. 2007; 66 (2): 326–33.
28. Hamdoon Z, Jerjes W, Upile T, Hopper C. Optical coherence tomography-guided photodynamic therapy for skin cancer: case study. Photodiagnosis Photodyn Ther. 2011; 8 (1): 49–52.
29. Themstrup L, Banzhaf CA, Mogensen M, Jemec GB. Optical coherence tomography imaging of non-melanoma skin cancer undergoing photodynamic therapy reveals subclinical residual lesions. Photodiagnosis Photodyn Ther. 2014; 11 (1): 7–12.

Литература

1. Casas A, Di Venosa G, Hasan T, Al Batlle. Mechanisms of resistance to photodynamic therapy. Curr Med Chem. 2011; 18 (16): 2486–515.
2. Mallidi S, Watanabe K, Timerman D, Schoenfeld D, Hasan T. Prediction of Tumor Recurrence and Therapy Monitoring Using Ultrasound-Guided Photoacoustic Imaging. Theranostics. 2015 Jan 1; 5 (3): 289–301.
3. Huang D, Swanson EA, Lin CP, Schuman S, Stinson WG, Chang W, et al. Optical coherence tomography. Science. 1991 Nov 22; 254 (5035): 1178–81.
4. Schmitt JM, Xiang SH. Cross-polarized backscatter in optical coherence tomography of biological tissue. Opt Lett. 1998 Jul 1; 23 (13): 1060–2.
5. Bouma BE, Tearney GJ. Clinical imaging with optical coherence tomography. Acad Radiol. 2002 Aug; 9 (8): 942–53.
6. Zagaynova EV, Gladkova ND, Shakhova NM, Streltsova OS, Kuznetsova IA, Yanvareva IA, et al. Optical Coherence Tomography Monitoring of Surgery in Oncology. В книге: Popp J, Tuchin V, Chiou A, Heinemann SH, editors. Handbook of Biophotonics. Wiley-VCH; 2012. p. 337–76.
7. Enfield J, Jonathan E, Leahy M. In vivo imaging of the microcirculation of the volar forearm using correlation mapping optical coherence tomography (cmOCT). Biomed Opt Express. 2011; 2 (5): 1184–93.
8. Mariampillai A, Leung MK, Jarvi M, Standish BA, Lee K, Wilson BC, et al. Optimized speckle variance OCT imaging of microvasculature. Opt Lett. 2010; 35 (8): 1257–9.
9. Kennedy BF, Hillman TR, McLaughlin RA, Quirk BC, Sampson DD. In vivo dynamic optical coherence elastography using a ring actuator. Opt Express. 2009; 17 (24): 21762–72.
10. Wang S, Li J, Manapuram RK, Menodiado FM, Ingram DR, Twa MD, et al. Noncontact measurement of elasticity for the detection of soft-tissue tumors using phase-sensitive optical coherence tomography combined with a focused air-puff system. Opt Lett. 2012; 37 (24): 5184–6.
11. Srivastava A, Verma Y, Rao K, Gupta P. Determination of elastic properties of resected human breast tissue samples using optical coherence tomographic elastography. Strain. 2011; Feb 1; 47 (1): 75–87.
12. Kennedy KM, McLaughlin RA, Kennedy BF, Tien A, Latham B, Saunders CM, et al. Needle optical coherence elastography for the measurement of microscale mechanical contrast deep within human breast tissues. J Biomed Opt. 2013; 18 (12): 121510.
13. Kennedy BF, McLaughlin RA, Kennedy KM, Chin L, Wijesinghe P, Curatolo A, et al. Investigation of Optical Coherence Micro-elastography as a Method to Visualize Cancers in Human Breast Tissue. Cancer Res. 2015; 75 (16): 3236–45.
14. Wang S, Larin KV, Li J, Vantipalli S, Manapuram RK, Aglyamov S, et al. A focused air-pulse system for optical-coherence-tomography-based measurements of tissue elasticity. Laser Physics Letters. 2013; 10 (7): 075605.
15. Nguyen TM, Song S, Arnal B, Wong EY, Huang Z, Wang RK, et al. Shear wave pulse compression for dynamic elastography using phase-sensitive optical coherence tomography. J Biomed Opt. 2014; 19 (1): 016013.
16. Zaitsev VY, Matveyev AL, Matveev LA, Gelikonov GV, Gubarkova EV, Gladkova ND, et al. Hybrid method of strain estimation in optical coherence elastography using combined sub-wavelength phase measurements and supra-pixel displacement tracking. J Biophotonics. 2016; 9 (5): 499–509.
17. Gubarkova EV, Dudenkova VV, Feldchtein FI, Timofeeva LB, Kiseleva EB, Kuznetsov SS, et al. Multi-modal optical imaging characterization of atherosclerotic plaques. J Biophotonics. 2015 Nov 25. doi: 10.1002/jbio.201500223.
18. Kiseleva E, Kirillin M, Feldchtein F, Vitkin A, Sergeeva E, Zagaynova E, et al. Differential diagnosis of human bladder mucosa pathologies in vivo with cross-polarization optical coherence tomography. Biomed Opt Express. 2015; Apr 1; 6 (4): 1464–76.
19. Matveev LA, Zaitsev VYu, Gelikonov GV, Matveyev AL, Moiseev AA, Ksenofontov SYu, et al. Hybrid M-mode-like OCT imaging of three-dimensional microvasculature in vivo using reference-free processing of complex valued B-scans. Opt Lett. 2015; 40 (7): 1472–5.
20. Rogowska J, Patel N, Plummer S, Brezinski ME. Quantitative optical coherence tomographic elastography: method for assessing arterial mechanical properties. Br J Radiol. 2006; 79 (945): 707–11.
21. Song S, Huang Z, Nguyen TM, Wong EY, Arnal B, O'Donnell M, et al. Shear modulus imaging by direct visualization of propagating shear waves with phase-sensitive optical coherence tomography. J Biomed Opt. 2013; 18 (12): 121509.
22. Adie SG, Kennedy BF, Armstrong JJ, Alexandrov SA, Sampson DD. Audio frequency in vivo optical coherence

elastography. Phys Med Biol. 2009; 54 (10): 3129–39.
23. Jonathan E, Enfield J, Leahy MJ. Correlation mapping method for generating microcirculation morphology from optical coherence tomography (OCT) intensity images. J Biophotonics. 2011; Sep; 4 (9): 583–7.
24. Jung Y, Dziennis S, Zhi Z, Reif R, Zheng Y, Wang RK. Tracking Dynamic Microvascular Changes during Healing after Complete Biopsy Punch on the Mouse Pinna Using Optical Microangiography. PLoS ONE. 2013; 8 (2): e57976.
25. Li H, Standish BA, Mariampillai A, Munce NR, Mao Y, Chiu S, et al. Feasibility of Interstitial Doppler Optical Coherence Tomography for In Vivo Detection of Microvascular Changes During Photodynamic Therapy. Lasers Surg Med. 2006; Sep 1; 38 (8): 754–61.
26. Standish BA, Lee KKC, Jin X, Mariampillai A, Munce NR, Wood MFG, et al. Interstitial Doppler Optical Coherence Tomography as a Local Tumor Necrosis Predictor in Photodynamic Therapy of Prostatic Carcinoma: An In vivo Study. Cancer Res. 2008; Dec 1; 68 (23): 9987–95.
27. Standish BA, Yang VX, Munce NR, Wong Kee Song LM, Gardiner G, Lin A, et al. Doppler optical coherence tomography monitoring of microvascular tissue response during photodynamic therapy in an animal model of Barrett's esophagus. Gastrointest Endosc. 2007; 66 (2): 326–33.
28. Hamdoon Z, Jerjes W, Upile T, Hopper C. Optical coherence tomography-guided photodynamic therapy for skin cancer: case study. Photodiagnosis Photodyn Ther. 2011; 8 (1): 49–52.
29. Themstrup L, Banzhaf CA, Mogensen M, Jemec GB. Optical coherence tomography imaging of non-melanoma skin cancer undergoing photodynamic therapy reveals subclinical residual lesions. Photodiagnosis Photodyn Ther. 2014; 11 (1): 7–12.

DYNAMIC CONTRAST-ENHANCED MRI IN DETERMINING HISTOLOGICAL TYPE OF CERVICAL CANCER

Tarachkova EV[1] ✉, Shorikov MA[1,2], Panov VO[1,2], Kuznetsov VV[2], Tyurin IE[1,2], Shimanovsky NL[3]

[1] Department of Roentgenology and Radiology,
Russian Medical Academy of Postgraduate Education, Moscow, Russia

[2] Blokhin Russian Cancer Research Center, Moscow, Russia

[3] P. V. Sergeev Molecular Pharmacology and Radiobiology Department, Biomedical Faculty,
Pirogov Russian National Research Medical University, Moscow, Russia

Knowing the histology of cervical cancer (squamos cell carcinoma or adenocarcinoma) is important in deciding on the best treatment plan. We have studied the role of dynamic contrast-enhanced magnetic resonance imaging in the differential diagnosis of cervical cancer. We examined 90 patients between 23 and 78 years of age (mean age was 43.5 years) with histologically distinctive stage IIb–IVb cervical cancers. Scanning was performed on Magnetom Espree 1.5T and Magnetom Skyra 3.0T scanners (Siemens, Germany) using gadobutrol (Gadavist by Bayer, Germany). On T1-weighted images, signal intensity and its rate of change were significantly higher for adenocarcinomas compared to squamos cell carcinomas ($p < 0.04$) from the 20th second after gadobutrol had been delivered to the tumor. With squamos cell carcinomas, the time-intensity curve (showing the dependence of signal intensity on the time elapsed after gadobutrol had been delivered to the tumor) had two phases: a short phase of a relatively slow accumulation of the contrast agent with the subsequent plateau or even signal intensity reduction. The pattern of gadobutrol accumulation allows differentiating between histological types of tumors. Based on the resulting curves, a pharmacokinetic model can be described for each tumor type. Postcontrast images are useful in determining tumor differentiation grade. Specifically, the signal from a well-differentiated adenocarcinoma is the most inhomogeneous one ($p < 0.03$). The method described in this work does not imply that histological analysis is unnecessary and can be recommended as a supplementary diagnostic tool.

Keywords: magnetic resonance imaging, contrast enhancement, gadobutrol, cervical cancer, adenocarcinoma, squamos cell carcinoma, differential diagnosis

✉ **Correspondence should be addressed:** Elena Tarachkova
ul. Barrikadnaya, d. 2/1, str. 1, Moscow, Russia, 123995; doctorkid@yandex.ru

Received: 10.08.2016 **Accepted:** 18.08.2016

ВОЗМОЖНОСТИ ДИНАМИЧЕСКОЙ МРТ С КОНТРАСТНЫМ УСИЛЕНИЕМ В ОПРЕДЕЛЕНИИ ГИСТОЛОГИЧЕСКОГО ТИПА РАКА ШЕЙКИ МАТКИ

Е. В. Тарачкова[1]✉, М. А. Шориков[1,2], В. О. Панов[1,2], В. В. Кузнецов[2], И. Е. Тюрин[1,2], Н. Л. Шимановский[3]

[1] Кафедра рентгенологии и радиологии,
Российская медицинская академия последипломного образования, Москва

[2] Российский онкологический научный центр имени Н. Н. Блохина, Москва

[3] Кафедра молекулярной фармакологии и радиобиологии имени акад. П. В. Сергеева, медико-биологический факультет,
Российский национальный исследовательский медицинский университет имени Н. И. Пирогова, Москва

Определение гистологического типа рака шейки матки (плоскоклеточный рак или аденокарцинома) способствует выбору наиболее эффективной терапии. В работе описан метод дифференциальной диагностики заболевания с использованием динамической магнитно-резонансной томографии с контрастным усилением. Были обследованы 90 пациенток в возрасте 23–78 лет (средний возраст — 43,5 года) с гистологически подтвержденным раком шейки матки стадий IIb–IVb. Сканировали на аппаратах Magnetom Espree 1.5T и Magnetom Skyra 3.0T (Siemens, Германия), используя гадобутрол («Гадовист», Bayer, Германия). На Т1-взвешенных изображениях интенсивность сигнала и скорость ее изменения, начиная с 20 с после появления гадобутрола в опухоли, были достоверно выше для аденокарцином, чем для плоскоклеточного рака ($p < 0,04$). При этом для плоскоклеточного рака наблюдали две фазы на кривых зависимости интенсивности сигнала от времени после появления гадобутрола в опухоли: короткую фазу относительно медленного накопления контрастного вещества с последующим выходом на плато или даже снижением сигнала к концу наблюдения (125 с). Именно характер накопления гадобутрола позволяет различать гистологические типы опухолей, и на основе соответствующих кривых могут быть предложены фармакокинетические модели для опухолей разных типов. Постконтрастные изображения полезны для определения степени дифференцировки опухоли. В частности, сигнал от высокодифференцированных аденокарцином достоверно наиболее неоднородный ($p < 0,03$). Описанный метод не исключает гистологической верификации диагноза и может быть рекомендован как дополнительный диагностический инструмент.

Ключевые слова: магнитно-резонансная томография, контрастное усиление, гадобутрол, рак шейки матки, аденокарцинома, плоскоклеточный рак, дифференциальная диагностика

✉ **Для корреспонденции:** Тарачкова Елена Владимировна
123995, г. Москва, ул. Баррикадная, д. 2/1, стр. 1; doctorkid@yandex.ru

Статья получена: 10.08.2016 **Статья принята в печать:** 18.08.2016

Cervical cancer (CC) remains a troubling health issue among women of reproductive age [1–6]. About 70–80 % of patients with invasive CC are diagnosed with squamous cell carcinoma; 10–20 % are diagnosed with adenocarcinoma [6, 7]. Adenocarcinomas tend to grow more aggressively, form distant metastases more frequently, demonstrate lower five-year survival rates, and require an alternative approach to treatment, specifically, when deciding on chemotherapy drugs [8]. Knowing CC histologic type would ensure timely and effective treatment.

Compared to CT and PET-CT, magnetic resonance imaging (MRI) has some advantages in detecting and staging localized CC; in case of advanced CC, CT and MRI are equally effective. PET-CT is recommended for the detection of recurrences and metastases in lymph nodes [1, 9, 10]. To differentiate between benign and malignant tumors, dynamic contrast-enhanced MRI (DCEMRI) is widely used [1]; however, this technique has not yet been applied to assess CC histologic types. To attempt such assessment, diffusion weighted MR images (DWIs) and apparent diffusion coefficient maps (ADC-maps) were used [11, 12]. Now, we hypothesized that DCEMRI images can be of a higher diagnostic value in the preoperative assessment of the histologic type of cervical cancer (squamous cell carcinoma or adenocarcinoma) and, possibly, tumor grade, compared to DWIs and ADC-mapping or T2-weighted images. Our work addresses the following objectives:

– detecting differences between DCEMRI-based intensity curves of gadobutrol accumulation for various histologic types of CC;

– detecting differences in the intensity and homogeneity of signals from various histologic types of tumor tissues using delayed postcontrast DCEMRI images;

– detecting differences in the signal intensity between various histologic types of CC using fat-suppressed and fat-unsuppressed T2WIs;

– estimating sensitivity and specificity of DCEMRI in the assessment of CC histologic type and grade.

METHODS

The study was carried out at N. N. Blokhin Russian Cancer Research Center. It enrolled 90 women aged 23–78 (mean age of 43.5 years) with histologically confirmed IIb–IVb cervical cancer, median lesion volume of 43.3 cm^3 (22.6 and 92.9 are the 1st and 3rd quantiles, respectively). Patients were distributed into groups depending on CC histologic type and tumor grade, as shown in table 1. Differences in age and lesion volumes between the groups were statistically insignificant ($p > 0.05$).

The following inclusion criteria were applied: suspicion of CC and a need for an adequate treatment plan in confirmed cases; a verified diagnosis of CC requiring a subsequent determination of tumor size, invasion depth, parametrial infiltration, and damage to lymph nodes and surrounding tissues; elevated levels of squamous cell carcinoma antigen (SCCA) in patients with ambiguous results of transvaginal ultrasound examination. Exclusion criteria were as follows: poor general condition of a patient (somatic and pshycic health) that prevented her from lying still during the scan; hypersensitivity to the components of magnetic resonance contrast agents (MRCAs); metal implants or implanted electronic devices (clips, pacemakers); claustrophobia; serious cardiovascular conditions; renal insufficiency (glomerular filtration rate of <30 ml/min); liver failure; patient's weight exceeding the maximum weight capacity of the MRI bed.

The patients were asked to stop eating gas-producing foods two days before the scan. A day before the scan, they were asked to take a standard dose of a laxative, and/or were administered an edema 12 h before the procedure. On the day of the examination, the patients were allowed to have a light breakfast rich in carbohydrates and a minimal amount of liquid (no later than 2 h before the examination). The patients took 40–80 mg of an antispasmodic (drotaverine marketed as No-Spa, by Research Institute of Organic Intermediates and Dyes, Russia) *per os* or, if they were not prone to constipation, 10 mg of hyoscine butylbromide, an antiperistaltic drug (Buscopan Boehringer Ingelheim, Germany). The patients were asked to have their urinary bladder filled with only a small amount of fluid for the scan.

Scans were carried out on Magnetom Espree 1.5T and Magnetom Skyra 3.0T scanners (Siemens, Germany) using a multichannel 12-element receiver body coil placed on the pelvis and centered 2–3 cm above the pubis, with patients in the supine position. The following axial image types were used:

1. fat-unsuppressed T2-weighted images (T2WIs);
2. fat-suppressed T2WIs;

Table 1. Distribution of patients with cervical cancer into groups according to tumor histologic type and grade

Parameter	Squamous cell carcinoma			Adenocarcinoma		
Number of patients	74			16		
Median age (quantile 1, quantile 3), years	42 (36; 50)			54 (39; 54)		
Median lesion volume (quantile 1, quantile 3), cm^3	43.6 (22,3; 95,2)			42.2 (24.4; 89.4)		
	Tumor grade					
	low	intermediate grade	high	low	intermediate grade	high
Number of patients	24	22	6	5	5	5
Median age (quantile 1, quantile 2), years	37 (35; 43)	44 (37; 48)	38 (35; 41)	59 (54; 62)	45 (39; 48)	56 (39; 58)
Median lesion volume (quantile 1, quantile 2), cm^3	43,6 (36.5; 114.6)	57.6 (40.2; 211.9)	63,6 (19.8; 166.3)	87,9 (56.4; 206.1)	38,2 (30.1; 72.1)	54,7 (35.3; 74.2)
FIGO stage FIGO IIa, %	28.6	33.3	–	–	50.0	50.0
FIGO stage FIGO IIIa, %	19.0	27.8	80.0	–	–	50.0
FIGO stage FIGO IIIb, %	23.8	27.8	20.0	75.0	25.0	–
FIGO stage FIGO IVa, %	19.0	5.6	–	–	–	–
FIGO stage FIGO IVb, %	9.5	5.6	–	25.0	25.0	–

Note. Lesion volume was measured directly (the sum of tumor square areas on T2-weighted images multiplied by section thickness). Grading was performed in 67 patients.

3. fat-suppressed DWIs with automatic ADC-mapping based on b-factor values of 50, 800 and 1000;

4. unenhanced T1-weighted images (T1WIs);

5. frequency-selective fat-suppressed T1WIs obtained during DCEMRI (keyhole imaging) [13], 35 series of 4.8 s each, in total. To reduce the contribution of fat-suppressed signal heterogeneity and to accurately detect MRCA accumulation zone, unenhanced images were subtracted from MRCA-enhanced images obtained at different time points after MRCA administration. After MRCA was delivered to the tumor, the observation lasted for 125 s;

6. fat-suppressed delayed T1WIs obtained 3–4 minutes after MRCA administration.

Technical parameters of the used sequences are shown in table 2.

For DCEMRI, the patients received a 7.5 ml injection of 1.0 M water-soluble extracellular MRCA gadobutrol (Gadovist by Bayer, Germany), which is about 0.1 mmol/kg of a patient's weight, at a rate of 2.5–3.0 ml/s. Double concentration of gadolinium in this formulation allows administering a lower amount of this drug and still obtaining high quality images, as gadolinium is highly reactive [14]. Gadobutrol is a macrocyclic gadolinium-containing formulation with a low risk of inducing nephrogenic systemic fibrosis [15].

The following parameters were evaluated using MR images:

• signal intensity, i. e., how bright or dark the object is, compared to the surrounding tissues; besides, during quantitative analysis, mean signal intensity (SI) in the region of interest (ROI) was measured (in arbitrary units);

• signal heterogeneity, i.e., non-uniformity of the object's signal distribution against the surrounding tissues; during quantitative analysis, we also assessed the range of signal intensity values within ROI. Those values can be treated as the absolute standard deviation of signal intensity (SDOSI, a. u.) or a ratio of standard deviation to signal intensity (a nondimensional value) within ROI.

According to the description, these parameters are available for simple visual assessment. However, we can also find their reference range using a standard interface of the workstation. To measure changes in signal intensity on all image types, we used SI and SDOSI data from the manually selected ROIs of cervical cancer tissue and gluteus maximus muscle (MR signal was normalized to the muscle signal from regions no bigger than 15 pixels in size). Thus, signal intensity was additionally evaluated as a ratio of SI in the tumor region to muscle SI.

After subtracting unenhanced MR-images from enhanced MR-images, we built time-curves based on DCEMRI data (fig. 1) showing changes in SI and its SD and calculated SI and SD in the same areas using postcontrast images obtained in the delayed phase. For each curve, a point of inflexion was determined, past which the rate of MRCA accumulation changed. We drew tangent lines to the initial and finishing curve segments, and their intersection point was considered an inflexion point (a point where the rate of signal intensity changes). Because the position of the inflexion point varied, it was taken as zero time point t for further calculations. However, the tables in this article show time elapsed after gadobutrol delivery to the tumor. Relative signal intensity, RSI(t), was calculated according to the following formula:

$$RSI(t) = \frac{SI(t) - SI(0)}{SI(0)} \times 100\ \%,$$

where RSI(t) is relative signal intensity at a given time point *t* after the inflextion point; SI(0) is signal intensity at inflexion point, SI(t) is signal intensity at a given time point *t* (here, we use *t* = 15, 30, 60 and 110 s after the inflexion point).

Statistical processing was done using Miscrosoft Excel 10 software with Addinsoft XLStat addon (Addinsoft, USA) and Statistica 10.0 (StatSoft, USA) using Mann–Whitney, Kruskal–Wallis and Dunn tests and ROC (reciever operator curves) analysis. The study was approved by the Research Ethics Committee of the Russian Medical Academy of Postgraduate Education (Protocol 8 dated June 14, 2016).

RESULTS

After MRCA administration, we observed a 10–20 s period (median of 15 s) of rapid and vigorous accumulation of the contrast agent in tumors of both types, with a corresponding change in SI after gadobutrol delivery to the tumor (fig. 2). This phase ended at the inflexion point of the time-SI curve. Past this point, adenoarcinomas exhibited a more intense MR-signal change followed by a more rapid uniform accumulation of gadobutrol ($p < 0.003$–0.040). For squamous cell carcinomas, MR signal intensity was lower 15 s after MRCA administration;

Table 2. MR-sequences used in the study and their parameters

Image type	Fat suppression	Sequence type and extra parameters	Slice thickness, mm	Field of view (side), mm	Matrix, pixel x pixel	TR/TE, ms	Number of accumulations
T2WI	No suppression or frequency-selective suppression	Turbo spin echo, acceleration factor is 17	3	320	384 x 384	6300–8000/132	1
DWI + ADC-maps	Selective suppression with inverting pulse	Echoplanar imaging, diffusion weighted imaging b-value is 50, 800, 1000	3–4	400	96 x 196	370/82	6
T1WI before MRCA injection, T1WI after MRCA injection in the delayed phase (3–4 minutes after the injection)	Frequency-selective suppression	Volumetric interpolated examination, flip angle is 10°	2	240	243 x 320	5.94/2.08	1
DCEMRI T1WI	Frequency-selective suppression	Time resolved imaging with stochastic trajectories, flip angle is 12°, k-space central and peripheral acquisition A is 51 % and B is 21 %, total observation time is 125 s	3	260	192 x 256	466/186	1

for the time-SI curve, two phases were typical: a short phase of relatively slow accumulation of the contrast agent (60 s past the inflexion point or 15 to 75 s after gadobutrol delivery to the tumor) with subsequent plateau or even MR signal reduction observed at second 125 after gadobutrol delivery to the tumor.

Differences between adenocarcinoma and squamous cell carcinoma detected during the analysis of SI and SDOSI on fat-suppressed T2WIs and then on T1WIs obtained during DCEMRI and in the delayed phase after MRCA administration are shown in tables 3 and 4. On fat-suppressed T2WIs, adenomas are characterized by a more intense and more homogenous signal, compared to squamous cell carcinomas ($p < 0.03–0.05$). With DCEMRI, SI and its rate of change on T1WIs were significantly higher for adenocarcinomas ($p < 0.003–0.040$) 20 s after gadobutrol had been delivered to the tumor and thereafter. On postcontrast images obtained during the delayed phase, poorly differentiated adenocarcinomas are characterized by a more homogenous signal compared to moderately and well-differentiated adenocarcinomas and squamous cell carcinomas of any grade, while for well-differentiated adenocarcinomas, a more heterogenous signal is typical, compared to adenocarcinomas and squamous cell carcinomas of any grade ($p < 0.03$). No significant differences were found for squamos cell carcinomas.

Due to an additional inflexion point appearing on the squamous cell carcinoma curve (around second 75 after gadobutrol delivery to the tumor), we also assessed the ratio of signal intensity at this time point to signal intensity at the end point (second 125). For squamous cell carcinoma, this ratio was close to 1 (plateau), for adenocarcinoma it was 1.1 ($p < 0.02$). This parameter and relative signal intensity 75 s after gadobutrol delivery to the tumor turned to be the most sensitive and specific (table 3). With optimized accuracy (a maximum sum of sensitivity and specificity), it was 0.75 for tumors of both types.

ROC-analysis also confirmed that specifics of gadobutrol accumulation best characterize the histologic type of a tumor. Additional parameters that were significantly different for adenocarcinomas and squamous cell carcinomas obtained from fat-suppressed T2WIs (SI absolute value, SI of the tumor normalized to the SI of the gluteus, and SDOSI) must be considered secondary. To understand their contribution, a model was built based on the binary logistic regression. It allowed for the assessment of total sensitivity and specificity of the method while using a combination of parameters: after frequency optimization, their values for adenocarcinoma were 0.80 and 0.86, respectively, and for squamous cell carcinoma — 0.86 and 0.80, respectively.

Postcontrast images in the delayed phase were useful in the assessment of tumor grade: they allow for highly sensitive and specific discrimination between poorly and well-differentiated adenocarcinomas. The former are characterized by a more homogenous signal; their sensitivity and specificity for a 0.90 area under ROC curve are 0.75 and 0.96, respectively. The latter are characterized by a more heterogeneous signal and are detected with 1.00 sensitivity and 0.83 specificity for a 0.88 area under ROC curve.

With ADC mapping, no significant differences were detected between tumors of two studied types of 15–30 pixels in size ($p = 0.21$).

DISCUSSION

Results obtained by other researchers in quite large samples (80 and 112 patients) demonstrated the possibility of detecting significant differences between adenicarcinomas and squamous cell carcinomas of various grades using the ADC mapping technique [11, 12]. The authors emphasize that MRI scans can contribute to a more accurate diagnosis or verify histological data, thus preventing medical errors. However, in both experiments mean ADC was calculated for the entire tumor, meaning that each slice where cervical cancer was detected had to be processed. This kind of analysis is quite time-consuming and can hardly be recommended for clinical use even in big specialized centers. We failed to establish a connection between ADC and tumor histologic type using a simpler measurement technique (ROI of 15–30 pixels). Besides, an accurate and precise ADC map is difficult to reproduce and construct, especially when only 2 or 3 b-factor values [16–18]. Our technique is simpler and easy to apply. DCEMRI here matters not only for the diagnosis but for the prognosis of CC outcome. Lund et al. [19] report low levels

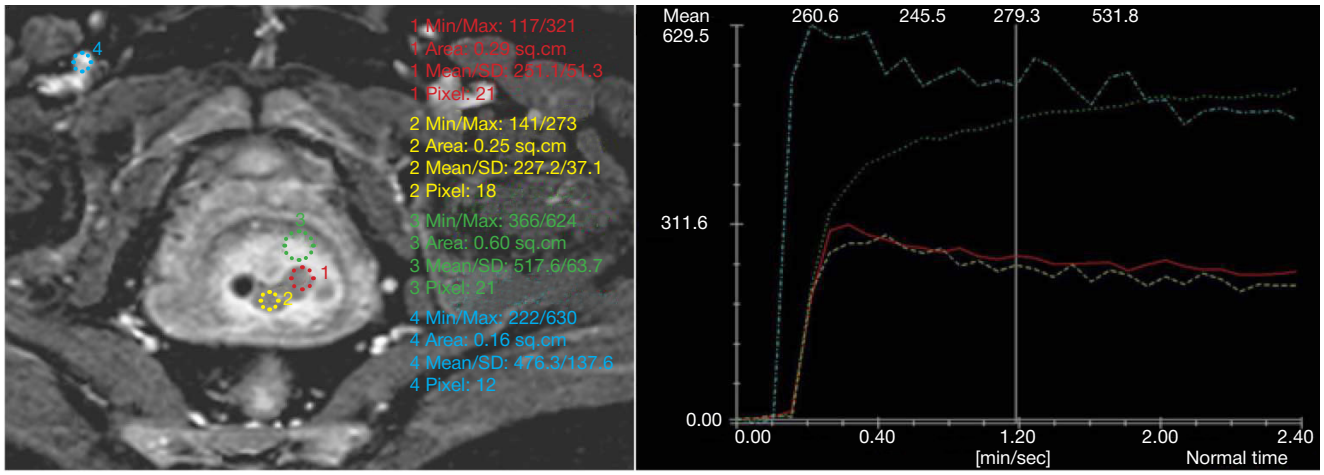

Fig. 1. Magnetic resonance contrast agent accumulation curves obtained on the scanner workstation

An axial section is on the left, obtained from a dynamic contrast-enhanced MR image (80 s after scanning was launched) of a patient with squamous cell carcinoma. Regions of interest (ROIs) are shown in different colors. The yellow (1) and red (2) circles show cervical cancer, the green (3) circle shows intact myometrium, the blue circle (4) shows a blood vessel. Signal intensity-time curves based on the ROI data are shown on the right. The vertical line designates time elapsed after measurements were started (80 s). The horizontal axis shows time elapsed after contrast agent delivery to the tumor (seconds); the vertical axis shows relative signal intensity. A higher signal intensity is characteristic of intact myometrium and the vessel.

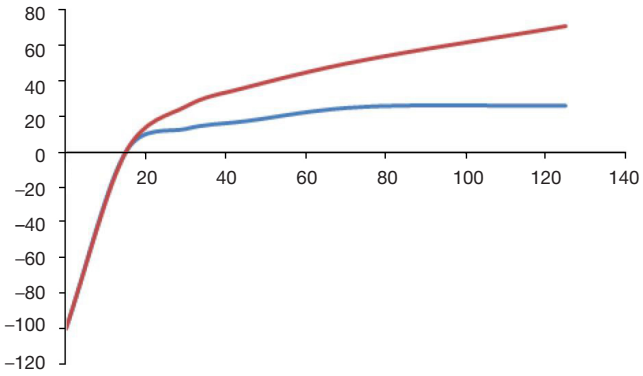

Fig. 2. A typical gadobutrol accumulation curve for two types of cervical cancer (squamous cell carcinoma and adenocarcinoma)

The horizontal axis shows time elapsed after contrast agent delivery to the tumor (seconds); the vertical axis shows relative signal intensity in tumor tissue (the red curve shows adenocarcinoma dynamics, the blue curve shows squamous cell carcinoma dynamics).

Table 3. Median values and the range of differences between studied parameters on fat-suppressed T2-weighted images and T1-weighted images after gadobutrol injection to the region of interest (no smaller than 15 pixels) for cervical cancer of two histologic types (squamous cell carcinoma and adenocarcinoma)

Parameter	p-value	Histologic type of cervical cancer	Median, a. u.	Quantile 1, a. u.	Quantile 3, a. u.
Fat-suppressed T2WI					
Tumor SI	0.05	Squamous cell carcinoma	250.38	202.38	295.11
		Adenocarcinoma	306.57	260.3	309.35
Tumor SI / Muscle SI	0.03	Squamous cell carcinoma	5.97	4.64	6.79
		Adenocarcinoma	7.17	5.37	7.81
SDOSI of tumor / SDOSI of muscle	0.02	Squamous cell carcinoma	0.15	0.11	0.18
		Adenocarcinoma	0.11	0.09	0.15
T1WI obtained during DCEMRI after MRCA administration					
RSI(30)	0.01	Squamous cell carcinoma	12.88	4.8	23.21
		Adenocarcinoma	25.68	16.27	35.13
RSI(45)	0.02	Squamous cell carcinoma	17.27	7.98	35.98
		Adenocarcinoma	36.40	19.18	46.51
RSI(75)	0.005	Squamous cell carcinoma	25.38	7.23	47.73
		Adenocarcinoma	52.11	33.53	66.17
RSI(125)	0.002	Squamous cell carcinoma	25.93	6.60	69.97
		Adenocarcinoma	71.09	41.34	100.38
SI(125) / SI(75)	0.02	Squamous cell carcinoma	1.00	0.94	1.08
		Adenocarcinoma	1.11	1.02	1.21
SDOSI(125)	0.04	Squamous cell carcinoma	42.10	33.70	81.60
		Adenocarcinoma	53.70	37.2	81.60
SDOSI(125) / SI(125)	0.02	Squamous cell carcinoma	0.15	0.11	0.21
		Adenocarcinoma	0.22	0.17	0.28

Note. SI is signal intensity; RSI(t) is relative signal intensity on T1-weighted images obtained during dynamic contrast-enhanced MRI at time point *t* (seconds) after gadobutrol delivery to the tumor; SDOSI is standard deviation of signal intensity. Significance of differences was assessed using Mann–Whitney test.

Table 4. Median standard deviation of signal intensity and its range on postcontrast T1-weighted images in the delayed phase after gadobutrol injection for cervical cancers of two histologic types (squamous cell carcinoma and adenocarcinoma) and different grades

Histologic type	Tumor grade	Median SD, a.u.	SD quantile, a.u.	SD quantile 3, a.u.
Squamous cell carcinoma	Low	47.55	37.80	52.70
	Intermediate	34.25	30.00	46.50
	High	32.10	28.70	41.40
Adenocarcinoma	Low	25.65*	24.95*	29.75*
	Intermediate	38.30	33.20	39.00
	High	57.20*	56.00*	68.10*

Note. Significance of differences was assessed using Kruskal–Wallis test and then confirmed by Dunn's paired test. * — $p < 0.03$.

of contrast enhancement during DCEMRI associated with a poorer prognosis, compared to a higher level of enhancement.

Besides, DCEMRI detected differences between MRCA accumulation curves of squamous cell carcinomas and adenocarcinomas. Therefore, it might be possible to build a two-compartment pharmacokinetic model [20] of gadobutrol accumulation (blood-tumor tissue) for adenocarcinoma, and a more complex three-compartment model for squamous cell carcinoma. The latter could be explained by the presence of (or, possibly, partial preservation of) a basement membrane on the inner mucosal layer of the cervix, and this can influence the choice of treatment, as it determines the type of blood circulation and eventually tumor bioaccessibility to chemotherapy drugs.

CONCLUSIONS

Contrast-enhanced dynamic magnetic resonance imaging allows detecting histologic type of cervical cancer (adenocarcinoma or squamous cell carcinoma) with high accuracy prior to excision using contrast agent accumulation data obtained from T1-weighted images; it also allows detecting adenocarcinoma grade based on the analysis of postcontrast images (in such adenomas, the signal is the most heterogeneous). However, our technique does not exclude the need for biopsy or other types of histological verification of the diagnosis and can be recommended as an additional diagnostic tool only.

References

1. Bourgioti C, Chatoupis K, Moulopoulos LA. Current imaging strategies for the evaluation of uterine cervical cancer. World J Radiol. 2016; 8 (4): 342–54.
2. Jemal A, Siegel R, Ward E, Hao Y, Xu J, Murray T, et. al. Cancer statistics, 2008. CA Cancer J Clin. 2008; 58 (2): 71–96.
3. Howlader N, Noone A, Krapcho M. SEER Cancer Statistics Review, 1975–2010. 2012. Available from: http://seer.cancer.gov/archive/csr/1975_2010/.
4. Siegel R, Naishadham D, Jemal A. Cancer statistics, 2013. CA Cancer J Clin. 2013; 63 (1): 11–30.
5. Axel EM. [Incidence and mortality from malignant tumors of the female reproductive system in Russia]. Gynecologic Oncology. 2012; (1): 18–23. Russian.
6. Davydov MI, Kuznetsov VV, Nechushkina MV, editors. Lektsii po onkoginekologii. Moscow: MEDpress-inform; 2009. 432 p. Russian.
7. Cervical Cancer Statistics [Internet]. London: Cancer Research UK. [cited 2016 Aug]. Available from: http://www.cancerresearchuk.org/cancer-info/cancerstats/types/cervix/.
8. Williams NL, Werner TL, Jarboe EA, Gaffney DK. Adenocarcinoma of the cervix: should we treat it differently? Curr Oncol Rep. 2015; 17 (4): 17.
9. Tarachkova EV, Streltsova ON, Panov VO, Bazaeva IY, Tyurin IE. [Multiparameter magnetic resonance imaging in the diagnosis of cancer of the cervix uteri]. Vestnik rentgenologii i radiologii. 2015; (6): 43–55. Russian.
10. Trufanov GE, Panov VO. Rukovodstvo po luchevoy diagnostike v ginekologii. Saint-Petersburg: ELBI-SPb; 2008. 592 p. Russian.
11. Kuang F, Ren J, Zhong Q, Liyuan F, Huan Y, Chen Z. The value of apparent diffusion coefficient in the assessment of cervical cancer. Eur Radiol. 2013; 23 (4): 1050–8.
12. Nakamura K, Kajitani S, Joja I, Haruma T, Fukushima C, Kusumoto T, et al. The posttreatment mean apparent diffusion coefficient of primary tumor is superior to pretreatment ADCmean of primary tumor as a predictor of prognosis with cervical cancer. Cancer Med. 2013; 2 (4): 519–25.
13. van Vaals JJ, Brummer ME, Dixon WT, Tuithof HH, Engels H, Nelson RC, et al. Keyhole method for imaging of contrast uptake. J Magn Reson Imaging. 1993; 3 (4): 671–5.
14. Gutierrez JE, Rosenberg M, Seemann J, Breuer J, Haverstock D, et al. Safety and Efficacy of Gadobutrol for Contrast-enhanced Magnetic Resonance Imaging of the Central Nervous System: Results from a Multicenter, Double-blind, Randomized, Comparator Study. Magn Reson Insights. 2015; 8: 1–10.
15. Thomsen HS, Morcos SK, Almén T, Bellin MF, Bertolotto M, Bongartz G, et al. Nephrogenic systemic fibrosis and gadolinium-based contrast media: updated ESUR Contrast Medium Safety Committee guidelines. Eur Radiol. 2013; 23 (2):307–18.
16. Koh DM, Thoeny HC, editors. Diffusion-Weighted MR Imaging: Application in The Body. Springer-Verlag Berlin Heidelberg; 2010, p. 7–16.
17. Giannotti E, Waugh S, Priba L, Davis Z, Crowe E, Vinnicombe S. Assessment and quantification of sources of variability in breast apparent diffusion coefficient (ADC) measurements at diffusion weighted imaging, Eur J Radiol. 2015; 84 (9): 1729–36.
18. Malyarenko DI, Ross BD, Chenevert TL. Analysis and correction of gradient nonlinearity bias in ADC measurements. Magn Reson Med. 2014; 71 (3): 1312–23.
19. Lund KV, Simonsen TG, Hompland T, Kristensen GB, Rofstad EK. Short-term pretreatment DCE-MRI in prediction of outcome in locally advanced cervical cancer. Radiother Oncol. 2015; 115 (3): 379–85.
20. Campbell JL Jr, Clewell RA, Gentry PR, Andersen ME, Clewell HJ. 3rd Physiologically based pharmacokinetic/toxicokinetic modeling. 2012 Computational Toxicology, Methods in Molecular Biology Series: 439–99.

Литература

1. Bourgioti C, Chatoupis K, Moulopoulos LA. Current imaging strategies for the evaluation of uterine cervical cancer. World J Radiol. 2016; 8 (4): 342–54.
2. Jemal A, Siegel R, Ward E, Hao Y, Xu J, Murray T, et. al. Cancer statistics, 2008. CA Cancer J Clin. 2008; 58 (2): 71–96.
3. Howlader N, Noone A, Krapcho M. SEER Cancer Statistics Review, 1975–2010. 2012. Доступно по ссылке: http://seer.cancer.gov/archive/csr/1975_2010/.
4. Siegel R, Naishadham D, Jemal A. Cancer statistics, 2013. CA Cancer J Clin. 2013; 63 (1): 11–30.
5. Аксель Е. М. Статистика злокачественных новообразований женской половой сферы. Онкогинекология. 2012; (1): 18–23.
6. Давыдов М. И., Кузнецов В. В., Нечушкина М. В., редакторы. Лекции по онкогинекологии. М.: МЕДпресс-информ; 2009. 432 с.
7. Cervical Cancer Statistics [Интернет]. London: Cancer Research UK. [дата обращения: август 2016 г.]. Доступно по ссылке: http://www.cancerresearchuk.org/cancer-info/cancerstats/types/cervix/.
8. Williams NL, Werner TL, Jarboe EA, Gaffney DK. Adenocarcinoma of the cervix: should we treat it differently? Curr Oncol Rep. 2015; 17 (4): 17.
9. Тарачкова Е. В., Стрельцова О. Н., Панов В. О., Базаева И. Я., Тюрин И. Е. Мультипараметрическая магнитно-резонансная томография в диагностике рака шейки матки. Вестник рентгенологии и радиологии. 2015; (6): 43–55.
10. Труфанов Г. Е., Панов В. О., редакторы. Руководство по лучевой диагностике в гинекологии. СПб.: Элби-СПб; 2008. 592 с.
11. Kuang F, Ren J, Zhong Q, Liyuan F, Huan Y, Chen Z. The value of apparent diffusion coefficient in the assessment of cervical cancer. Eur Radiol. 2013; 23 (4): 1050–8.
12. Nakamura K, Kajitani S, Joja I, Haruma T, Fukushima C,

Kusumoto T, et al. The posttreatment mean apparent diffusion coefficient of primary tumor is superior to pretreatment ADCmean of primary tumor as a predictor of prognosis with cervical cancer. Cancer Med. 2013; 2 (4): 519–25.
13. van Vaals JJ, Brummer ME, Dixon WT, Tuithof HH, Engels H, Nelson RC, et al. Keyhole method for imaging of contrast uptake. J Magn Reson Imaging. 1993; 3 (4): 671–5.
14. Gutierrez JE, Rosenberg M, Seemann J, Breuer J, Haverstock D, et al. Safety and Efficacy of Gadobutrol for Contrast-enhanced Magnetic Resonance Imaging of the Central Nervous System: Results from a Multicenter, Double-blind, Randomized, Comparator Study. Magn Reson Insights. 2015; 8: 1–10.
15. Thomsen HS, Morcos SK, Almén T, Bellin MF, Bertolotto M, Bongartz G, et al. Nephrogenic systemic fibrosis and gadolinium-based contrast media: updated ESUR Contrast Medium Safety Committee guidelines. Eur Radiol. 2013; 23 (2):307–18.
16. Koh DM, Thoeny HC, editors. Diffusion-Weighted MR Imaging: Application in The Body. Springer-Verlag Berlin Heidelberg; 2010, p. 7–16.
17. Giannotti E, Waugh S, Priba L, Davis Z, Crowe E, Vinnicombe S. Assessment and quantification of sources of variability in breast apparent diffusion coefficient (ADC) measurements at diffusion weighted imaging, Eur J Radiol. 2015; 84 (9): 1729–36.
18. Malyarenko DI, Ross BD, Chenevert TL. Analysis and correction of gradient nonlinearity bias in ADC measurements. Magn Reson Med. 2014; 71 (3): 1312–23.
19. Lund KV, Simonsen TG, Hompland T, Kristensen GB, Rofstad EK. Short-term pretreatment DCE-MRI in prediction of outcome in locally advanced cervical cancer. Radiother Oncol. 2015; 115 (3): 379–85.
20. Campbell JL Jr, Clewell RA, Gentry PR, Andersen ME, Clewell HJ. 3rd Physiologically based pharmacokinetic/toxicokinetic modeling. 2012 Computational Toxicology, Methods in Molecular Biology Series: 439–99.

CONTRAST ENHANCED MRI OF TUMORS USING GADOPENTETIC ACID LINKED TO CYCLODEXTRIN BY AN ESTER BOND

Kulakov VN[1], Lipengolts AA[1,2], Grigorieva EYu[2], Semeikin AV[3], Abakumov MA[3], Karakhanov EA[4], Maximov AB[4], Shimanovsky NL[3] ✉

[1] Burnazyan Federal Medical Biophysical Center, Moscow, Russia

[2] N. N. Blokhin Russian Cancer Research Center, Moscow, Russia

[3] P. V. Sergeev Molecular Pharmacology and Radiobiology Department, Biomedical Faculty, Pirogov Russian National Research Medical University, Moscow, Russia

[4] Department of Petroleum Chemistry and Organic Catalysis, Faculty of Chemistry, Lomonosov Moscow State University, Moscow, Russia

Contrast-enhanced magnetic resonance imaging has become a routine diagnostic procedure. One of the most common contrast agents used for MRI is gadopentetic acid (Gd-DTPA, marketed as Magnevist). In this work, we studied the relaxivity of Gd-DTPA covalently bonded to β-cyclodextrin and compared enhancement properties of this compound and Magnevist. Our work demonstrated high relaxivity of Gd-DTPA complex containing 80 % of Gd-DTPA-modified β-cyclodextrin mono-derivative, 10 % of Gd-DTPA-modified β-cyclodextrin di-derivative and 10 % of Gd-DTPA-modified β-cyclodextrin tri-derivative. Gd-DTPA residues were linked to β-cyclodextrin by an ester bond, in which a COOH group belongs to DTPA and OH is a β-cyclodextrin surface hydroxyl group. It was proved experimentally that the studied compound is not toxic in concentrations necessary for diagnostic procedures. Compared to Magnevist, it can provide similar enhancement when used in just half of the equivalent amount.

Keywords: gadolinium, diethylenetriaminepentaacetic acid, β-cyclodextrin, tumor cells, fibroblasts, relaxivity, tumor visualization

Funding: this work was supported by Government Contract 11411.1008700.13.081 dated September 13, 2011 as part of the Federal Targeted Program for the Development of Pharmaceutical and Medical Industry of the Russian Federation until 2020.

✉ **Correspondence should be addressed:** Nikolay Shimanovsky
ul. Ostrovityanova, d. 1, Moscow, Russia, 117997; shiman@rsmu.ru

Recieved: 15.08.2016 **Accepted:** 25.08.2016

МРТ-ВИЗУАЛИЗАЦИЯ ОПУХОЛЕЙ С КОНТРАСТНЫМ УСИЛЕНИЕМ ГАДОПЕНТЕТОВОЙ КИСЛОТОЙ, СОЕДИНЕННОЙ С ЦИКЛОДЕКСТРИНОМ СЛОЖНОЭФИРНОЙ СВЯЗЬЮ

В. Н. Кулаков[1], А. А. Липенгольц[1,2], Е. Ю. Григорьева[2], А. В. Семейкин[3], М. А. Абакумов[3], Э. А. Караханов[4], А. Б. Максимов[4], Н. Л. Шимановский[3] ✉

[1] Федеральный медицинский биофизический центр имени А. И. Бурназяна, Москва

[2] Российский онкологический научный центр имени Н. Н. Блохина, Москва

[3] Кафедра молекулярной фармакологии и радиобиологии имени акад. П. В. Сергеева, медико-биологический факультет, Российский национальный исследовательский медицинский университет имени Н. И. Пирогова, Москва

[4] Кафедра химии нефти и органического катализа, химический факультет, Московский государственный университет имени М. В. Ломоносова, Москва

В настоящее время широко используют диагностическую процедуру на основе магнитно-резонансной томографии с применением контрастных средств, из которых наиболее часто применяют гадопентетовую кислоту (Gd-ДТПА, лекарственная форма — препарат «Магневист»). Данная работа посвящена изучению релаксирующей способности Gd-ДТПА, ковалентно соединенного с β-циклодекстрином, и сравнительной оценке визуализирующей способности изучаемого соединения и «Магневиста». Показано, что высокой релаксирующей способностью обладает комплекс Gd-ДТПА, состоящий из 80 % монопроизводного Gd-ДТПА-β-циклодекстрина и содержащий по 10 % ди- и три-производного Gd-ДТПА циклического углевода. Остатки Gd-ДТПА соединены с β-циклодекстрином сложноэфирной связью, где –COOH относится к ДТПА, а OH — поверхностные гидроксилы β-циклодекстрина. Экспериментально доказано, что изучаемое соединение не обладает токсичностью в диагностических концетрациях. Визуализирующая способность аналогичная «Магневисту» может быть достигнута введением меньшего, до 50 %, количества препарата.

Ключевые слова: гадолиний, диэтилентриаминопентауксусная кислота, β-циклодекстрин, опухолевые клетки, фибробласты, релаксивность, визуализация опухоли

Финансирование: работа выполнена в рамках Государственного контракта № 11411.1008700.13.081 от 13.09.2011 ФЦП «Развитие фармацевтической и медицинской промышленности Российской Федерации на период до 2020 года и дальнейшую перспективу».

✉ **Для корреспонденции:** Шимановский Николай Львович
117997, г. Москва, ул. Островитянова, д. 1; shiman@rsmu.ru

Статья получена: 15.08.2016 **Статья принята в печать:** 25.08.2016

Gadolinium enhancement is a must in cancer diagnosis assisted by magnetic resonance imaging (MRI). The most common contrast agent is gadopentetic acid (Gd-DTPA, marketed as Magnevist). Gd-DTPA-enhanced MRI is highly informative; however, it must be ordered with caution due to a risk of nephrogenic systemic fibrosis that can be induced by gadolinium release from the chelate in patients with slow Gd-DTPA clearance [1]. Therefore, finding a chelating agent with increased relaxivity (imaging capacity) remains a high priority issue, since it can facilitate switching to lower doses of the contrast agent and thus reduce the risk of nephrogenic systemic fibrosis. Cyclic hydrocarbons, such as α-, β- and γ -cyclodextrins (CDs) [2], may have good prospects here, as they are already enjoying a wide application in pharmacy as solubilizers for poorly soluble compounds and are employed in other areas of science and engineering [3].

A CD has an ability to selectively form inclusion complexes with other molecules, ions and even radicals that determines its role in basic and applied research. CDs can form complexes in solutions and in the solid phase; a good example would be CD-based chemical sensors whose mechanism of action has been well studied [4].

Gadolinium-based contrast agents are not manufactured in Russia. This fact seriously limits the scope of pathologies that could be detected on MRI (malignant tumors in the first place) and impedes treatment monitoring.

The potential of cyclodextrins in the development of gadolinium-containing contrast agents makes them an attractive research object. Cyclodextrins have good prospects due to the availability of hydroxyl groups on the molecule surface and the ability to form inclusion compounds. Numerous attempts to create gadolinium-modified cyclodextrins demonstrated that gadolinium relaxivity in such complexes significantly increases [5, 6]. However, their imaging capacity *in vivo* has not been studied yet.

The basic requirements for a CD-based complex compound are as follows: small molecule size (<5.0 nm); nontoxicity (the molecule must remain nontoxic and stable when exposed to physiological conditions for several hours); the chemical bond between a Gd^{3+}-based complex compound and a CD is expected to break inside the body; a Gd^{3+} complex must be stable at pH = 6.0–8.0.

The aim of this work was to evaluate relaxivity of Gd-DTPA linked to β-CD by an ester bond and to compare MRI scans enhanced with the experimental compounds and Magnevist.

METHODS

The following reagents were used in the experiment: reagent grade diethylenetriaminepentaacetic acid, melting point above 219 °C; β-cyclodextrin (β-CD, Aldrich, USA), purity >99 %; $Gd(NO_3)_3 \cdot 6H_2O$ (Aldrich, USA), purity of 99.99 %; reagent grade or chemically pure organic solvents. Synthesis of gadopentetic acid linked to β-CD was performed according to the patent [7]. In total, 5 samples were synthesized. Their properties are described in table 1. Magnevist (Bayer, Germany) was used as a comparator. Gadolinium concentration in the experimental formulations (aqueous solutions with pH 7.2 ± 0.2) was 0.3 M.

Gd content in the samples was measured on the X-ray fluorescence analyzer X-Art M (Comita, St.Petersburg). The weighted amount of the substance was dissolved in distilled water to a concentration of 30 mg/ml. 1 ml of the obtained solution was placed into a special cuvette. Then, 1 ml of distilled water was added to the solution, 1 ml of the obtained sample was placed in a cuvette for X-ray fluorescence analysis that was performed subsequently. 1 ml volumes were selected to ensure complete wetting of cuvette surface and measurement uniformity. Quantitative assessment of the ligand (chelator) and CD-based complex content in the synthesized samples was performed using mass spectrometry. ESI-MS spectra were registered with the Agilent LS/MS 1100 SL ion trap mass spectrometer (Agilent Technologies, USA) using electrospray ionization (ESI) in the positive/negative ion mode. The results are presented in table 1.

T_1 relaxometry was performed on the ClinScan MRI scanner by Bruker BioSpin, Germany (field strength of 7 Tesla, proton resonant frequency of 300 MHz). Tubes filled with various concentrations of the experimental compounds were placed in water for fine tuning of the magnetic field. Then, data acquisition was performed. Magnevist aqueous solution was used as a control (Magnevist concentration was identical to that of the studied compounds). Relaxation time (T_1) was calculated using Turbo Inversion Recovery sequence [8]. Signal intensity from each sample was measured using ImageJ software (National Institutes of Health, USA). T_1 values of the studied compounds were computed using the following formula:

$$SI = k \cdot (1 - (1 - \cos\alpha) \cdot e^{\frac{TI}{T_1}} - 2 \cdot \cos\alpha \cdot e^{\frac{TR - \frac{TE}{2}}{T_1}} + \cos\alpha \cdot e^{\frac{TR}{T_1}}),$$

where SI is signal intensity; T_1 is spin-lattice relaxation time; TI is inversion time; TR is repetition time; TE is echo time; α is an impulse deflection angle.

Computation was done using Mathcad software (PTC, USA). Imaging capacity of the studied samples was evaluated based on T_1 values using the ClinScan MR scanner by Bruker BioSpin, Germany (field strength of 7 Tesla, proton resonant frequency of 300 MHz) and a two-segment surface receiver coil. First, fast orthogonal T_1-weighted images (WIs) were obtained. Then, coronal fat-suppressed T_2-weighted images were obtained using Turbo Spin Echo impulse sequence (TR = 2220 ms, TE = 49 ms, section thickness of 1 mm, 16 sections, matrix of 320 × 320, FOV read = 50 mm, BLADE K-space trajectory with 100 % coverage). Axial fat-suppressed T_2-WIs were obtained using Turbo Spin Echo sequence (TR = 3310 ms, TE = 51 ms, section thickness of 1 mm, 26 sections, matrix 256 × 256, FOV read = 40 mm). Prior to MR scanning, each animal was anesthetized with 6 mg chloral hydrate diluted in normal saline. The animals fell asleep 4 to 10 minutes after the injection. Unenhanced control scans were performed in multiple positions for 20 minutes. Then, the animals received retro-orbital and intraperitoneal injections of Magnevist (the comparator) or the experimental compound in the amount of 1 mg of Gd per mouse (2×10^{-3} mmol of Magnevist, 1.5×10^{-3} mmol or K14-1). Retro-orbital route of administration was used instead of tail vein injections. Then, dynamic MRI was performed (fig. 1–4). After the experiment, the animals were sacrificed.

To assess how the experimental compound was accumulated in tumor tissues, we analyzed signal intensity in the tumor before and after 2×10^{-3} mmol of K14-1 or Magnevist had been administered. We selected a tumor region on the MR image and a similar region on the contralateral side and calculated average signal intensities (SI_c and SI_n, respectively). Average noise levels were measured in the areas outside the mouse body. For each compound, contrast-to-noise ratio (CNR) at a specific time point was calculated according to the following formula:

$$CNR = \frac{SI_c - SI_n}{SN}.$$

Table 1. T_1-relaxivity and properties of the obtained samples

Sample code	Compound	Content, %	Relaxivity, $(mmol/l)^{-1} \cdot s^{-1}$	Gd content in the sample, %
K12B-1	CD-DTPA	20	5.13	10.0
	Gd-DTPA	10		
	CD-Gd-DTPA	20		
	CD-Gd-2DTPA	10		
	CD-2(Gd-DTPA)	15		
	CD-3-2Gd-DTPA	25		
K12B-2	CD-DTPA	7	5.54	9.0
	Gd-DTPA	8		
	CD-Gd-DTPA	40		
	CD-2-Gd-DTPA	15		
	CD-2(Gd-DTPA)	15		
	CD-3-Gd-DTPA	15		
K13-1	CD-Gd-DTPA	80	5.81	12.0
	CD-3(Gd-DTPA)	20		
K13-2	CD-Gd-DTPA	60	6.29	11.8
	CD-2(Gd-DTPA)	30		
	CD-3(-Gd-DTPA)	10		
K14-1	CD-Gd-DTPA	80	6.08	12.3
	CD-2(-Gd-DTPA)	10		
	CD-3(-Gd-DTPA)	10		
Magnevist	Gd-DTPA	99	4.22	17.0
	DTPA	1		

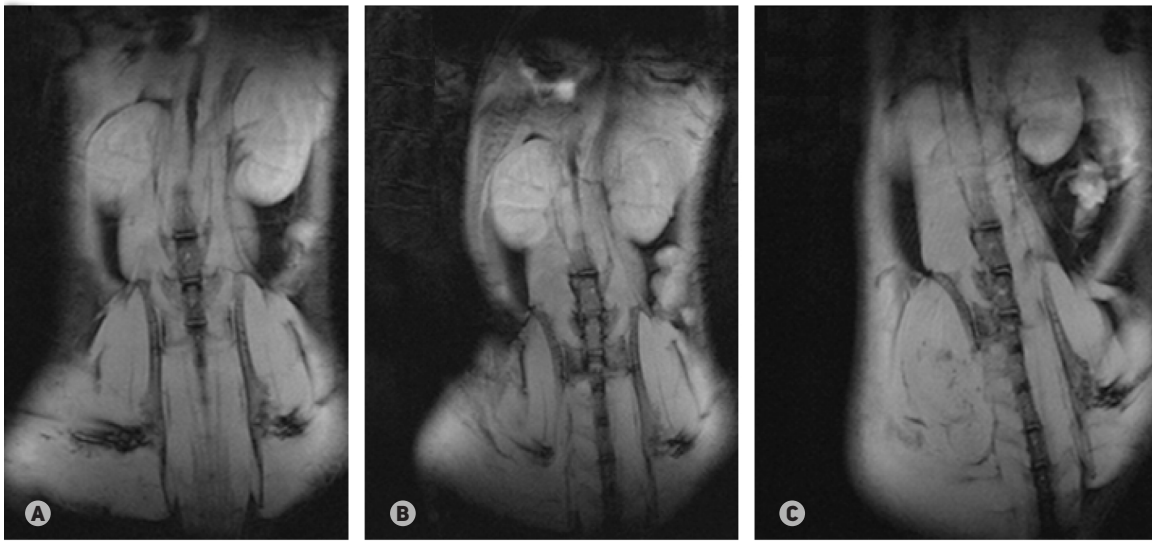

Fig. 1. MR images of mice with transplanted tumors (**A** — Ca755, **B** — LLC and **C** — B16) before contrast administration

We also compared time-dependent accumulation of gadolinium in pathological and normal tissues by computing signal-to-noise ratio (SNR) in tumor and healthy tissues at each time point:

$$SNR = \frac{SI}{SN}.$$

Figure 5 shows dependency between SNR values and time relapsed after i. v. injection of K14-1 and Magnevist in mice with transplanted melanoma.

Bio-experiments

The experiments were carried out on C57BL/6 male and female mice (weight of 18–20 g) and Wistar male and female rats (weight of 150–200 g) provided by Stolbovaya breeding nursery. All animals had a veterinary certificate (Form 1).

The experimental model complied with the guidelines for preclinical laboratory studies of novel formulations [9, 10]. For MRI-based assessment of imaging capacity of synthesized compounds, three mouse cancer cell lines from different tissue types were ordered from the Cell Bank of N. N. Blokhin Russian Cancer Research Center, namely, Lewis lung carcinoma LLC1, breast adenocarcinoma Ca755 and melanoma B16-F10. Cancer cell transplantation was performed in compliance with standard regulations [9–11]. A suspension of cancer cells (4×10^6 cells per mouse) was subcutaneously injected in the mouse thigh. The experiment went on after tumors had reached a 1 cm diameter.

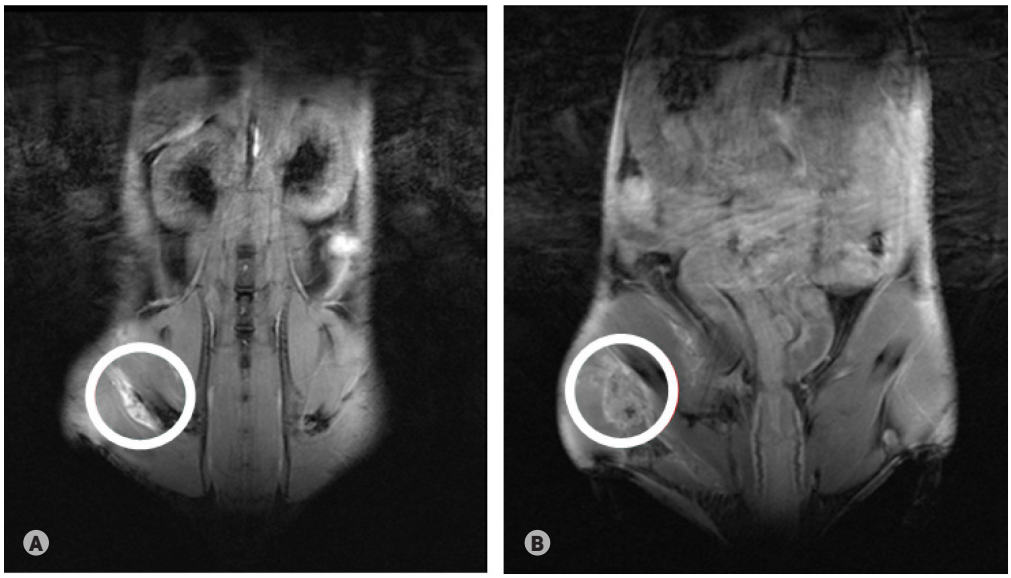

Fig. 2. MR images of mouse breast adenocarcinoma Ca755 5 minutes after injecting **(A)** Magnevist and **(B)** K14-1. The tumor area is circled

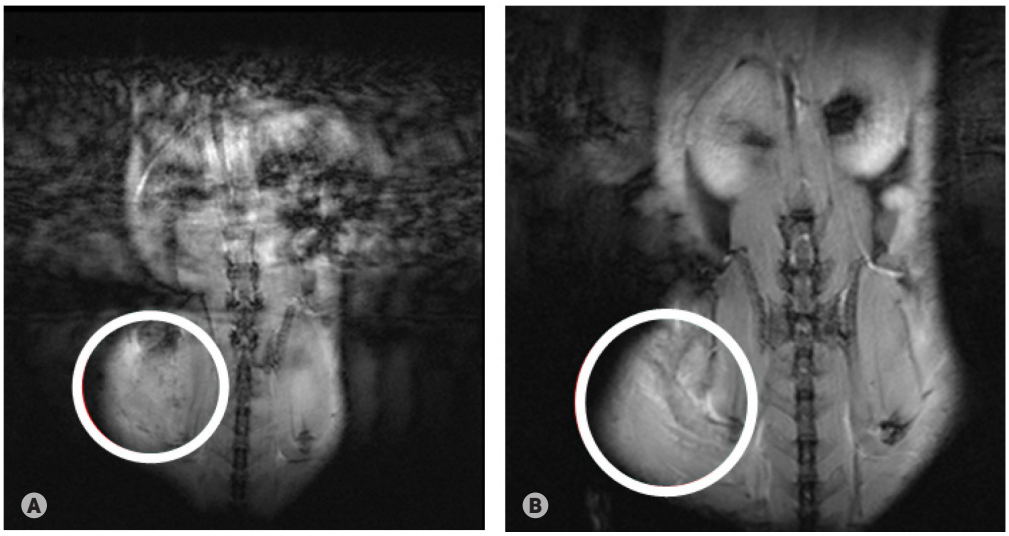

Fig. 3. MR images of mouse Lewis lung adenocarcinoma LLC 5 minutes after injecting **(A)** Magnevist and **(B)** K14-1. The tumor area is circled

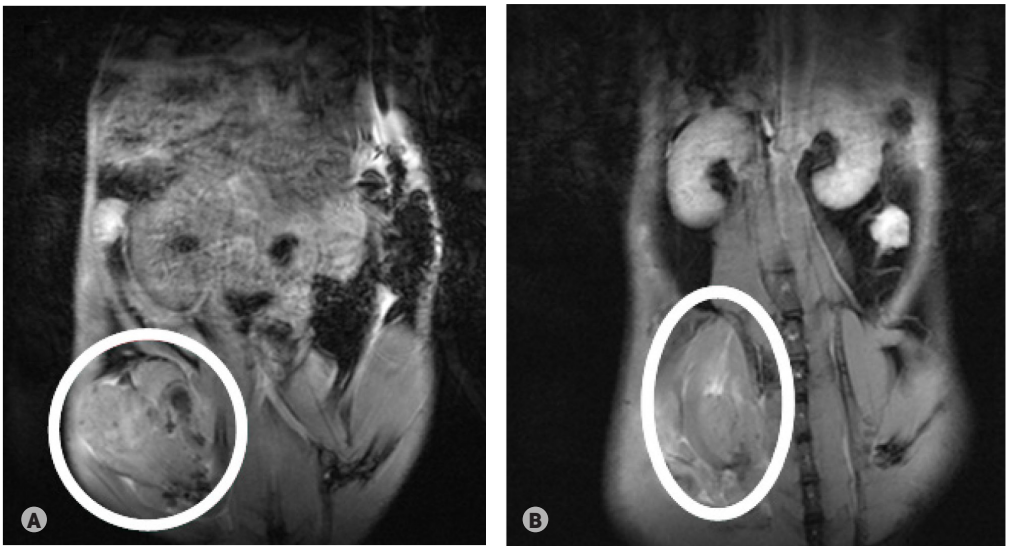

Fig. 4. MR images of mouse melanoma B16 5 minutes after injecting **(A)** Magnevist and **(B)** K14-1. The tumor area is circled

Acute toxicity tests. The animals received single intravenous doses of 3,000, 6,000, 9,000, 12,000 and 15,000 mg/kg of the studied compounds. Observation lasted for 30 days. Acute toxicity assessment was based on the number of animals found dead during the test and the day of their death [9].

Cytotoxicity of the studied compounds was assessed according to the guidelines [9] using the MTT-assay [12]. Color development was measured by detecting optical density of the sample at 530 nm wavelength using a plate photometer (AIFR-01 UNIPLAN Immunoassay Analyzer by PIKON, Russia). Percentage viability was defined as the ratio of the average optical density of the studied compound at a given concentration to the average optical density of the control sample. Data were processed using the Mann-Whitney nonparametric test. Difference was considered statistically significant with $p < 0.05$.

Fibroblast preparation. A parietal bone consists of actively proliferating cells. The bone of a neonatal rat was isolated aseptically. Briefly, after decapitation and surface sterilization, the skin was removed and the parietal bone was taken out. The parietal bone (1 cm^2 in size) was placed into a sample bottle with DMEM culture medium (PanEco, Russia) and cut into 1–2 mm3 fragments. Then, the medium with tissue fragments was placed onto the bottom of 50 ml Costar flat-bottom culture flasks by Corning, USA (bottom square area of 25 cm^2), positioned at a 45° angle and incubated for 30 minutes at 37 °C. The fragments adhered to the inclined surface. 30 minutes later, the medium was removed, the flasks were repositioned horizontally and 10 ml of DMEM were added supplemented with 20 % heat-activated fetal bovine serum, 100 μg /ml of L-glutamine and 40 μg /ml of gentamicin sulfate.

Fibroblasts were cultured under sterile conditions. The cells were incubated at 37 ºC and 5 % CO_2. All procedures were carried out in the LC laminar flow cabinet (Laminar Systems, Russia). A week later, patches of cell monolayers were observed on the flask surface. For better distribution, the cells were treated with trypsin; another week later, a multilayer culture was obtained.

Data were statistically processed using GrapthPad Prism software (GraphPad Software, USA).

RESULTS

T_1-relaxivity values of the synthesized Gd-DTPA-CD compounds and Magnevist are presented in table 1. T_1-relaxivity of all synthesized samples is higher, compared to Magnevist, but the highest relaxivity is demonstrated by K14-1, K13-1 and K13-2 samples. The β-CD compound (sample code K14-1) has a number of advantages over the comparator: its T_1-relaxivity is 50 % higher, compared to Magnevist, while gadolinium concentration in it is 40 % lower. It means that malignant tumors can be visualized using lower gadolinium doses while retaining the same quality of MR images and reducing the risk of complications.

Experiments on animals were carried out in compliance with international guidelines [13]. Intravenous injections of 3,000–6,000 mg/kg of the studied samples did not induce toxicity in rats of both genders. Death was observed in male and female rats at 9,000 mg/kg and over. The animals died no earlier than 24 hours after the injection. The animals who received sublethal doses retained normal weight during the observation. Autopsy did not detect any visual changes in the organs. Males were more sensitive to Gd-DTPA-CD than females; 2 out of 6 females and 1 out of 6 males survived after receiving 12,000 and 15,000 mg/kg of the compound. LD50 was 7 ± 1 mmol/kg.

Sample K14-1 did not exhibit significant toxicity toward rat fibroblasts at all studied concentrations (table 2).

DISCUSSION

Considering the criteria for imaging capacity required of MR contrasting agents, namely, the maximum content of Gd^{3+} paramagnetic ions and the maximum relaxivity value (table 1), we selected samples K13-1, K13-2, K14-1, K14-2 for *in vivo* assessment of the diagnostic value of MRI enhanced with these compounds. The best tumor enhancement was observed with K14-1 sample (fig. 1–4). With Magnevist and β-CD (code K14-1), enhancement quality was practically the same, although a covalently bonded Gd-DTPA — β-CD complex contains 40 % less gadolinium than Magnevist. Animals with transplanted tumors received the same amounts of gadolinium, but the β-CD derivative (code K14-1) substantially increased magnetic resonance signal in well vascularized tumors, such as breast adenocarcinoma Ca755, compared to Magnevist, which is definitely an advantage (fig. 5).

Cytotoxic effects of various concentrations of K14-1 and Magnevist were evaluated based on cell viability in the following cell cultures: Lewis lung carcinoma LLC1, melanoma B-16 and breast adenocarcinoma Ca755. With K14-1, results of all cytotoxicity tests in B16-F10, LLC1, and Ca755 cell lines

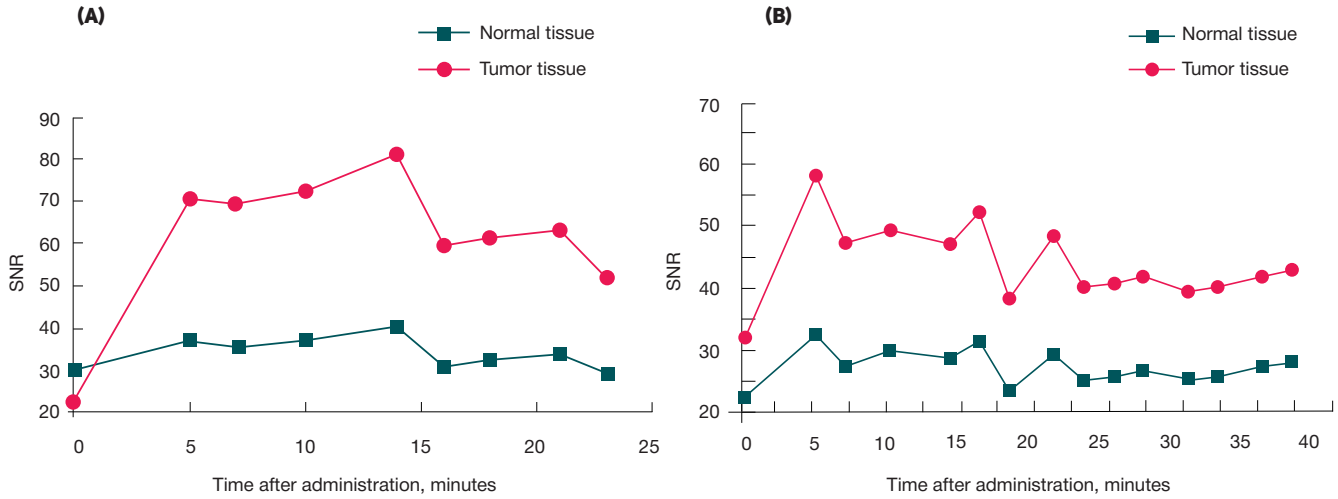

Fig. 5. The curve shows dependency between signal-to-noise ratio in normal and tumor tissues and time elapsed after the injection of the studied contrast agents (**A** — Magnevist; **B** — K14-1) in mouse melanoma B16-F10

were similar (cell growth was inhibited): $IC_{50} = (1 \div 2) \times 10^{-4}$ M; $IC_{90} = (0.2 \div 0.5) \times 10^{-4}$ M. IC_{50} computed for K14-1 fell within the range of standard cytotoxicity values suggested for active compounds ($IC_{50} \leq 10^{-4}$ M), therefore, we conclude that sample K14-1 does not exhibit conspicuous toxicity.

Biological activity of gadolinium compounds was assessed using normal fibroblasts of the rat parietal bone. These cells are highly viable and easy to culture *in vitro*. Fibroblasts are a common test object in the assessment of toxicity of various compounds [10].

Unlike Magnevist, sample K14-1 did no exhibit significant toxicity toward rat fibroblasts. Magnevist reduced cell viability by 83 and 27 % at 10 and 1 % concentrations, respectively (table 2).

Table 2. Comparison of Magnevist and β-CD derivative (sample K14-1) effect on rat fibroblast viability

K14-1 concentration, % (mM in 100 ml solution)	Cell viability, %#	
	Magnevist	K14-1
10 ($2.55 \cdot 10^{-3}$)	17*	124
1 ($2.55 \cdot 10^{-4}$)	73*	117
0.1 ($2.55 \cdot 10^{-5}$)	123	135*
0.01 ($2.55 \cdot 10^{-6}$)	127*	140*

Note: # — data are presented as percentage from the control; the control is taken as 100 %.

CONCLUSIONS

Magnevist, a contrast agent for MRI enhancement, and a modified Gd-DTPA-CD complex (sample K14-1) have relatively equal imaging capacity in mice with transplanted tumors. Sample K14-1 is original and easy to formulate; it exhibits high relaxivity and allows using 40–50 % less gadolinium for *in vivo* imaging, compared to Magnevist, thus reducing the risk of adverse effects, such as nephrogenic systemic fibrosis. Gd-DTPA-CD provides better enhancement in well vascularized tumors, compared to Magnevist.

References

1. Buylov VM. [Magnetic resonance contrast agents and nephrogenic fibrosing dermatosis and systemic fibrosis (review article)]. Medical Visualization. 2007; (2): 140–3. Russian.
2. Szejtli J. Cyclodextrin technology. Dordrecht, Netherlands: Kluwer Academic Publishers; 1988. 450 p.
3. Dodziuk H, editor. Cyclodextrins and their complexes: Chemistry, analytical methods, applications. Weinheim, Germany: Wiley-VCH; 2006. 489 p.
4. Ogoshi T, Harada A. Chemical Sensors Based on Cyclodextrin Derivatives. Sensors. 2008; 8: 4961–82.
5. Battistini E, Gianolio E, Gref R, Couvreur P, Fuzerova S, Othman M, et al. High-relaxivity magnetic resonance imaging (MRI) contrast agent based on supramolecular assembly between a gadolinium chelate, a modified dextran, and poly-beta-cyclodextrin. Chemistry. 2008; 14 (15): 4551–61.
6. Bryson JM, Chu WJ, Lee JH, Reineke TM. A β-cyclodextrin "click cluster" decorated with seven paramagnetic chelates containing two water exchange sites. Bioconjug Chem. 2008 Aug; 19 (8): 1505–9.
7. Kulakov VN, Lipengol'ts AA, Karakhanov EA, Maksimov AL, Grigor'eva EYu, Cherepanov AA, inventors. Modifitsirovannye gadopentetatom proizvodnye beta-tsiklodekstrina. Russian Federation patent No. 2541090. 2013 Nov 28. Russian.
8. Bernistein MA, King KF, Zhou XJ. Handbook of MRI pulse sequences. Burlington, MA: Elsevier Academic Press; 2004. 788 p.
9. Mironov AN, Bunatyan ND, Vasil'ev AN, Verstakova OL, Zhuravleva MV, Lepakhin VK, et al, editors. Rukovodstvo po provedeniyu doklinicheskikh issledovanii lekarstvennykh sredstv. Moscow: Grif i K; 2012. 944 p. Russian.
10. Fisenko VP, editor. Rukovodstvo po eksperimental'nomu (doklinicheskomu) izucheniyu novykh farmakologicheskikh veshchestv. Moscow: Remedium; 2000. p. 18–25. Russian.
11. Evropeiskaya konventsiya po zashchite pozvonochnykh zhivotnykh, ispol'zuemykh dlya eksperimental'nykh i drugikh nauchnykh tselei, EEC, Strasbourg, 1985. Lanimalogiya. 1993; (1): 29. Russian.
12. Mossman T. Rapid colorimetric assay for cellular growth and survival: application to proliferation and cytotoxicity assays. J Immunol Methods. 1983 Dec 16; 65 (1–2): 55–63.
13. Mezhdunarodnye rekomendatsii po provedeniyu mediko-biologicheskikh issledovanii s ispol'zovaniem zhivotnykh. WHO Chron. 1985; 39 (3): 7–9. Russian.

Литература

1. Буйлов В. М. Магнитно-резонансные контрастные средства и нефрогенные фиброзирующая дермопатия и системный фиброз (обзор литературы). Мед. визуал. 2007; (2): 140–3.
2. Szejtli J. Cyclodextrin technology. Dordrecht, Netherlands: Kluwer Academic Publishers; 1988. 450 p.
3. Dodziuk H, editor. Cyclodextrins and their complexes: Chemistry, analytical methods, applications. Weinheim, Germany: Wiley-VCH; 2006. 489 p.
4. Ogoshi T, Harada A. Chemical Sensors Based on Cyclodextrin Derivatives. Sensors. 2008; 8: 4961–82.
5. Battistini E, Gianolio E, Gref R, Couvreur P, Fuzerova S, Othman M, et al. High-relaxivity magnetic resonance imaging (MRI) contrast agent based on supramolecular assembly between a gadolinium chelate, a modified dextran, and poly-beta-cyclodextrin. Chemistry. 2008; 14 (15): 4551–61.
6. Bryson JM, Chu WJ, Lee JH, Reineke TM. A β-cyclodextrin "click cluster" decorated with seven paramagnetic chelates containing two water exchange sites. Bioconjug Chem. 2008 Aug; 19 (8): 1505–9.
7. Кулаков В. Н., Липенгольц А. А., Караханов Э. А., Максимов А. Л., Григорьева Е. Ю., Черепанов А. А. Модифицированные гадопентетатом производные бета-циклодекстрина. Патент РФ № 2541090. 28 ноября 2013 г.
8. Bernistein MA, King KF, Zhou XJ. Handbook of MRI pulse sequences. Burlington, MA: Elsevier Academic Press; 2004. 788 p.
9. Миронов А. Н., Бунатян Н. Д., Васильев А. Н., Верстакова О. Л., Журавлева М. В., Лепахин В. К. и др., редакторы. Руководство по проведению доклинических исследований лекарственных средств. М.: Гриф и К; 2012. 944 с.
10. Фисенко В. П., редактор. Руководство по экспериментальному (доклиническому) изучению новых фармакологических веществ. М.: Ремедиум; 2000. с. 18–25.
11. Европейская конвенция по защите позвоночных животных, используемых для экспериментальных и других научных целей, ЕЭС, Страсбург, 1985 г. Ланималогия. 1993; (1): 29.
12. Mossman T. Rapid colorimetric assay for cellular growth and survival: application to proliferation and cytotoxicity assays. J Immunol Methods. 1983 Dec 16; 65 (1–2): 55–63.
13. Международные рекомендации по проведению медико-биологических исследований с использованием животных. Хроника ВОЗ. 1985; 39 (3): 7–9.

NUCLEAR MEDICINE IMAGING IN DEMENTIA

Kondakov AK[1,3] ✉, Znamensky IA[1,2,3], Mosin DYu[2,3], Grechko AV[2]

[1] Department of Radiology, Biomedical Faculty,
Pirogov Russian National Research Medical University, Moscow, Russia

[2] Hospital for incurable patients – the Scientific Medical and Rehabilitation Center, Moscow, Russia

[3] Department of Radionuclide Imaging,
Central Clinical Hospital of the Russian Academy of Sciences, Moscow, Russia

In this work the authors share their opinion on the role of nuclear medicine imaging in the diagnosis and differential diagnosis of dementias. Perfusion single–photon emission computed tomography using ^{99m}Tc-exametazim and ^{18}F-fluorodeoxyglucose positron emission tomography are highly sensitive and specific; they are recommended for a wide range of clinical applications. The efficacy of amyloid imaging in Alzheimer's is still a matter of discussion, because amyloid accumulation is also typical in patients with other dementias. Dopamine transporter imaging using ^{123}I-ioflupane is a very reliable diagnostic tool for Parkinson's disease and Lewy body dementia, and can help to adjust treatment strategies. Further evolution of nuclear medicine methods will most likely include the development of new radionuclide tracers for such targets as microglial cells' activation and neurofibrillary tangles.

Keywords: nuclear medicine, SPECT, PET, exametazime, ^{18}F-fluorodeoxyglucose, Alzheimer's disease, Lewy body dementia, frontotemporal lobar degeneration, vascular dementia, dopamine transporters, amyloid imaging

✉ **Correspondence should be addressed:** Anton Kondakov
Litovsky bulvar, d. 1a, Moscow, Russia, 117593; kondakov.a.k@gmail.com

Received: 16.08.2016 **Accepted:** 21.08.2016

ВОЗМОЖНОСТИ ЯДЕРНОЙ МЕДИЦИНЫ В ДИАГНОСТИКЕ ДЕМЕНЦИЙ

А. К. Кондаков[1,3] ✉, И. А. Знаменский[1,2,3], Д. Ю. Мосин[2,3], А. В. Гречко[2]

[1] Кафедра лучевой диагностики и терапии, медико-биологический факультет,
Российский национальный исследовательский медицинский университет имени Н. И. Пирогова, Москва

[2] Госпиталь для инкурабельных больных – Научный лечебно-реабилитационный центр, Москва

[3] Отделение радионуклидных методов диагностики,
Центральная клиническая больница РАН, Москва

В работе представлено мнение о применимости различных методов ядерной медицины для диагностики, в том числе дифференциальной, различных деменций. Перфузионная однофотонная эмиссионная компьютерная томография с эксаметазимом и позитронно-эмиссионная томография с ^{18}F-фтордезоксиглюкозой высокочувствительны и высокоспецифичны и рекомендуются для широкого применения в клинической практике. Эффективность визуализации распределения амилоида при выявлении болезни Альцгеймера остается под сомнением, так как накопление амилоида характерно для пациентов с другими деменциями. Визуализация распределения переносчиков дофамина с ^{123}I-иофлупаном крайне эффективна в диагностике болезни Паркинсона и деменции с тельцами Леви: ее результаты могут обусловливать коррекцию тактики лечения. Дальнейшее развитие методов, скорее всего, будет заключаться в разработке новых радионуклидных маркеров к таким мишеням, как клетки микроглии и нейрофибриллярные клубки.

Ключевые слова: ядерная медицина, ОФЭКТ, ПЭТ, эксаметазим, ^{18}F-фтордезоксиглюкоза, болезнь Альцгеймера, деменция с тельцами Леви, фронтотемпоральная дегенерация, сосудистая деменция, переносчики дофамина, визуализация амилоида

✉ **Для корреспонденции:** Кондаков Антон Кириллович
117593, г. Москва, Литовский бульвар, д. 1а; kondakov.a.k@gmail.com

Статья поступила: 16.08.2016 **Статья принята к печати:** 21.08.2016

Improvements in life expectancy in the western world are concomitant with increasing prevalence of age-associated diseases, among which dementias amount to 1.5 %. Of all dementia cases, 70 % account for Alzheimer's disease (AD) and 2 0% are vascular dementias. In 2010 there were 35 million people living with various dementias worldwide, with the highest disease prevalence registered in Latin America [1].

Single-photon emission computed tomography (SPECT) and positron-emission tomography (PET) are nuclear medicine techniques used to diagnose dementia at early stages. Just like our colleagues from other countries, here in Russia we use a ^{99m}Tc-exametazime, a technetium-based radiopharmaceutical (RP) for SPECT imaging of regional cerebral blood flow (rCBF). For PET, ^{18}F-fluorodeoxyglucose (FDG) is used to evaluate the rate of glucose metabolism. When deciding on the nuclear medicine technique to monitor patients with neurodegenerative diseases, the doctor should bear in mind the patterns of RP distribution in the brain tissue that largely determine diagnosis accuracy and, therefore, help to elaborate a better treatment strategy. Here, we discuss the value of some radionuclide

neuroimaging techniques for the differential diagnosis of dementias and treatment monitoring and talk about further advances in this area of research.

Clinical efficacy of perfusion SPECT with ^{99m}Tc-exametazime

We believe that perfusion SPECT with ^{99m}Tc-exametazime is one of the most effective techniques used to diagnose neurodegenerative diseases. It allows diagnosing and differentiating between dementias due to various patterns of RP distribution in the brain (fig. 1) [2]. A pattern typical for frontotemporal degeneration (FTD), namely, prevailing hypoperfusion in the frontal cortex, differs significantly from the AD pattern (hypoperfusion in the parietal, prefrontal and posterior temporal cortices) [3]. SPECT is the least effective for differentiating AD from dementia with Lewy bodies (DLB), because imaging patterns of these two disorders are very similar. Dougall et al. [4] report 71.5 % sensitivity and 78.2 % specificity of SPECT when differentiating between AD and FTD; with AD and vascular dementia, the corresponding figures were 71.3 and 75.9 %. When diagnosing AD by comparing patterns of RP distribution in patients and healthy individuals, sensitivity and specificity were 66.0 and 79.0 %, respectively. Yeo et al. [5] provided slightly different statistics: pooled sensitivity and specificity of the method in the differential diagnosis of AD and FTP were 79.7 and 79.9 %, respectively; for AD and vascular dementia the figures were 70.2 and 76.2 %, respectively; when comparing patients with AD and healthy individuals, the figures were 76.1 and 85.4 %, respectively.

The potential of perfusion SPECT as a monitoring tool in the treatment of neurodegenerative disorders has not been studied properly. Efimova et al. [6] demonstrated that brain perfusion and cognitive function improve in the course of antihypertensive therapy by comparing screening results before treatment and six months after it. Murashko [7] studied brain perfusion in patients with hypertonic encephalopathy and demonstrated that therapy with cavinton improved brain perfusion. However, the study sample was too small, and there was no control group. Another important observation was made by Nobili et al. [8], who performed repeat brain perfusion SPECT scans on patients with AD after starting therapy with acetylcholinesterase inhibitors. They showed that if cognitive function was intact, brain perfusion pattern did not change significantly, while in patients with deteriorated cognitive function, who were undergoing treatment, rCBF was reduced. We believe that perfusion SPECT can be a promising tool in the assessment of medication efficacy and prediction of the disease outcome. However, this method still requires further longitudinal studies.

In Russia, perfusion SPECT is not included into the state-approved standard of medical care. Besides, it is quite expensive, therefore, is not used widely. We think that professional medical community should call for the inclusion of this method into the standard of the specialized medical care for patients with Alzheimer's disease and other dementias, given that the equipment necessary for scanning procedures is available in most regional centers.

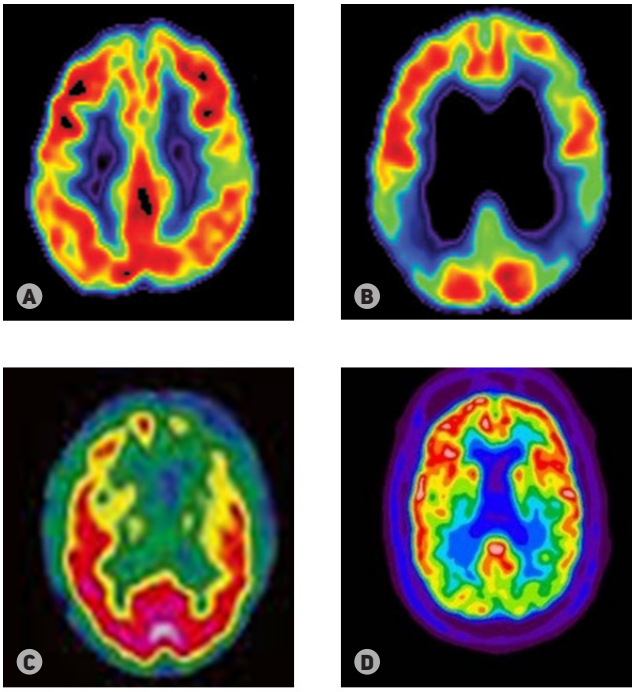

Fig. 1. Brain perfusion SPECT with 99mTc-exametazime, axial sections. **(A)** Intact brain perfusion. **(B)** Perfusion pattern typical for Alzheimer's disease (reduced perfusion in the parietal cortex). **(C)** Perfusion pattern typical for frontotemporal degeneration (reduced perfusion in the frontal cortex). **(D)** Perfusion pattern typical for Lewy body dementia and similar to Alzheimer's; reduced perfusion is observed in the occipital cortex (Dierckx et al. [2])

Clinical efficacy of PET with ^{18}F-fluorodeoxyglucose

We believe that PET with ^{18}F- fluorodeoxyglucose can be used for diagnosing neurodegenerative diseases in the same cases as perfusion SPECT, because patterns of glucose hypometabolism and hypoperfusion are similar: glucose utilization and brain regional perfusion are linked [9]. Both hypoperfusion regions detected by perfusion SPECT with ^{99m}Tc-exametazime and hypometabolism regions found on PET with ^{18}F-FDG reflect structural changes in the brain [10]. PET has a better resolution and ^{18}F-FDG is a more stable radionuclide tracer than ^{99m}Tc-exametazime, which makes this method highly accurate. Davison et al. [11] compared PET with 18F-FDG and perfusion SPECT with ^{99m}Tc-exametazime and found that SPECT sensitivity and specificity were 85.0 and 87.0 %, respectively, while PET sensitivity and specificity were 99.0 and 93.0 %, respectively. However, the authors note that the number of works confirming their findings is low and emphasize the necessity of direct prospective comparative studies in this area of research.

We would like to draw the reader's attention to the work by Kato et al. [12] in which reduced perfusion in inferior parietal lobe, precuneus and posterior cingulate gyrus is described as a predictor of mild cognitive impairment evolution into Alzheimer's disease, in addition to the already known patterns of reduced glucose uptake.

We believe that PET scanning should be used to differentiate between dementias only when other methods have failed and under the condition that scan results will influence the treatment strategy. Specifically, PET with ^{18}F-FDG can be used to support AD diagnosis based on the results of neuropsychological testing, if CT or MRI showed no changes in the brain matter and SPECT findings are ambiguous.

PET in amyloid imaging

For brain amyloid imaging, ^{11}C-Pittsburgh compound B is used. Its clinical application was first described in 2004 [13]. Due to the short half-life of ^{11}C, ^{18}F-based RPs were developed,

including florbetapir, florbetaben and flutemetamol (all approved by American Food and Drug Administration).

We believe that clinical importance of scanning that makes use of RPs exhibiting affinity to amyloids is questionable. This method is very cost-ineffective and can not be included into standard screening procedures. We do not recommend it for the differential diagnosis of dementias, as amyloid plaques can be visualized in patients who do not have AD or suffer from other dementias. In about 20 % of cases, amyloid accumulation is observed in patients with clinically verified FTD, which can be explained by the similarity of AD and FTD symptoms or by concomitant AD and FTD pathologies [14]. About 89 % of patients with DLB accumulate RPs with affinity to amyloids. Still, it is not a false positive result, but rather a reflection of a pathophysiological process [2].

We do not recommend amyloid imaging for the assessment of dementia severity and therapy progress, because amyloid deposition is markedly slowed after the onset of mild cognitive impairments. From that moment, amyloid imaging becomes ineffective, as amyloid accumulation surrenders its leading role in cognitive function deterioration to the structural changes in the brain. Perfusion SPECT or PET with ^{18}F-FDG describe the course of the disease better.

Dopamine transporter imaging

The reduced number of dopamine transporters in the putamen is a hallmark of Parkinson's disease and Lewy body dementia. Visualization of dopamine transporter distribution in patients is performed using ^{123}I-ioflupan. It has a high affinity to dopamine transporters and binds to them in the striate bodies. SPECT scanning can evaluate their number reduction (fig. 2) [15].

This method can be recommended for clinical use, as it is a highly effective diagnostic tool: with DLB, its sensitivity is over 70.0 % and specificity is over 90.0 % [16]. We believe that scan results can be a basis for the adjustments in the treatment plan. A randomized study conducted by Walker et al. [17] confirmed that if the scan result is positive (suggesting DLB), doctors make necessary corrections to the diagnosis and treatment strategy. Wide clinical application of this method is restricted by ^{123}I-ioflupan high price.

CONCLUSIONS

Radionuclide techniques are effective ancillary tools in the diagnosis and differential diagnosis of dementias, especially at early stages of the disease when morphological changes in the brain have not yet set in. Available in Russia, perfusion SPECT and PET are highly sensitive and specific. They are also very effective as a monitoring tool for assessing the progress of the neurodegenerative disease when combined with longitudinal studies, but their application is restricted by a high price of radionuclide tracers.

We believe that dopamine transporter imaging is highly effective and can be used to diagnose Lewy body dementia and parkinsonian syndromes along with the development of novel RPs. At the same time, amyloid imaging is the least effective in the differential diagnosis of various dementias due to the high cost of RPs and difficult interpretation of the results. We recommend this scanning procedure should be introduced in a few federal medical centers for studying complicated cases of dementias at early stages and conducting scientific research; new radionuclide tracers should be developed in cyclotron radiochemistry labs in parallel.

Further evolution of nuclear medicine techniques for the diagnosis of neurodegenerative diseases will depend on the development of more specific radionuclide tracers, including those that detect microglial cells activation (^{11}C-PK11195) [18]. Another potential target for diagnostic imaging in patients with dementias is neurofibrillary tangles. At the moment, new RPs are being developed for their targeting. However, one of such radionuclide tracers, ^{18}F-FDDNP, is still less effective than Pittsburgh compound B and ^{18}F-FDG in predicting the disease progress [19].

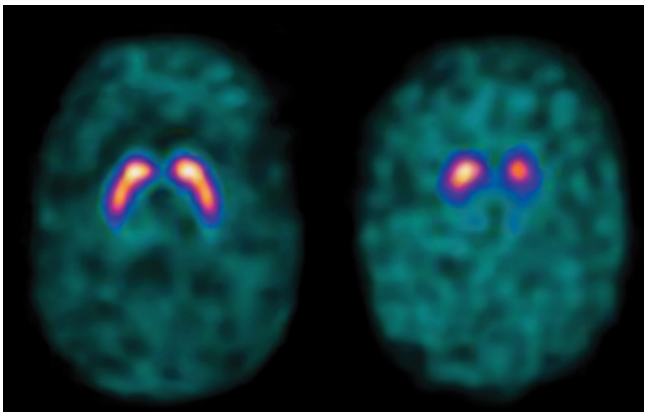

Fig. 2. SPECT with 123I-ioflupan shows distribution of dopamine transporters. The picture shows axial sections at the striatal level. Left: a section obtained from a healthy volunteer. Right: a section obtained from a patient with Parkinson's disease (Hauser et al. [15])

References

1. Prince M, Bryce R, Albanese E, Wimo A, Ribeiro W, Ferri CP. The global prevalence of dementia: A systematic review and metaanalysis. Alzheimers Dement. 2013 Jan; 9 (1): 63–75.e2. doi: 10.1016/j.jalz.2012.11.007.
2. Dierckx RAJO, Otte A, de Vries EFJ, van Waarde A, Leenders KL, editors. PET and SPECT in Neurology. Berlin, Heidelberg: Springer-Verlag; 2014.
3. Trollor JN, Sachdev PS, Haindl W, Brodaty H, Wen W, Walker BM. Regional cerebral blood flow deficits in mild Alzheimer's disease using high resolution single photon emission computerized tomography. Psychiatry Clin Neurosci. 2005 Jun; 59 (3): 280–90. doi: 10.1111/j.1440-1819.2005.01372.x.
4. Dougall NJ, Bruggink S, Ebmeier KP. Systematic review of the diagnostic accuracy of 99mTc-HMPAO-SPECT in dementia. Am J Geriatr Psychiatry. 2004 Nov–Dec; 12 (6): 554–70. doi: 10.1176/appi.ajgp.12.6.554.
5. Yeo JM, Lim X, Khan Z, Pal S. Systematic review of the diagnostic utility of SPECT imaging in dementia. Eur Arch Psychiatry Clin Neurosci. 2013 Oct; 263 (7): 539–52. doi: 10.1007/s00406-013-0426-z.
6. Efimova NYu, Chernov VI, Efimova IYu, Shnaider OL, Popov SV. Vliyanie implantatsii elektrokardiostimulyatora na kognitivnuyu disfunktsiyu u patsientov s postoyannoi formoi fibrillyatsii predserdii: vzaimosvyaz' s tserebral'noi perfuziei. Vestnik aritmologii. 2008; (54): 15–9. Russian.
7. Murashko NK. Odnofotonnaya emissionnaya tomografiya pri khronicheskoi gipertonicheskoi entsefalopatii. Klinicheskaya gerontologiya. 2007; (8): 26–9. Russian.
8. Nobili F, Koulibaly M, Vitali P, Migneco O, Mariani G, Ebmeier K, et al. Brain perfusion follow-up in Alzheimer's patients during

treatment with acetylcholinesterase inhibitors. J Nucl Med. 2002 Aug; 43 (8): 983–90.
9. Rocher AB, Chapon F, Blaizot X, Baron JC, Chavoix C. Resting-state brain glucose utilization as measured by PET is directly related to regional synaptophysin levels: a study in baboons. Neuroimage. 2003 Nov; 20 (3): 1894–8.
10. Ahmed RM, Paterson RW, Warren JD, Zetterberg H, O'Brien JT, Fox NC, et al. Biomarkers in dementia: clinical utility and new directions. J Neurol Neurosurg Psychiatry. 2014 Dec; 85 (12): 1426–34. doi: 10.1136/jnnp-2014-307662.
11. Davison CM, O'Brien JT. A comparison of FDG-PET and blood flow SPECT in the diagnosis of neurodegenerative dementias: A systematic review. Int J Geriatr Psychiatry. 2014 Jun; 29 (6): 551–61. doi: 10.1002/gps.4036.
12. Kato T, Inui Y, Nakamura A, Ito K. Brain fluorodeoxyglucose (FDG) PET in dementia. Ageing Res Rev. 2016 Feb 11. doi: 10.1016/j.arr.2016.02.003. [Epub ahead of print].
13. Klunk WE, Engler H, Nordberg A, Wang Y, Blomqvist G, Holt DP, et al. Imaging brain amyloid in Alzheimer's disease with Pittsburgh Compound-B. Ann Neurol. 2004 Mar; 55 (3): 306–19. doi: 10.1002/ana.20009.
14. Villemagne VL. Amyloid imaging: Past, present and future perspectives. Ageing Res Rev. 2016 Jan 28. doi: 10.1016/j.arr.2016.01.005. [Epub ahead of print].
15. Hauser RA, Grosset DG. [123I]FP-CIT (DaTscan) SPECT brain imaging in patients with suspected parkinsonian syndromes. J Neuroimaging. 2012 Jul; 22 (3): 225–30. doi: 10.1111/j.1552-6569.2011.00583.x.
16. Baglio F, Preti MG, Farina E. Neuroimaging Findings in Dementia with Lewy Body: A Review. In: Bright P, editor. Neuroimaging — Methods. InTech; 2012. doi: 10.5772/24221. Available from: http://www.intechopen.com/books/neuroimaging-methods/neuroimaging-findings-in-dementia-with-lewy-body-a-review-
17. Walker Z, Moreno E, Thomas A, Inglis F, Tabet N, Rainer M, et al. Clinical usefulness of dopamine transporter SPECT imaging with 123I-FP-CIT in patients with possible dementia with Lewy bodies: randomised study. Br J Psychiatry. 2015 Feb; 206 (2): 145–52. doi: 10.1192/bjp.bp.114.148643.
18. Okello A, Edison P, Archer HA, Turkheimer FE, Kennedy J, Bullock R, et al. Microglial activation and amyloid deposition in mild cognitive impairment: a PET study. Neurology. 2009 Jan 6; 72 (1): 56–62. doi: 10.1212/01.wnl.0000338622.27876.0d.
19. Ossenkoppele R, Tolboom N, Foster-Dingley JC, Adriaanse SF, Boellaard R, Yaqub M, et al. Longitudinal imaging of Alzheimer pathology using [11C]PIB, [18F]FDDNP and [18F]FDG PET. Eur J Nucl Med Mol Imaging. 2012 Jun; 39 (6): 990–1000. doi: 10.1007/s00259-012-2102-3.

Литература

1. Prince M, Bryce R, Albanese E, Wimo A, Ribeiro W, Ferri CP. The global prevalence of dementia: A systematic review and metaanalysis. Alzheimers Dement. 2013 Jan; 9 (1): 63–75.e2. doi: 10.1016/j.jalz.2012.11.007.
2. Dierckx RAJO, Otte A, de Vries EFJ, van Waarde A, Leenders KL, editors. PET and SPECT in Neurology. Berlin, Heidelberg: Springer-Verlag; 2014.
3. Trollor JN, Sachdev PS, Haindl W, Brodaty H, Wen W, Walker BM. Regional cerebral blood flow deficits in mild Alzheimer's disease using high resolution single photon emission computerized tomography. Psychiatry Clin Neurosci. 2005 Jun; 59 (3): 280–90. doi: 10.1111/j.1440-1819.2005.01372.x.
4. Dougall NJ, Bruggink S, Ebmeier KP. Systematic review of the diagnostic accuracy of 99mTc-HMPAO-SPECT in dementia. Am J Geriatr Psychiatry. 2004 Nov–Dec; 12 (6): 554–70. doi: 10.1176/appi.ajgp.12.6.554.
5. Yeo JM, Lim X, Khan Z, Pal S. Systematic review of the diagnostic utility of SPECT imaging in dementia. Eur Arch Psychiatry Clin Neurosci. 2013 Oct; 263 (7): 539–52. doi: 10.1007/s00406-013-0426-z.
6. Ефимова Н. Ю., Чернов В. И., Ефимова И. Ю., Шнайдер О. Л., Попов С. В. Влияние имплантации электрокардиостимулятора на когнитивную дисфункцию у пациентов с постоянной формой фибрилляции предсердий: взаимосвязь с церебральной перфузией. Вестн. аритмол. 2008; (54): 15–9.
7. Мурашко Н. К. Однофотонная эмиссионная томография при хронической гипертонической энцефалопатии. Клин. геронтол. 2007; (8): 26–9.
8. Nobili F, Koulibaly M, Vitali P, Migneco O, Mariani G, Ebmeier K, et al. Brain perfusion follow-up in Alzheimer's patients during treatment with acetylcholinesterase inhibitors. J Nucl Med. 2002 Aug; 43 (8): 983–90.
9. Rocher AB, Chapon F, Blaizot X, Baron JC, Chavoix C. Resting-state brain glucose utilization as measured by PET is directly related to regional synaptophysin levels: a study in baboons. Neuroimage. 2003 Nov; 20 (3): 1894–8.
10. Ahmed RM, Paterson RW, Warren JD, Zetterberg H, O'Brien JT, Fox NC, et al. Biomarkers in dementia: clinical utility and new directions. J Neurol Neurosurg Psychiatry. 2014 Dec; 85 (12): 1426–34. doi: 10.1136/jnnp-2014-307662.
11. Davison CM, O'Brien JT. A comparison of FDG-PET and blood flow SPECT in the diagnosis of neurodegenerative dementias: A systematic review. Int J Geriatr Psychiatry. 2014 Jun; 29 (6): 551–61. doi: 10.1002/gps.4036.
12. Kato T, Inui Y, Nakamura A, Ito K. Brain fluorodeoxyglucose (FDG) PET in dementia. Ageing Res Rev. 2016 Feb 11. doi: 10.1016/j.arr.2016.02.003. [Epub ahead of print].
13. Klunk WE, Engler H, Nordberg A, Wang Y, Blomqvist G, Holt DP, et al. Imaging brain amyloid in Alzheimer's disease with Pittsburgh Compound-B. Ann Neurol. 2004 Mar; 55 (3): 306–19. doi: 10.1002/ana.20009.
14. Villemagne VL. Amyloid imaging: Past, present and future perspectives. Ageing Res Rev. 2016 Jan 28. doi: 10.1016/j.arr.2016.01.005. [Epub ahead of print].
15. Hauser RA, Grosset DG. [123I]FP-CIT (DaTscan) SPECT brain imaging in patients with suspected parkinsonian syndromes. J Neuroimaging. 2012 Jul; 22 (3): 225–30. doi: 10.1111/j.1552-6569.2011.00583.x.
16. Baglio F, Preti MG, Farina E. Neuroimaging Findings in Dementia with Lewy Body: A Review. In: Bright P, editor. Neuroimaging — Methods. InTech; 2012. doi: 10.5772/24221. Available from: http://www.intechopen.com/books/neuroimaging-methods/neuroimaging-findings-in-dementia-with-lewy-body-a-review-
17. Walker Z, Moreno E, Thomas A, Inglis F, Tabet N, Rainer M, et al. Clinical usefulness of dopamine transporter SPECT imaging with 123I-FP-CIT in patients with possible dementia with Lewy bodies: randomised study. Br J Psychiatry. 2015 Feb; 206 (2): 145–52. doi: 10.1192/bjp.bp.114.148643.
18. Okello A, Edison P, Archer HA, Turkheimer FE, Kennedy J, Bullock R, et al. Microglial activation and amyloid deposition in mild cognitive impairment: a PET study. Neurology. 2009 Jan 6; 72 (1): 56–62. doi: 10.1212/01.wnl.0000338622.27876.0d.
19. Ossenkoppele R, Tolboom N, Foster-Dingley JC, Adriaanse SF, Boellaard R, Yaqub M, et al. Longitudinal imaging of Alzheimer pathology using [11C]PIB, [18F]FDDNP and [18F]FDG PET. Eur J Nucl Med Mol Imaging. 2012 Jun; 39 (6): 990–1000. doi: 10.1007/s00259-012-2102-3.

POSTMORTEM MAGNETIC RESONANCE IMAGING IN THE DIAGNOSIS OF CONGENITAL PNEUMONIA

Tumanova UN[1]✉, Lyapin VM[1], Bychenko VG[1], Schegolev AI[1,2], Sukhikh GT[1]

[1] Kulakov Research Center for Obstetrics, Gynecology and Perinatology, Moscow, Russia

[2] Pirogov Russian National Research Medical University, Moscow, Russia

Congenital pneumonia is one of the leading causes of neonatal deaths. In this work we assess the possibility of using postmortem magnetic resonance imaging for the diagnosis of congenital pneumonia. The study was conducted on 21 neonate bodies. Before the autopsy, MRI scanning was performed on the Magnetom Verio 3T system (Siemens, Germany) in T1 and T2 standard modes. The resulting images were used to analyze signal intensities of lung tissue, pleural fluid and air. Airiness index was computed as the ratio of pleural fluid signal intensity to lung tissue signal intensity. Then, the autopsy was performed. Based on the histological analysis results, the main and the control groups were formed. The bodies of 9 neonates who had died from congenital pneumonia were included into the main group; the control group consisted of 12 dead neonates with no signs of pneumonia. On T1-weighted images, the signal intensity from the lungs of the infants with congenital pneumonia was higher by 26.5 % in the left lung and 12.9 % in the right lung, compared to the controls (p >0.05). On T2-weighted images, the corresponding figures were 23.7 and 31.2 % (p >0.05). The sensitivity of the method is 77.8 %, specificity is 75.0 % and diagnostic efficacy is 76.2 %.

Keywords: congenital pneumonia, lung, postmortem magnetic resonance imaging, autopsy, airiness index

✉ **Correspondence should be addressed:** Uliana Tumanova
ul. Akademika Oparina, d. 4, Moscow, Russia, 117997; u.n.tumanova@gmail.com

Received: 17.08.2016 **Accepted:** 23.08.2016

ПОСМЕРТНАЯ МРТ ДЛЯ ДИАГНОСТИКИ ВРОЖДЕННОЙ ПНЕВМОНИИ

У. Н. Туманова[1]✉, В. М. Ляпин[1], В. Г. Быченко[1], А. И. Щеголев[1,2], Г. Т. Сухих[1]

[1] Научный центр акушерства, гинекологии и перинатологии имени академика В. И. Кулакова, Москва

[2] Российский национальный исследовательский медицинский университет имени Н. И. Пирогова, Москва

Врожденная пневмония — одна из основных причин гибели детей в неонатальном периоде. В работе оценена возможность применения посмертной магнитно-резонансной томографии для диагностики врожденной пневмонии на аутопсийном материале. Исследовали тела 21 умершего новорожденного. До аутопсии проводили МРТ-исследование на аппарате 3T Magnetom Verio (Siemens, Германия) в стандартных T1 и T2 режимах. На томограммах анализировали интенсивность сигнала от ткани легких, плевральной жидкости и воздуха и рассчитывали показатель воздушности — отношение интенсивности сигнала от жидкости в плевральной полости к интенсивности сигнала от ткани легких. Затем проводили патологоанатомическое вскрытие и по результатам изучения гистологических препаратов все наблюдения разделили на две группы: в основную группу включили тела 9 новорожденных, умерших от врожденной пневмонии, в группу сравнения — тела 12 умерших новорожденных без признаков пневмонии. Интенсивность сигнала от ткани легких новорожденных с врожденной пневмонией была выше аналогичного показателя в группе сравнения: на 26,5 и 12,9 % в левом и правом легком соответственно на T1-взвешенных изображениях (p >0,05) и на 23,7 и 31,2 % — на T2-взвешенных изображениях (p >0,05). Чувствительность описанного метода составила 77,8 %, специфичность — 75,0 %, диагностическая эффективность — 76,2 %.

Ключевые слова: врожденная пневмония, легкое, посмертная магнитно-резонансная томография, аутопсия, показатель воздушности

✉ **Для корреспонденции:** Туманова Ульяна Николаевна
117997, г. Москва, ул. Академика Опарина, д. 4; u.n.tumanova@gmail.com

Статья поступила: 17.08.2016 **Статья принята к печати:** 23.08.2016

Congenital pneumonia is an acute inflammatory condition of the respiratory zone caused by an antenatal or/and intrapartum infection and manifesting itself clinically and radiographically within the first 72 hours after birth [1]. Improvements in diagnostic techniques and treatment approaches contribute to better survival of affected neonates, but death rate still remains relatively high. According to research data [2], congenital pneumonia is diagnosed worldwide in 10–38 % of stillborn and 20–63 % of liveborn babies who subsequently die. In Russia, congenital pneumonia accounted for 0.43 % of all intrauterine deaths and was also the primary cause of death of 8.7 % of infants in the early (0–6 days) neonatal period in 2010, as reported by the Federal Service for State Statistics [3]. In 2014, those figures were 0.35 % and 8.34 %, respectively [4].

The major technique for the postmortem diagnosis of congenital pneumonia is autopsy. However, morphological analysis is often impeded by false positive results of lung float test performed at autopsy and by a weak inflammatory response in premature babies or upon treatment with antibiotics [5, 6]. Here, radiography is usually an alternative.

Computed tomography (CT) is considered the major radiographic technique used to diagnose pulmonary pathologies [7–9]. Postmortem CT is also quite effective in the assessment of lung conditions and determining cause of death in adults [10]. However, lungs of dead fetuses and neonates are not visible on unenhanced CT [11]. Parallel to CT, magnetic resonance imaging (MRI) is being increasingly used to detect pulmonary pathologies [12]. For example, bronchial pneumonia previously diagnosed during a CT scan was detected later by MRI in 21 out of 22 adults, and the efficacy of this technique was relatively high: sensitivity of 95 %, specificity of 88 %, positive prognostic value of 95 % [13]. MRI proved to be an effective diagnostic tool in the examination of 30 children (3–19 years of age) who had already been diagnosed with pneumonia based on the X-ray test [14]. The researchers concluded that MRI could be used as an alternative to X-ray or CT for the detection of pneumonia foci no smaller than 1 cm in size in the absence of calcification [13, 14]. Since MRI produces images in any projection and the patient is not exposed to radiation, it can be recommended for the dynamic assessment of pneumonia progression. Leutner et al. [15] demonstrated that MRI is more effective in diagnosing necrotizing pneumonia, compared to enhanced CT. MRI also proved highly effective in the differential diagnosis of causes of stillbirths and neonatal deaths [16, 17] and was successfully used to determine time of intrauterine fetal death by evaluating lung morphology [18, 19].

The aim of this work was to study a possibility of using postmortem MRI for diagnosing congenital pneumonia in autopsy material.

METHODS

We studied 21 dead neonates. Six to fifteen hours after infants had been pronounced dead but prior to autopsy, the bodies were scanned in standard T1 and T2 modes on 3T Magnetom Verio scanner (Siemens, Germany) set up to a field of view of 300 mm and a flip angle of 180°. T1-mode settings were as follows: slice thickness of 0.9 mm, repetition time of 1, 900 ms, echo time of 2.2 ms. T2-mode settings were as follows: slice thickness of 1 mm, repetition time of 3,200 ms, echo time of 410 ms. Using sagittal T1- and T2-weighted images, we measured signal intensity (SI) in the following regions of interest (ROI): the largest possible section of the right and left lung that did not contain big elements of the bronchovascular bundle, region of air in the area close to the anterior abdominal wall and in the pleural fluid. Then, an original airiness index (AI) was calculated for the right and left lungs as the ratio of the SI value of the pleural fluid to the SI value of the lung tissue. Because MR signal intensity within a given body region changes non-linearly and depends on a number of factors (distance from the scanner's isocenter, magnetic field homogeneity, physical properties of the surrounding tissues, etc.), to study its absolute value alone would be incorrect. We believe that airiness index allows minimizing or even eliminating measurement error related to the performance of an individual scanner.

After MRI scan, autopsy was performed followed by the analysis of hematoxylin- and eosin-stained histological slices. Based on the autopsy results, two groups were formed: group (the main experimental group) included bodies of 9 neonates who had died of congenital pneumonia 2 h 12 min to 36.5 days after birth; group II (the comparison group) included bodies of 12 neonates with no signs of pneumonia who had died 2 h 7 min to 24 days after birth. The bodies, the right lung and the left lung were weighted. The weight ratio of both lungs to the body was calculated.

Statistical processing was done using Statistica 8.0 software (StatSoft, USA). Mean values, standard deviations and a coefficient of variation were computed for each measured parameter. Differences were considered significant with $p < 0.05$. Using the obtained results, we calculated sensitivity, specificity and diagnostic efficacy of postmortem MRI in the diagnosis of congenital pneumonia.

The study was approved by the Biomedical Research Ethics Committee of Kulakov Research Center for Obstetrics, Gynecology and Perinatology (Protocol 25 dated June 22, 2012).

RESULTS

Morphological analysis of autopsy material obtained from the comparison group established that left lung weight varied from 2.1 to 36.5 g (coefficient of variation was 95.4 %) and right lung weight varied from 0.3 to 24.2 g (coefficient of variation was 50.9 %) (table 1). Mean weight of the left, right and both lungs was 10.8 ± 10.8, 11.5 ± 6.1 and 22.3 ± 14.6 g, respectively. Histological samples of lung tissue had signs of hypoplasia (in bodies with congenital diaphragmatic hernia) (fig. 1A), atelectases and dystelectases.

In neonates who had died of pneumonia, the weights of the left and right lungs were 4.1 to 42.7 g (coefficient of variation was 44.9 and 40.1 %, respectively) (table 1). Mean weights were 19.6 ± 9.3 and 24.1 ± 10.2 g, respectively; mean weight of both lungs was 45.9 ± 17.7 g. This indicates that all values were 1.8–2.1 times higher than in the comparison group ($p < 0.05$). The weight ratio of both lungs to the body was 2.4 times higher in the experimental group ($p < 0.05$). Histological samples obtained from group I showed signs of pneumonia manifested as weak monocyte/macrophage infiltration. (fig. 1B).

Visual analysis of T1- and T2-weighted images obtained from both groups indicated almost identical signal intensity in both lungs, but T2-weighted images reflected the organ structure more clearly, compared to T1-weighted images (fig.2, 3). The signal from the lungs of neonates who had died of pneumonia was more intense in both scanning modes as compared to the signal from the lungs of neonates who had died of other pathologies. It was 26.5 and 12.9 % more intense for the left and right lungs, respectively, on T1-weighted images and 23.7 and 31.2 % more intense on T2-weighted images ($p > 0.05$) (table 2). Nonuniform signal intensity within one lung was occasionally observed in the comparison group as a result of a haemorrhage (fig.4); differences in tissue brightness in the right and left lungs were due to organ compression caused by diaphragmatic hernia (fig. 5).

Mean airiness index of the left lung calculated upon the analysis of T1-weighted images of neonates who had died of pneumonia was by 44 % lower in the experimental group than in the comparison group; with the right lung, it was by 1.1 % higher (table 2). The same index calculated upon the analysis of T2-weighted images was lower for both lungs in the experimental group: by 14.3 % for the left lung and by 5.7 % for the right lung. When airiness index was calculated in the right and left lung separately, differences were statistically insignificant ($p > 0.05$). However, if the index value obtained from T2-weighted images was less than 2.5 in both lungs of a newborn, it indicated a morphologically confirmed pneumonia in the vast majority of cases (77.8 %).

Sensitivity of the applied technique was 77.8 %, its specificity was 75.0 % and diagnostic efficacy was 76.2 %, which indicates its high diagnostic value.

Table 1. Clinical and morphological features of dead neonates

Group	Case	Sex	Gestational age	Age	Body weight	Weight of both lungs	Right lung weight	Left lung weight	Weight ratio of both lungs to the body
I	1	F	38	5 сут. 11 ч	2080.0	43.2	22.1	21.1	0.021
	2	M	33	28 сут.	2800.0	58.6	25.2	33.4	0.021
	3	м	24	5 сут. 15 ч	800.0	16.3	12.2	14.1	0.020
	4	F	33	7 сут. 14 ч	2674.0	52.6	29.3	23.3	0.020
	5	M	35	36 сут. 10 ч	3206.0	43.9	23.3	20.6	0.014
	6	M	39	3 сут. 4 ч	3980.0	65.3	42.7	22.6	0.016
	7	M	30	5 сут.	1942.0	62.7	33.7	29.0	0.032
	8	F	33	1 сут. 1 ч	2636.0	21.3	17.2	4.1	0.008
	9	F	27	2 ч	980.0	19.3	10.8	8.5	0.020
	M ± SD		32.4 ± 4.8	10 сут. 7 ч	2344.2 ± 1018.4	45.9 ± 17.7	24.1 ± 10.2	19.6 ± 9.3	0.019 ± 0.006
II	10	M	40	2 ч	2747.0	15.7	9.6	6.1	0.006
	11	F	36	23 сут. 15 ч	1820.0	46.5	24.2	22.3	0.026
	12	M	39	23 ч	3538.0	13.2	6.2	7.0	0.004
	13	M	35	3 сут. 2 ч	1391.0	12.6	9.4	3.2	0.009
	14	F	39	2 сут.	3740.0	17.0	14.5	2.5	0.005
	15	F	39	21 ч	4450.0	21.3	11.4	9.9	0.005
	16	F	37	16 ч	2310.0	10.1	7.8	2.3	0.004
	17	M	40	6 ч	4550.0	13.6	11.3	2.3	0.003
	18	F	37	19 ч	2853.0	11.5	9.4	2.1	0.004
	19	M	37	4 сут.	3182.0	36.0	17.5	18.5	0.011
	20	F	39	24 сут.	5164.0	53.1	16.6	36.5	0.010
	21	F	37	1 сут. 11 ч	3770.0	17.1	0.3	16.8	0.005
	M ± SD		37.9 ± 1.6	5 сут. 10 ч	3292.9 ± 1134.7	22.3 ± 14.6	11.5 ± 6.1	10.8 ± 10.8	0.008 ± 0.006

DISCUSSION

For this work, we selected pleural fluid and air as the most stable lung components with regard to their physical parameters. Signal intensity varied in the area containing pleural fluid and air. Since there were no signs of pleuritis at autopsy, such variability was probably related to different scanner settings used by different tomography specialists. The presence of fluid of non-inflammatory origin (transudate-like) in the pleural cavity is indicative of early nonspecific postmortem changes [20] and is observed in all deaths, as proved by the autopsy.

Differences between groups with regard to airiness index were statistically insignificant, which might be due to a relatively small sample size and a need to assess lung pathology in each individual case and not in the whole group. However, we believe that AI <2.5 registered simultaneously in both lungs on T2-weighted images indicates pneumonia. This pattern was observed in 7 out of 9 cases in the experimental group. In two other cases, a higher AI was a result of concomitant pathologies: pneumothorax in case 1 and the edematous form of hemolytic disease in case 7. In the comparison group, AI was >2.5 for both lungs in 9 out of 12 cases. In three cases with airiness index <2.5 for both lungs indicating pneumonia, we detected multiple congenital defects (case 11) and false congenital diaphragmatic hernia with compression of the lungs (cases 13 and 18).

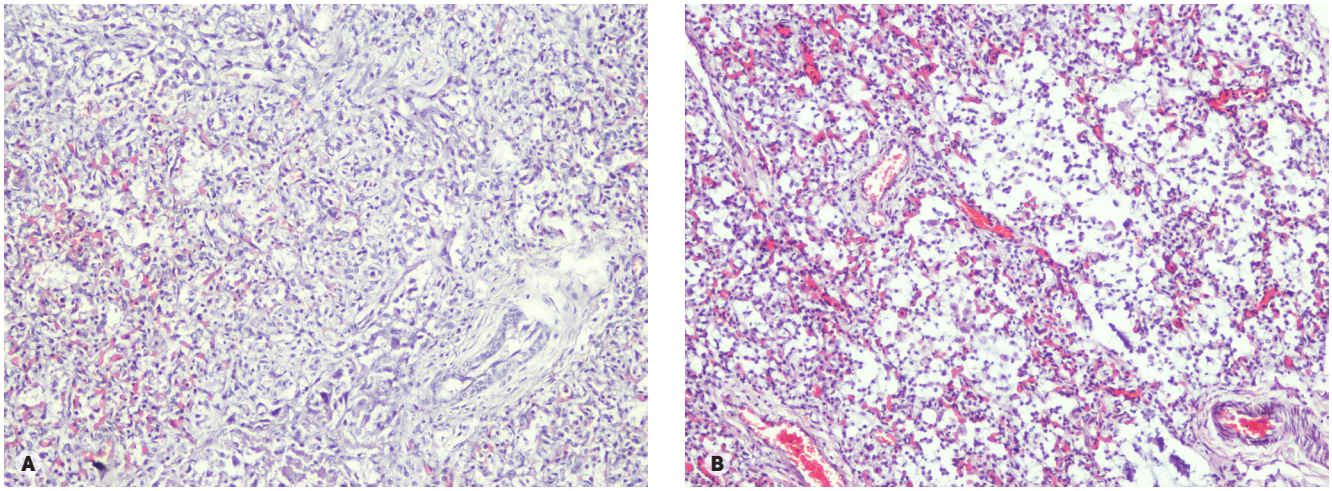

Fig. 1. Histological changes of lungs: **(A)** hypoplasia, **(B)** monocyte/macrophage pneumonia. Staining with hematoxylin and eosin, ×100

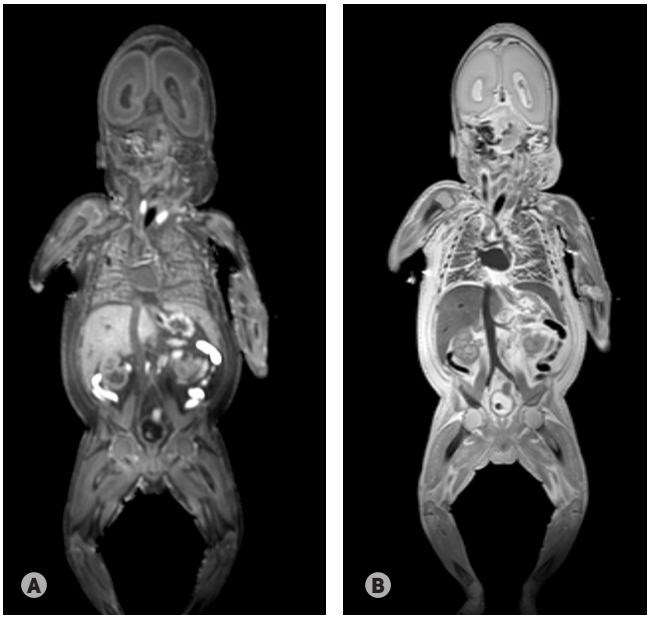

Fig. 2. Coronal MR-images of a dead neonate with congenital pneumonia (the experimental group): **(A)** T1-weighted image, **(B)** T2-weighted image

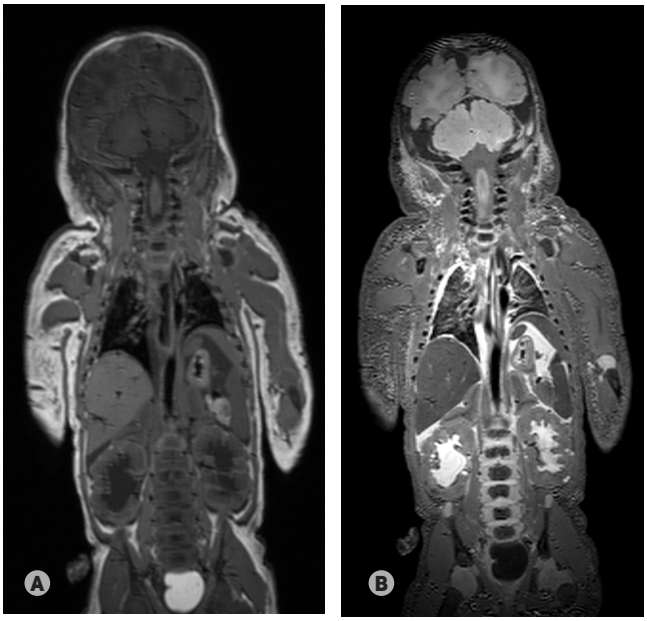

Fig. 3. Coronal MR-images of a dead neonate without lung pathology (the comparison group): **(A)** T1-weighted image, **(B)** T2-weighted image

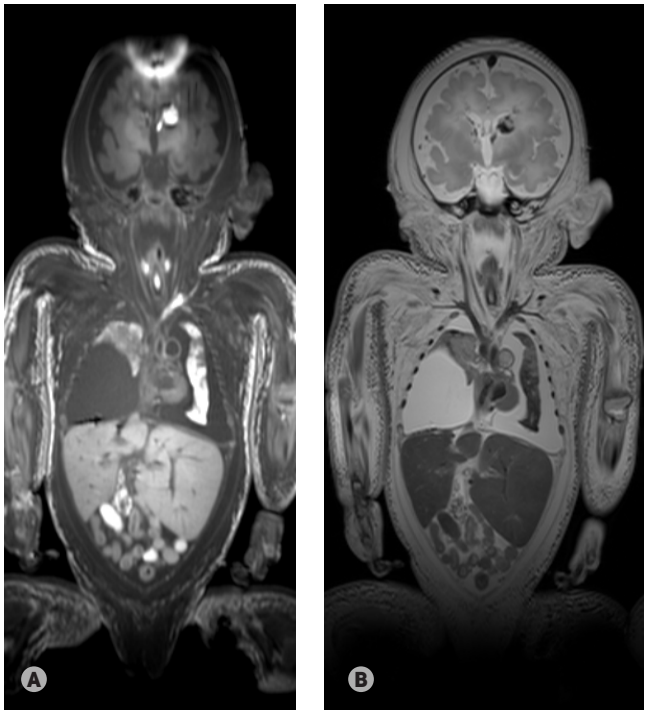

Fig. 4. Coronal MR-images of a dead neonate from the comparison group with hemorrhages in both lungs in the absence of pneumonia: **(A)** T1-weighted image, **(B)** T2-weighted image

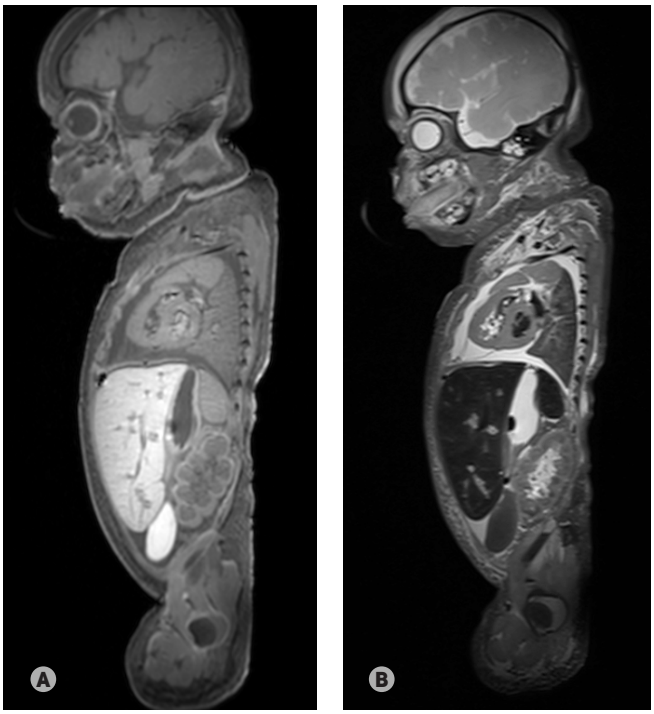

Fig. 5. Sagittal MR-images of a dead neonate from the comparison group with the intact left lung and right lung compressed by a diaphragmatic hernia

We think that airiness index allows for minimizing or eliminating measurement error related to the performance of an individual scanner and its settings.

Our results show a higher diagnostic efficacy of the applied technique as compared to the results obtained by Arthurs et al. [21], who demonstrated that sensitivity of the postmortem MRI in fetuses, newborns and children was 12.5 %, specificity was 92.6 % and the prognostic value of a positive result was 25 %. The reason here might be that the researchers visually assessed lung airiness and indurations to diagnose pneumonia. They also demonstrated that MRI diagnostic efficacy improves in older patients: the worst results (69.7 % of false negative results) were obtained for fetuses that had died before week 24 of gestation. On the one hand, MRI-based diagnosis of lung conditions, such as pneumonia, is a complicated clinical task; MR images of lungs are of low quality because of low proton density and a large amount of air-tissue gradients [22, 23]. On the other hand, back in the1990s Herold et al. [24] and Blum et al. [25] demonstrated moderate signal intensity on T1-weighted images and high signal intensity on T2-weighted images of immunocompromised patients with pulmonary aspergillosis. A definite MRI advantage is its ability to measure absolute and relative lung size that to some extent reflects progression of respiratory failure [26, 27].

Table 2 . Signal intensity and airiness index (AI) of lungs of dead neonates

Group	Case	T1-weighted images						T2-weighted images					
		Signal intensity				AI, RL	AI, LL	Signal intensity				AI, RL	AI, LL
		Right lung	Left lung	Air	Fluid			Right lung	Left lung	Air	Fluid		
I	1	128	664	6.0	515	4.0	0.8	120	330	3.0	880	7.3	2.7
	2	488	750	7.0	409	0.8	0.5	330	200	6.0	300	0.9	1.5
	3	538	517	9.0	379	0.7	0.7	416	345	4.5	735	1.8	2.1
	4	769	530	9.0	588	0.8	1.1	330	300	3.0	720	2.2	2.4
	5	566	492	6.0	293	0.5	0.6	380	290	1.0	523	1.4	1.8
	6	688	741	11	557	0.8	0.8	521	450	4.5	1122	2.2	2.5
	7	719	693	7.0	393	0.5	0.6	239	208	5.0	639	2.7	3.1
	8	479	595	12	444	0.9	0.7	446	453	6.0	920	2.1	2.0
	9	873	887	12	516	0.6	0.6	870	837	8.0	1120	1.3	1.3
	M ± SD	583.1 ± 217.2	652.1 ± 130.6	8.8 ± 2.4	454.9 ± 95.8	1.1 ± 1.1	0.7 ± 0.2	405.8 ± 209.8	379.2 ± 193.4	4.6 ± 2.1	773.2 ± 270.1	2.4 ± 1.9	2.2 ± 0.5
II	10	144	72	6.0	277	1.9	3.8	195	176	3.0	590	3.0	3.4
	11	938	871	9.6	736	0.8	0.8	552	465	4.0	996	2.1	2.1
	12	605	564	9.0	420	0.7	0.7	119	133	3.0	500	4.2	3.8
	13	624	585	7.0	430	0.7	0.7	363	365	3.0	672	1.9	1.8
	14	251	569	9.0	349	1.4	0.6	251	312	3.0	690	2.7	2.2
	15	477	384	10	340	0.7	0.9	265	237	3.0	598	2.3	2.5
	16	829	866	10	573	0.7	0.7	436	456	7.0	1140	2.6	2.5
	17	581	541	5.0	435	0.7	0.8	287	278	3.0	742	2.6	2.7
	18	524	388	7.0	261	0.5	0.7	279	396	4.0	583	2.1	1.5
	19	359	250	3.0	930	2.6	3.7	359	363	3.0	930	2.6	2.6
	20	504	678	3.0	341	0.7	0.5	446	323	2.0	926	2.1	2.9
	21	362	419	5.0	514	1.4	1.2	160	176	1.0	412	2.6	2.3
	M ± SD	516.5 ± 225.3	515.6 ± 232.8	7.0 ± 2.6	467.2 ± 197.5	1.1 ± 0.6	1.3 ± 1.1	309.3 ± 127.0	306.7 ± 109.6	3.3 ± 1.4	731.6 ± 220.5	2.6 ± 0.6	2.5 ± 0.6

Artifacts on MR images result from lung motion during aspiration and blood pulsations, especially in newborns [28]. They are not the case in postmortem MRI; however, we have to admit that there is a problem with accurate assessment of unspecific postmortem changes related to blood redistribution and autolysis [20, 29, 30]. To improve diagnostic accuracy and provide a possibility for differential diagnosis, some authors suggest histological analysis (apart from MRI) of lung tissue samples obtained percutaneously or endoscopically [31].

As postmortem MRI efficacy largely depends on the scanner type and its settings, special protocols should be elaborated considering scanner types, operating modes and corresponding software. Taylor et al. [32] inferred the necessity of using different protocols when analyzing the bodies of dead fetuses and infants.

CONCLUSIONS

Postmortem magnetic resonance imaging is effective in the detection of congenital pneumonia in stillborn babies and neonates who die shortly after birth. To verify the pathology, specific parameters of lung tissue on MR images are less important than a ratio of signal intensity in lung tissue to fluid signal intensity (pleural fluid in our case) on T2-weighted images. This ratio, or the airiness index, allows minimizing the impact of scanner settings on the procedure outcome. Differences in the airiness index between the studied groups of babies who died of congenital pneumonia and those who died of other causes were statistically insignificant because of a small sample size. A study with a larger sample may prove our hypothesis that airiness index less than 2.5 for both lungs on T2-weighted images can be used to diagnose congenital pneumonia.

References

1. Grebennikov VA, Ionov OM, Mostovoy AV, Ovsyannikov DYu, Degtyarev DN. Dykhatel'nye rasstroystva. In: Volodin NN, editor. Neonatologiya: natsional'noe rukovodstvo. Moscow: GEOTAR-Media; 2009. p. 246–92. Russian.
2. Duke T. Neonatal pneumonia in developing countries. Arch Dis Child Fetal Neonatal Ed. 2005; 90 (3): F211–9.
3. Shchegolev AI, Tumanova UN, Frolova OG. [Regional features of stillbirth in the Russian Federation]. In: Mezhregional'naya nauchno-prakticheskaya konferentsiya s mezhdunarodnym uchastiem "Aktual'nye voprosy sudebno-meditsinskoy ekspertizy i ekspertnoy praktiki v regional'nykh byuro sudebno-meditsinskoy ekspertizy na sovremennom etape"; 2013 Nov 21–22; Ryazan, Russia. Ryazan; 2013. p. 163–9. Russian
4. Shchegolev AI, Tumanova UN, Shuvalova MP, Frolova OG. Vrozhdennaya pnevmoniya kak prichina perinatal'noy smerti v Rossiyskoy Federatsii. Neonatologiya: novosti, mneniya, obuchenie 2016; 2: 61–6. Russian.
5. Khrushchelevski E, Shperl'-Zeyfridova G, Chervakov VF, editors.

Sektsiya trupov plodov i novorozhdennykh. Moscow: Medgiz; 1962. p. 224. Russian.
6. Sorokin AF. Pnevmonii novorozhdennykh. In: Ivanovskaya TE, Leonova LV, editors. Patologicheskaya anatomiya bolezney ploda i rebenka. Moscow: Meditsina; 1989. p. 208–10. Russian.
7. Vishnevskiy AA, Karmazanovskiy GG, Kokov LS, Bykov GA, Borisov VV, Shchegolev AI. Sovremennye vozmozhnosti diagnostiki v torakal'noy khirurgii. Khirurgiya. Zhurnal imeni N. I. Pirogova. 2003; 3: 92–5. Russian.
8. Verschakelen JA, De Wever W. Computed tomography of the lung. A pattern approach. Berlin: Springer-Verlag; 2007.
9. Tyurin IE. Novye gorizonty torakal'noy khirurgii. Poliklinika. 2013; 5 (1): 12–7. Russian.
10. Michiue T, Sakurai T, Ishikawa T, Oritani S, Maeda H. Quantitative analysis of pulmonary pathophysiology using postmortem computed tomography with regard to the cause of death. Forensic Sci Int. 2012; 220 (1–3): 232–8.
11. Fedoseeva VK, Tumanova UN, Lyapin VM, Voevodin SM, Shchegolev AI. Vozmozhnosti ispol'zovaniya mul'tispiral'noy komp'yuternoy tomografii v posmertnoy diagnostike patologii plodov i novorozhdennykh. Rossiyskiy elektronnyy zhurnal luchevoy diagnostiki. 2013; 3 (S2): 448. Russian.
12. Puderbach M, Kauczor HU. Can lung MR replace lung CT? Pediatr Radiol. 2008; 38 Suppl 3: S439-51.
13. Eibel RP, Herzog O, Dietrich C, Rieger H, Ostermann M, Reiser S, et al. Nachweis von pneumonischen Infiltraten mit der MRT. Radiologe. 2006; 46: 267–74. German.
14. Rupprecht T, Böwing B, Kuth R, Deimling M, Rascher W, Wagner M. Steady-state free precession projection MRI as a potential alternative to the conventional chest X-ray in pediatric patients with suspected pneumonia. Eur Radiol. 2002; 12 (11): 2752–6.
15. Leutner CC, Gieseke J, Lutterbey G, Kuhl C K, Glasmacher A, Wardelmann E, et al. MR-imaging of pneumonia in immunocompromised patients: comparison with helical CT. AJR Am J Roentgenol. 2000; 175 (2): 391–7.
16. Barber JL, Sebire NJ, Chitty LS, Taylor AM, Arthurs OJ. Lung aeration on post-mortem magnetic resonance imaging is a useful marker of live birth versus stillbirth. Int J Legal Med. 2015; 129 (3): 531–6.
17. Tumanova UN, Bychenko VG, Lyapin VM, Voevodin SM, Shchegolev AI, Sukhikh GT, inventors. Kulakov Research Center for Obstetrics, Gynecology and Perinatology, assignee. Sposob differentsial'noy diagnostiki mertvorozhdennogo i smerti novorozhdennogo posle rozhdeniya. Patent. RU 2577454 2015 Jun 18. Russian.
18. Lally PJ, Arthurs O, Addison S, Alavi A, Sebire NJ, Taylor A, et al. Estimating maceration severity using whole body magnetic resonance T2 relaxometry. Arch Dis Child Fetal Neonatal. 2014; (S1): A92–3.
19. Tumanova UN, Lyapin VM, Voevodin SM, Shchegolev AI, Sukhikh GT. Postmortem MRI to determine the time of intrauterine fetal death. Vichows Archiv. 2015; 467 (S1): 27.
20. Tumanova UN, Shchegolev AI. Nespetsificheskie posmertnye izmeneniya, vyyavlyaemye pri komp'yuterno-tomograficheskom issledovanii. In: Mezhdunarodnaya konferentsiya “Kriminalisticheskoe soprovozhdenie rassledovaniya prestupleniy: problemy i puti ikh resheniya”; 2016 Feb 19; Moscow, Russia. Moscow; 2016. p. 525–9. Russian.
21. Arthurs OJ, Thayyil S, Olsen OE, Addison S, Wade A, Jones R, et al. Diagnostic accuracy of post-mortem MRI for thoracic abnormalities in fetuses and children. Eur Radiol. 2014; 24: 2876–84.
22. Bankier AA, O’Donnell CR, Mai VM, Storey P, De Maertelaer V, Edelman RR, et al. Impact of lung volume on MR signal intensity changes of the lung parenchyma. J Magn Reson Imaging. 2004; 20 (6): 961–6.
23. Ciet P, Tiddens HAWM, Wielopolski PA, Wild JM, Lee EY, et al. Magnetic resonance imaging in children: common problems and possible solutions for lung and airways imaging. Pediatr Radiol. 2015; 45 (13): 1901–5.
24. Herold CJ, Mostbeck G, Kramer J, Schwarzinger I, Wrba F, Haller J, et al. Invasive pulmonary aspergillosis: radiologic and magnetic resonance tomographic characteristics. Rofo. 1990; 153 (5): 569–74.
25. Blum U, Windfuhr M, Buitrago-Tellez C, Sigmund G, Herbst EW, Langer M. Invasive pulmonary aspergillosis. MRI, CT and plain radiographic findings and their contribution for early diagnosis. Chest. 1994; 106 (4): 1156–61.
26. Thayyil S, Schievanoa S, Robertson NJ, Jones R, Chitty LS, Sebire NJ, et al. A semi-automated method for non-invasive internal organ weight estimation by post-mortem magnetic resonance imaging in fetuses, newborns and children. Eur J Radiol. 2009; 72: 321–6.
27. Tumanova UN, Bychenko VG, Liapin VM, Voevodin SM, Shchegolev AI. [Congenital Diaphragmatic Hernia in a Newborn: MRI – Pathomorphological Comparisons]. Medical Visualization. 2014; 4: 72–83. Russian.
28. Liszewski MC, Hersman FW, Altes TA, Ohno Y, Ciet P, Warfield SK, et al. Magnetic resonance imaging of pediatric lung parenchyma, airways, vasculature, ventilation, and perfusion: state of the art. Radiol Clin N Am. 2013; 51 (4): 555–82.
29. Dubrova SE, Vishnyakova MV, Kinle AF, Filimonov BA. [Features of computed tomography autopsy: the problem of interpretation of specific and nonspecific artifacts]. Diagnostic radiology and radiotherapy. 2016; 1: 25–40. Russian.
30. Tumanova UN, Shchyogolev AI. [Postmortem Magnetic Resonance Tomography of Fetuses and Newborns]. Medical Visualization. 2015; 5: 128–36. Russian.
31. Sebire NJ, Weber MA, Thayyil S, Mushtaq I, Taylor A, Chitty LS. Minimally invasive perinatal autopsies using magnetic resonance imaging and endoscopic postmortem examination (“keyhole autopsy”): feasibility and initial experience. J Matern Fetal Neonatal Med. 2012; 25 (5): 513–8.
32. Taylor AM, Sebire NJ, Ashworth MT, Schievano S, Scott RJ, Wade A, et al. Postmortem Cardiovascular Magnetic Resonance Imaging in Fetuses and Children: A Masked Comparison Study With Conventional Autopsy. Circulation. 2014; 129 (19): 1937–44.

Литература

1. Гребенников В. А., Ионов О. М., Мостовой А. В., Овсянников Д .Ю., Дегтярев Д. Н. Дыхательные расстройства. В кн.: Володин Н. Н., редактор. Неонатология: национальное руководство. М.: ГЭОТАР-Медиа, 2009. с. 246–92.
2. Duke T. Neonatal pneumonia in developing countries. Arch Dis Child Fetal Neonatal Ed. 2005; 90 (3): F211–9.
3. Щеголев А. И., Туманова У. Н., Фролова О. Г. Региональные особенности мертворождаемости в Российской Федерации. В сб.: Межрегиональная научно-практическая конференция с международным участием «Актуальные вопросы судебно-медицинской экспертизы и экспертной практики в региональных бюро судебно-медицинской экспертизы на современном этапе»; 21–22 ноября 2013 г.; Рязань, Россия. Рязань; 2013. с. 163–9.
4. Щеголев А. И., Туманова У. Н., Шувалова М. П., Фролова О. Г. Врожденная пневмония как причина перинатальной смерти в Российской Федерации. Неонатология: новости, мнения, обучение. 2016; 2: 61–6.
5. Хрущелевски Э., Шперль-Зейфридова Г., Черваков В. Ф., редакторы. Секция трупов плодов и новорожденных. М.: Медгиз; 1962. с. 224.
6. Сорокин А. Ф. Пневмонии новорожденных. В книге: Ивановская Т. Е., Леонова Л. В., редакторы. Патологическая анатомия болезней плода и ребенка. М.: Медицина; 1989. с. 208–10.
7. Вишневский А. А., Кармазановский Г. Г., Коков Л. С., Быков Г. А., Борисов В. В., Щеголев А. И. Современные возможности диагностики в торакальной хирургии. Хирургия.

Журнал имени Н. И. Пирогова. 2003; 3: 92–5.
8. Verschakelen JA, De Wever W. Computed tomography of the lung. A pattern approach. Berlin: Springer-Verlag; 2007.
9. Тюрин И. Е. Новые горизонты торакальной хирургии. Поликлиника. 2013; 5 (1): 12–7.
10. Michiue T, Sakurai T, Ishikawa T, Oritani S, Maeda H. Quantitative analysis of pulmonary pathophysiology using postmortem computed tomography with regard to the cause of death. Forensic Sci Int. 2012; 220 (1–3): 232–8.
11. Федосеева В. К., Туманова У. Н., Ляпин В. М., Воеводин С. М., Щеголев А. И. Возможности использования мультиспиральной компьютерной томографии в посмертной диагностике патологии плодов и новорожденных. Российский электронный журнал лучевой диагностики. 2013; 3 (S2): 448.
12. Puderbach M, Kauczor HU. Can lung MR replace lung CT? Pediatr Radiol. 2008; 38 Suppl 3: S439–51.
13. Eibel RP, Herzog O, Dietrich C, Rieger H, Ostermann M, Reiser S, et al. Nachweis von pneumonischen Infiltraten mit der MRT. Radiologe. 2006; 46: 267–74. German.
14. Rupprecht T, Böwing B, Kuth R, Deimling M, Rascher W, Wagner M. Steady-state free precession projection MRI as a potential alternative to the conventional chest X-ray in pediatric patients with suspected pneumonia. Eur Radiol. 2002; 12 (11): 2752–6.
15. Leutner CC, Gieseke J, Lutterbey G, Kuhl C K, Glasmacher A, Wardelmann E, et al. MR-imaging of pneumonia in immunocompromised patients: comparison with helical CT. AJR Am J Roentgenol. 2000; 175 (2): 391–7.
16. Barber JL, Sebire NJ, Chitty LS, Taylor AM, Arthurs OJ. Lung aeration on post-mortem magnetic resonance imaging is a useful marker of live birth versus stillbirth. Int J Legal Med. 2015; 129 (3): 531–6.
17. Туманова У. Н., Быченко В. Г., Ляпин В. М., Воеводин С. М., Щеголев А. И., Сухих Г. Т., авторы. Научный центр акушерства, гинекологии и перинатологии имени В. И. Кулакова, патентообладатель. Способ дифференциальной диагностики мертворожденного и смерти новорожденного после рождения. Патент РФ №2577454 от 18.06.2015.
18. Lally PJ, Arthurs O, Addison S, Alavi A, Sebire NJ, Taylor A, et al. Estimating maceration severity using whole body magnetic resonance T2 relaxometry. Arch Dis Child Fetal Neonatal. 2014; (S1): A92–3.
19. Tumanova UN, Lyapin VM, Voevodin SM, Shchegolev AI, Sukhikh GT. Postmortem MRI to determine the time of intrauterine fetal death. Vichows Archiv. 2015; 467 (S1): 27.
20. Туманова У. Н., Щеголев А. И. Неспецифические посмертные изменения, выявляемые при компьютерно-томографическом исследовании. В сборнике: Международная конференция «Криминалистическое сопровождение расследования преступлений: проблемы и пути их решения»; 19 февраля 2016 г.; Москва, Россия. М.; 2016. с. 525–9.
21. Arthurs OJ, Thayyil S, Olsen OE, Addison S, Wade A, Jones R, et al. Diagnostic accuracy of post-mortem MRI for thoracic abnormalities in fetuses and children. Eur Radiol. 2014; 24: 2876–84.
22. Bankier AA, O'Donnell CR, Mai VM, Storey P, De Maertelaer V, Edelman RR, et al. Impact of lung volume on MR signal intensity changes of the lung parenchyma. J Magn Reson Imaging. 2004; 20 (6): 961–6.
23. Ciet P, Tiddens HAWM, Wielopolski PA, Wild JM, Lee EY, et al. Magnetic resonance imaging in children: common problems and possible solutions for lung and airways imaging. Pediatr Radiol. 2015; 45 (13): 1901–5.
24. Herold CJ, Mostbeck G, Kramer J, Schwarzinger I, Wrba F, Haller J, et al. Invasive pulmonary aspergillosis: radiologic and magnetic resonance tomographic characteristics. Rofo. 1990; 153 (5): 569–74.
25. Blum U, Windfuhr M, Buitrago-Tellez C, Sigmund G, Herbst EW, Langer M. Invasive pulmonary aspergillosis. MRI, CT and plain radiographic findings and their contribution for early diagnosis. Chest. 1994; 106 (4): 1156–61.
26. Thayyil S, Schievanoa S, Robertson NJ, Jones R, Chitty LS, Sebire NJ, et al. A semi-automated method for non-invasive internal organ weight estimation by post-mortem magnetic resonance imaging in fetuses, newborns and children. Eur J Radiol. 2009; 72: 321–6.
27. Туманова У. Н., Быченко В. Г., Ляпин В.М., Воеводин С. М., Щеголев А. И. Врожденная диафрагмальная грыжа у новорожденного: МРТ – патоморфологические сопоставления. Медицинская визуализация. 2014; 4: 72–83.
28. Liszewski MC, Hersman FW, Altes TA, Ohno Y, Ciet P, Warfield SK, et al. Magnetic resonance imaging of pediatric lung parenchyma, airways, vasculature, ventilation, and perfusion: state of the art. Radiol Clin N Am. 2013; 51 (4): 555–82.
29. Дуброва С. Э., Вишнякова М. В., Кинле А. Ф., Филимонов Б. А. Особенности компьютерной томографии трупа: проблема интерпретации специфических и неспецифических артефактов. Лучевая диагностика и терапия. 2016; 1: 25–40.
30. Туманова У. Н., Щеголев А. И. Посмертная магнитно-резонансная томография плодов и новорожденных. Медицинская визуализация. 2015; 5: 128–36.
31. Sebire NJ, Weber MA, Thayyil S, Mushtaq I, Taylor A, Chitty LS. Minimally invasive perinatal autopsies using magnetic resonance imaging and endoscopic postmortem examination ("keyhole autopsy"): feasibility and initial experience. J Matern Fetal Neonatal Med. 2012; 25 (5): 513–8.
32. Taylor AM, Sebire NJ, Ashworth MT, Schievano S, Scott RJ, Wade A, et al. Postmortem Cardiovascular Magnetic Resonance Imaging in Fetuses and Children: A Masked Comparison Study With Conventional Autopsy. Circulation. 2014; 129 (19): 1937–44.

INFLUENCE OF ANESTHETIC TECHNIQUES ON OCCURRENCE OF POSTOPERATIVE COGNITIVE DYSFUNCTION IN ELDERLY PATIENTS UNDERGOING GYNECOLOGICAL SURGERY

Krasenkova EA[1] ✉, Ovechkin AYu[2], Pyregov AV[2]

[1] Faculty of Pediatrics,
Pirogov Russian National Research Medical University, Moscow, Russia

[2] Department of Anesthesiology and Resuscitation,
Kulakov Research Center for Obstetrics, Gynecology and Perinatology, Moscow, Russia

Postoperative cognitive dysfunction (POCD) is a disorder that develops in the early postoperative period, persisting for several days or weeks and leading to decrease in higher cortical functions (speech, memory, attention, etc.). POCD is often associated with anesthetic techniques and drugs. This paper studied the effect of general, neuraxial and combined anesthesia on POCD development in elderly women undergoing gynecological surgery. The study featured 43 patients (mean age 65,0 ± 2.2 years). There were 12 women in the general anesthesia group, 23 in the neuraxial anesthesia group, and 8 women in the combined anesthesia group. Intraoperative monitoring included electrocardiography, non-invasive blood pressure measurement, determination of blood oxygen saturation level (rSO_2) and determination of bispectral index (BIS monitoring). A day before surgery and on the 5th day after the surgery, neuropsychological tests were carried out through tracking test, Mini-Mental State Examination and frontal assessment battery. All intraoperative indicators were normal in all the patients. POCD was diagnosed in 3 women who were under general anesthesia, in 7 women under neuraxial anesthesia and 2 under the combined group (25, 30 and 25 % relative to the total number of patients in the groups, respectively). The average rSO_2 value was below the initial level in all groups: below by 6 % in the general anesthesia group, by 15 % in the neuraxial group, and by 10 % in the combined group. However, the differences were statistically insignificant (p >0.05). The study found no relationship between anesthetic techniques and POCD.

Keywords: postoperative cognitive dysfunction, cognitive impairment, general anesthesia, neuraxial anesthesia, combined anesthesia, elderly age

✉ **Correspondence should be addressed:** Ekaterina Krasenkova
ul. Marshala Nedelina, d. 34, korp. 1, kv. 99, Moscow, Russia, 121471; krasenkova.ea@gmail.com

Received: 09.06.2016 **Accepted:** 16.08.2016

ВЛИЯНИЕ МЕТОДА АНЕСТЕЗИИ НА ВОЗНИКНОВЕНИЕ ПОСЛЕОПЕРАЦИОННОЙ КОГНИТИВНОЙ ДИСФУНКЦИИ У ПАЦИЕНТОВ ПОЖИЛОГО ВОЗРАСТА ПРИ ОПЕРАЦИЯХ В ГИНЕКОЛОГИИ

Е. А. Красенкова[1] ✉, А. Ю. Овечкин[2], А. В. Пырегов[2]

[1] Педиатрический факультет,
Российский национальный исследовательский медицинский университет имени Н. И. Пирогова, Москва

[2] Отделение анестезиологии-реанимации,
Научный центр акушерства, гинекологии и перинатологии имени академика В. И. Кулакова, Москва

Послеоперационная когнитивная дисфункция (ПОКД) — расстройство, развивающееся в ранний послеоперационный период, сохраняющееся в течение нескольких дней или недель и проявляющееся снижением высших корковых функций (речи, памяти, внимания и др.). Возникновение ПОКД часто связывают с методом анестезиологического обеспечения и препаратами. В работе изучено влияние общей, нейроаксиальной и сочетанной анестезии на развитие ПОКД у женщин пожилого и старческого возраста при операциях в гинекологии. В исследование включили 43 пациентки (средний возраст — 65,0 ± 2,2 года). В группе с общей анестезией было 12 женщин, с нейроаксиальной — 23, с сочетанной — 8. Интраоперационный мониторинг включал снятие электрокардиограммы, неинвазивное измерение артериального давления, определение уровня насыщения крови кислородом (rSO_2), определение биспектрального индекса (BIS-мониторинг). За день до операции и на 5-й день после нее проводили нейропсихологическое тестирование с помощью теста слежения, краткой шкалы оценки психического статуса и батареи оценки лобной функции. Все интраоперационные показатели у всех пациенток были в норме. ПОКД была диагностирована у 3 женщин, находившихся под общей анестезией, у 7 — под нейроаксиальной и у 2 — под сочетанной (25, 30 и 25 % относительно общего числа пациенток в группах соответственно). Среднее значение показателя rSO_2 во всех группах было ниже исходного уровня: при общей анестезии — на 6 %, при нейроаксиальной — на 15 %, при сочетанной — на 10 %, однако различия были статистически незначимыми (p >0,05). Связь между типом анестезии и развитием ПОКД не была выявлена.

Ключевые слова: послеоперационная когнитивная дисфункция, когнитивное расстройство, общая анестезия, нейроаксиальная анестезия, сочетанная анестезия, пожилой возраст

✉ **Для корреспонденции:** Красенкова Екатерина Алексеевна
121471, г. Москва, ул. Маршала Неделина, д. 34, корп. 1, кв. 99; krasenkova.ea@gmail.com

Статья поступила: 09.06.2016 **Статья принята в печать:** 16.08.2016

Postoperative cognitive dysfunction (POCD) is one of the pressing problems faced by modern anesthesiology. It is a disorder that develops in the early postoperative period, persisting for several days or weeks, and rarely for months. POCD is clinically manifested in the form of memory impairment, trouble concentrating, long holding of attention, and other disorders in higher cortical functions (thinking, speech, etc.). A patient with postoperative cognitive dysfunction develops learning problems, lower mental capacity and deteriorating mood (depression occurs) [1]. This can lead to reduced quality of life [2–4]. POCD is not included in the International Statistical Classification of Diseases and Related Health Problems (ICD-10) despite its high prevalence and the strong it attracts from the scientific community. Mild cognitive disorder (F06.7) — a diagnosis close to POCD — is the one included in the ICD.

The exact mechanism by which POCD develops still remains unknown. A number of studies associate the occurrence of this condition with the effect of anesthetics and depth of anesthesia [5–7]. Bianchi et al. [8] found that inhaled anesthetics affect amyloidogenesis in the brain, thereby promoting POCD. Monk et al. [7] suggested that inhalation anesthetics may be neurotoxic and cause brain aging, but that there are no human data evaluating this hypothesis to date. At the same time, the impact of surgical stress [9] and patients' preoperative status [7, 9] on POCD has been pointed out. For example, in patients who have suffered from cerebral infarction, the course of early POCD significantly worsens even in the absence of residual defects. Some researchers also consider POCD as a risk factor for Alzheimer's disease [10], while the etiology of both disorders remains unclear.

POCD and regional oxygen saturation index (rSO_2) have been found to be related: intraoperative decline in rSO_2 is a predictor of the disorder. Li et al. [11] showed this relationship in thoracic surgery in one-lung ventilation, while Papadopoulos et al. [12] did so through surgery for hip fractures in patients older than 75 years. It was advised that cerebral oximeter should be applied not only to identify the risk of POCD but also to determine the tactics for postoperative management [11, 13–16]. Some researchers have also reported on the relationship of cerebral oximetry and specific anesthetic agents [17, 18] with premorbid POCD background [19]. Salazar et al. [20] assumed that postoperative cognitive dysfunction develops with lower rSO_2 in patients undergoing surgery in a certain position. Although they were unable to identify significant association, the authors concluded that surgery protocols, which involve rSO_2 measurement, reduce the risk of POCD. Other researchers have noted a decline in rSO_2 in patients operated upon in a beach chair position [21].

Elderly age is considered an important risk factor for POCD. It is associated with natural decline of cognitive functions and with a variety of diseases, such as hypertension, atherosclerosis, coronary artery disease, thrombosis, stroke, etc. [1, 3, 6, 7, 12–15]. Moreover, the number of surgical procedures in elderly patients is growing as the number of articles published on POCD in elderly age increases [4]. Other risk factors include: organic brain syndrome and mental disorders [1, 3]; extent and duration of sugery, intra- and post-operative complications (hemorrhage, hemodynamic responses, etc.) [3–6]; chronic pain syndrome [8]; classes III-IV of the physical status classification by the American Society of Anesthesiologists]22].

The aim of this study was to evaluate the effects of anesthesia (method, drugs) on the cognitive status of elderly patients undergoing gynecological surgery by comprehensive neuropsychological evaluation.

METHODS

The study conducted in 2015 featured female patients from the Kulakov Research Center for Obstetrics, Gynecology and Perinatology. The inclusion criteria were: 60–80 years of age and gynecological diseases requiring elective surgery. The exclusion criteria were: burdened neurological history and acute cerebrovascular diseases; organic lesions of the central nervous system, epilepsy and history of mental illness; severe concussion, stroke; severe somatic pathology; dementia (24 points or more in the Mini-Mental State Examination questionnaire); burdened alcohol, drug or poison history; expansion of surgical intervention; decompensation extragenital pathology. The study included 43 patients aged 65.0 ± 2.2 years.

Vaginal hysterectomy was carried out on 19 patients, laparoscopic hysterectomy on 8 patients, laparoscopic adnexectomy on 7 patients, laparotomy hysterectomy on 6 patients, laparoscopic cholecystectomy on 2 patients and stoma closure on 1 patient. Three types of anesthesia were used: general anesthesia (12 patients with an average age of 66.0 ± 5.6 years), neuraxial anesthesia (23 patients with an average age of 66.0 ± 4.9 years) and combined anesthesia (8 patients with an average age of 68.0 ± 6.4 years). Doses of preparations were selected individually according to the manufacturer's recommendations, age and sensitivity of the patients, as well as the required anesthetic effect. Then, the average doses of drugs were given for the patient groups (divided by type of anesthesia).

General anesthesia was performed according to the following procedure. Atropine sulfate premedication (Dalkhimpharm, Russia) and Dexamethasone premedication (Krka, Slovenia) were carried out. Propofol (AstraZeneca, UK) 1.3 ± 1.5 mg/kg and rocuronium (Hameln Pharmaceuticals, Germany) 0.9 mg/kg were used for induction. After induction, tracheal intubation was performed. Narcotic and respiratory mixture sevoflurane (Abbott Laboratories, UK) and oxygen with maintenance of minimum alveolar concentration at a 0.8–1.0 level were used to maintain anesthesia.

Spinal-epidural anesthesia was used for neuraxial anesthesia. Puncture of the spinal and epidural space was performed on the level of segments 2–3 of the lumbar vertebrae (L2–L3). Hyperbaric bupivacaine (AstraZeneca) was administered in the spinal space at a dose of 8.95 ± 3.05 mg. Ropivacaine (AstraZeneca) was administered in the epidural at a dose of 68.5 ± 12.0 mg. The punctures were preceded by atropine sulfate premedication and dexamethasone premedication.

Combined anesthesia consisted of general anesthesia and installation of an epidural catheter at the L1–L3 level after standard premedication (atropine sulphate and dexamethasone). Induction, tracheal intubation and general anesthesia were then performed. Ropivacaine (1 mg/kg) was administered in the epidural space.

Intraoperative monitoring was conducted according to the Oxford Standard (ECG, blood pressure, SpO_2) [23] with the Infinity Delta monitor (Draeger, Germany). BIS monitoring (measurement of bispectral index to assess the level of anesthesia and brain sedation) was performed using monitor console Infinity BISx SmartPod (Draeger). The INVOS 5100C monitor (Covidien AG, USA) was used for cerebral oximetry.

The cognitive status of the patients was assessed on a day before and 5th day after the surgery using three neuropsychological tests — Trail Making Test, Mini-Mental State Examination and frontal assessment battery.

Trail Making Test (TMT) [24] allows to evaluate the patient's attention, speed of thinking and coordination. It consists of two parts: In part A, the patient is instructed to connect a set of numbers from 1 to 25, while in part B, the patient is instructed to connect alternating letters and numbers in ascending order. The test is allocated 300 seconds. After that, the time taken by the patient to perform the task is estimated, and the degree of dysfunction is determined based on the scale of results (three degrees).

The Mini-Mental State Examination [25] includes 9 tests evaluating a patient's orientation in space and time, attention, memory and speech. The result is given in points.

Frontal assessment battery [26] consists of 6 tasks that allow to estimate the patient's ability to generalize, attentiveness, ability to concentrate, state of speech processes and motor activity. The results are also given in points.

The average values and standard deviations of test results before and after the operation were calculated for each group of patients and were compared for the purpose of identifying POCD — if after surgery, test result turned out to be by more than 10 % worse than the result prior to surgery, cognitive disorder was diagnosed. The average values and standard deviations of the rSO_2 index before and after surgery were also calculated for each group of patients. Statistical data analysis was performed using Student's t-test ($p < 0.05$).

The study was approved by the Biomedical Research Ethics Committee of the Kulakov Research Center for Obstetrics, Gynecology and Perinatology (Minutes No 1 of 29 January 2015). All the patients gave their written informed consent to participate in the study.

RESULTS

Electrocardiograms obtained in the course of surgery were characteristic of the age norm. Saturation was maintained at 97–99 %. Bispectral index remained normal (45–60 %), thereby allowing to exclude the influence of inadequate or excessive brain sedation on the patients' cognitive functions.

The average value of the rSO_2 index during surgery in all the three groups differed (decreased) from the baseline values as follows: 6 % decrease for general anesthesia, 15 % decrease for neuraxial anesthesia, and 10 % decrease for combined anesthesia. However, the differences were statistically not significant ($p > 0.05$).

Assessment of cognitive status of patients (by Trail Making Test and Frontal Assessment Battery) identified POCD in 12 patients: 3 women for general anesthesia, 7 for neuraxial anesthesia and 2 for combined anesthesia. However, ithe number of patients with POCD in each group turned out to be almost equal 25, 30 and 25 %, respectively. Cognitive deficits in the group of patients with general anesthesia averaged 23.8 and 25 % for the FAB and TMT respectively (see table). The average values of these same indicators in the group of patients with neuraxial anesthesia were equal to 18.6 and 27.9 % respectively, while in the group of patients with combined anesthesia — 25.0 and 23.7 % respectively. Postoperative test results obtained via MMSE differed from preoperative values by less than 10 %. Data were statistically significant only for the FAB and TMT tests ($p < 0.05$). It can be assumed that the MMSE test is less sensitive with respect to postoperative cognitive dysfunction.

DISCUSSION

Some researchers have noted that general anesthesia is related to more significant decline in rSO2 than neuraxial [27–29], while others believe that there are no differences [30, 31]. Indeed, the neuraxial block leads to changes in the central hemodynamics, which can affect the oxygenation level of the cerebral blood flow. However, in our work, significant reduction in rSO_2 during neuraxial anesthesia was unreliable. Perhaps this is due to the insufficient sample size.

Many authors attribute the occurrence of POCD to the type of anesthetic management [1, 2, 5, 7, 17, 28, 30]. But most researchers have formed a pilot group of elderly people who are predisposed to cognitive dysfunction due to age-related changes in the brain. In our study, we were not able to detect differences between the three types of anesthesia. Perhaps, extent of surgery, surgical stress and quality of patient management in the postoperative period are POCD risk factors to a greater degree [32, 33].

Children's surgery and cardiology could provide indirect evidence that type of anesthesia has no influence on POCD occurrence. In pediatric anesthesiology, the issue of cognitive dysfunction is as acute as in adults. But many researchers point out that despite individual POCD cases in school-age children, one cannot claim that a particular anaesthetic support has a higher effect on POCD development than the others [34]. Cardiac surgery procedures are associated with brain hypoxia, which should lead to cognitive dysfunction. However, some researchers studying the problem also reported that anesthesia type has no effect on POCD incidence [35].

CONCLUSIONS

Our study showed that the likelihood of developing postoperative cognitive dysfunction in elderly women undergoing gynecological surgeries does not depend on the type of anesthesia. Reduced cerebral oxygenation could be the cause of more frequent occurrence of POCD in neuraxial anesthesia. However, our findings on reduction of rSO_2 in neuraxial anesthesia are not statistically significant. The hypothesis should be further tested in a group consisting of large number of patients. We also noted that Trail Making Test and Frontal Assessment Battery are the most sensitive POCD detection tools.

Neuropsychological test results

Group (type of anesthesia)	Number of patients	Detected POCD, patients (percentage in the group, %)	FAB score			MMSE score			TMT score		
			before surgery, p	after surgery, p	change, %	before surgery, p	after surgery, p	change, %	before surgery, p	after surgery, p	change, %
General	12	3 (25.0)	14.5 ± 1.7	11.0 ± 1.3	24.0*	26.1 ± 4.0	24.3 ± 3.7	7.0	46.5 ± 6.6	62.0 ± 8.9	25.0*
Neuraxial	23	7 (30.0)	14.3 ± 2.9	11.6 ± 2.4	18.6*	26.5 ± 3.1	24.2 ± 2.2	8.7	48.4 ± 4.5	67.2 ± 6.2	28.0*
Combined	8	2 (25.0)	13.1 ± 3.6	9.8 ± 2.7	25.0*	25.1 ± 2.9	23.4 ± 2.7	6.9	50.2 ± 5.0	65.8 ± 6.5	23.8*

Note. FAB — Frontal Assessment Battery, MMSE — Mini-Mental State Examination, TMT — Trail Making Test. * — $p < 0.05$ (when comparing the average values of the attribute in the group before and after surgery).

References

1. Solenkova AA, Bondarenko AA, Lubnin AYu, Dzyubanova NA. [Postoperative cognitive dysfunction in elderly patients]. Anesteziologiya i reanimatologiya. 2012; 4: 13–9. Russian.
2. Newman S, Stygall J, Hirani S, Shaefi S, Maze M. Postoperative cognitive dysfunction after noncardiac surgery: a systematic review. Anesthesiology. 2007 Mar; 106 (3): 572–90.
3. Dijkstra JB, Houx PJ, Jolles J. Cognition after major surgery in the elderly: test performance and complaints. Br J Anaesth. 1999 Jun; 82 (6): 867–74.
4. Berger M, Nadler JW, Browndyke J, Terrando N, Ponnusamy V, Cohen HJ, et al. Postoperative Cognitive Dysfunction: Minding the Gaps in Our Knowledge of a Common Postoperative Complication in the Elderly. Anesthesiol Clin. 2015 Sep; 33 (3): 517–50.
5. Monk TG, Price CC. Postoperative cognitive disorders. Curr Opin Crit Care. 2011 Aug; 17 (4): 376–81.
6. Newfield P. Postoperative cognitive dysfunction. F1000 Med Rep. 2009 Feb 24; 1: 14.
7. Monk TG, Weldon BC, Garvan CW, Dede DE, van der Aa MT, Heilman KM, et al. Predictors of cognitive dysfunction after major noncardiac surgery. Anesthesiology. 2008 Jan; 108 (1): 18–30.
8. Bianchi SL, Tran T, Liu C, Lin S, Li Y, Keller JM, et al. Brain and behavior changes in 12-month-old Tg2576 and nontransgenic mice exposed to anesthetics. Neurobiol Aging. 2008 Jul; 29 (7): 1002–10.
9. Zhang C, Li C, Xu Z, Zhao S, Li P, Cao J, et al. The effect of surgical and psychological stress on learning and memory function in aged C57BL/6 mice. Neuroscience. 2016 Apr 21; 320: 210–20.
10. Hu X, Xu G. Does anesthesia cause postoperative cognitive decline. Med Princ Pract. 2016; 25 (5): 497.
11. Li XM, Li F, Liu ZK, Shao MT. Investigation of one-lung ventilation postoperative cognitive dysfunction and regional cerebral oxygen saturation relations. J Zhejiang Univ Sci B. 2015 Dec; 16 (12): 1042–8.
12. Papadopoulos G, Karanikolas M, Liarmakopoulou A, Papathanakos G, Korre M, Beris A. Cerebral oximetry and cognitive dysfunction in elderly patients undergoing surgery for hip fractures: a prospective observational study. Open Orthop J. 2012; 6: 400–5.
13. Li XM, Shao MT, Wang JJ, Wang YL. Relationship between post-operative cognitive dysfunction and regional cerebral oxygen saturation and β-amyloid protein. J Zhejiang Univ Sci B. 2014 Oct; 15 (10): 870–8.
14. Hong SW, Shim JK, Choi YS, Kim DH, Chang BC, Kwak YL. Prediction of cognitive dysfunction and patients' outcome following valvular heart surgery and the role of cerebral oximetry. Eur J Cardiothorac Surg. 2008 Apr; 33 (4): 560–5.
15. de Tournay-Jetté E, Dupuis G, Bherer L, Deschamps A, Cartier R, Denault A. The relationship between cerebral oxygen saturation changes and postoperative cognitive dysfunction in elderly patients after coronary artery bypass graft surgery. J Cardiothorac Vasc Anesth. 2011 Feb; 25 (1): 95–104.
16. Ni C, Xu T, Li N, Tian Y, Han Y, Xue Q, et al. Cerebral oxygen saturation after multiple perioperative influential factors predicts the occurrence of postoperative cognitive dysfunction. BMC Anesthesiol. 2015 Oct 26; 15: 156.
17. Xu JH, Zhang TZ, Peng XF, Jin CJ, Zhou J, Zhang YN. Effects of sevoflurane before cardiopulmonary bypass on cerebral oxygen balance and early postoperative cognitive dysfunction. Neurol Sci. 2013 Dec; 34 (12): 2123–9.
18. Choi JW, JooAhn H, Yang M, Kim JA, Lee SM, Ahn JH. Comparison Between Phenylephrine and Dopamine in Maintaining Cerebral Oxygen Saturation in Thoracic Surgery: A Randomized Controlled Trial. Medicine (Baltimore). 2015 Dec; 94 (49): 2212.
19. Kim SY, Chae DW, Chun YM, Jeong KH, Park K, Han DW. Modelling of the Effect of End-Tidal Carbon Dioxide on Cerebral Oxygen Saturation in Beach Chair Position under General Anaesthesia. Basic Clin Pharmacol Toxicol. 2016 Jul; 119 (1): 85–92.
20. Salazar D, Sears BW, Aghdasi B, Only A, Francois A, Tonino P, et al. Cerebral desaturation events during shoulder arthroscopy in the beach chair position: patient risk factors and neurocognitive effects. J Shoulder Elbow Surg. 2013 Sep; 22 (9): 1228–35.
21. Deiner S, Chu I, Mahanian M, Lin HM, Hecht AC, Silverstein JH. Prone position is associated with mild cerebral oxygen desaturation in elderly surgical patients. PLoS One. 2014 Sep 12; 9 (9): e106387.
22. American Society of Anesthesiologists. New classification of physical status. Anesthesiology. 1963; 24: 111.
23. Sykes MK, Vickers MD, Hull CJ. Principles of measurement and monitoring in anaesthesia and intensive care. 3rd ed. Oxford: Blackwell; 1991. 372 p.
24. Reitan RM. The relation of the trail making test to organic brain damage. J Consult Psychol. 1955 Oct; 19 (5): 393–4.
25. Folstein MF, Folstein SE, McHugh PR. "Mini-mental state". A practical method for grading the cognitive state of patients for the clinician. J Psychiatr Res. 1975 Nov; 12 (3): 189–98.
26. Julayanont P, Tangwongchai S, Hemrungrojn S, Tunvirachaisa-kul C, Phanthumchinda K, Hongsawat J, et al. The Montreal Cognitive Assessment-Basic: A Screening Tool for Mild Cognitive Impairment in Illiterate and Low-Educated Elderly Adults. J Am Geriatr Soc. 2015 Dec; 63 (12): 2550–4.
27. Ozgen ZS, Toraman F, Erkek E, Sungur T, Guclu P, Durmaz S, et al. Cesarean under general or epidural anesthesia: does it differ in terms of regional cerebral oxygenation? Acta Anaesthesiol Taiwan. 2014 Dec; 52 (4): 159–62.
28. Kermany MP, Soltani MH, Ahmadi K, Motiee H, Rubenzadeh S, Nejati V. The impact of anesthetic techniques on cognitive functions after urological surgery. Middle East J Anaesthesiol. 2015 Feb; 23 (1): 35–42.
29. Silbert BS, Evered LA, Scott DA. Incidence of postoperative cognitive dysfunction after general or spinal anaesthesia for extracorporeal shock wave lithotripsy. Br J Anaesth. 2014 Nov; 113 (5): 784–91.
30. Closhen D, Engelhard K, Dette F, Werner C, Schramm P. Changes in cerebral oxygen saturation following prone positioning for orthopaedic surgery under general anaesthesia: a prospective observational study. Eur J Anaesthesiol. 2015 Jun; 32 (6): 381–6.
31. Rasmussen LS, Jonson T, Kuipers HM. Does anesthesia case postoperative cognitive disfunction? A randomized study of regional versus general anesthesia in 438 elderly patients. Acta Anaesthesiol Scand. 2003; 47: 1188–94.
32. Casati A, Aldegheri G, Vinciguerra F. Randomized comparison between sevofluraneanaesthesia and unilateral spinal anaesthesia in elderly patients undergoing orthopaedic surgery. Eur J Anaesth. 2003; 20: 640–6.
33. Crul BJ, Hulstijn W, Burger IC. Influence of the type of anaesthesia on post-operative subjective physical well-being and mental function in elderly patients. Acta Anaesthesiol Scand. 1992; 36: 615–20.
34. Aun CS, McBride C, Lee A, Lau AS, Chung RC, Yeung CK, et al. Short-Term Changes in Postoperative Cognitive Function in Children Aged 5 to 12 Years Undergoing General Anesthesia: A Cohort Study. Medicine (Baltimore). 2016 Apr; 95 (14): e3250.
35. Mayr NP, Hapfelmeier A, Martin K, Kurz A, van der Starre P, Babik B, et al. Comparison of sedation and general anaesthesia for transcatheter aortic valve implantation on cerebral oxygen saturation and neurocognitive outcome. Br J Anaesth. 2016 Jan; 116 (1): 90–9.

Литература

1. Соленкова А. А., Бондаренко А. А., Лубнин А. Ю., Дзюбанова Н. А. Послеоперационные когнитивные изменения у больных пожилого и старческого возраста. Анестезиология и реаниматология. 2012; 4: 13–9.

2. Newman S, Stygall J, Hirani S, Shaefi S, Maze M. Postoperative cognitive dysfunction after noncardiac surgery: a systematic review. Anesthesiology. 2007 Mar; 106 (3): 572–90.
3. Dijkstra JB, Houx PJ, Jolles J. Cognition after major surgery in the elderly: test performance and complaints. Br J Anaesth. 1999 Jun; 82 (6): 867–74.
4. Berger M, Nadler JW, Browndyke J, Terrando N, Ponnusamy V, Cohen HJ, et al. Postoperative Cognitive Dysfunction: Minding the Gaps in Our Knowledge of a Common Postoperative Complication in the Elderly. Anesthesiol Clin. 2015 Sep; 33 (3): 517–50.
5. Monk TG, Price CC. Postoperative cognitive disorders. Curr Opin Crit Care. 2011 Aug; 17 (4): 376–81.
6. Newfield P. Postoperative cognitive dysfunction. F1000 Med Rep. 2009 Feb 24; 1: 14.
7. Monk TG, Weldon BC, Garvan CW, Dede DE, van der Aa MT, Heilman KM, et al. Predictors of cognitive dysfunction after major noncardiac surgery. Anesthesiology. 2008 Jan; 108 (1): 18–30.
8. Bianchi SL, Tran T, Liu C, Lin S, Li Y, Keller JM, et al. Brain and behavior changes in 12-month-old Tg2576 and nontransgenic mice exposed to anesthetics. Neurobiol Aging. 2008 Jul; 29 (7): 1002–10.
9. Zhang C, Li C, Xu Z, Zhao S, Li P, Cao J, et al. The effect of surgical and psychological stress on learning and memory function in aged C57BL/6 mice. Neuroscience. 2016 Apr 21; 320: 210–20.
10. Hu X, Xu G. Does anesthesia cause postoperative cognitive decline. Med Princ Pract. 2016; 25 (5): 497.
11. Li XM, Li F, Liu ZK, Shao MT. Investigation of one-lung ventilation postoperative cognitive dysfunction and regional cerebral oxygen saturation relations. J Zhejiang Univ Sci B. 2015 Dec; 16 (12): 1042–8.
12. Papadopoulos G, Karanikolas M, Liarmakopoulou A, Papathanakos G, Korre M, Beris A. Cerebral oximetry and cognitive dysfunction in elderly patients undergoing surgery for hip fractures: a prospective observational study. Open Orthop J. 2012; 6: 400–5.
13. Li XM, Shao MT, Wang JJ, Wang YL. Relationship between post-operative cognitive dysfunction and regional cerebral oxygen saturation and β-amyloid protein. J Zhejiang Univ Sci B. 2014 Oct; 15 (10): 870–8.
14. Hong SW, Shim JK, Choi YS, Kim DH, Chang BC, Kwak YL. Prediction of cognitive dysfunction and patients' outcome following valvular heart surgery and the role of cerebral oximetry. Eur J Cardiothorac Surg. 2008 Apr; 33 (4): 560–5.
15. de Tournay-Jetté E, Dupuis G, Bherer L, Deschamps A, Cartier R, Denault A. The relationship between cerebral oxygen saturation changes and postoperative cognitive dysfunction in elderly patients after coronary artery bypass graft surgery. J Cardiothorac Vasc Anesth. 2011 Feb; 25 (1): 95–104.
16. Ni C, Xu T, Li N, Tian Y, Han Y, Xue Q, et al. Cerebral oxygen saturation after multiple perioperative influential factors predicts the occurrence of postoperative cognitive dysfunction. BMC Anesthesiol. 2015 Oct 26; 15: 156.
17. Xu JH, Zhang TZ, Peng XF, Jin CJ, Zhou J, Zhang YN. Effects of sevoflurane before cardiopulmonary bypass on cerebral oxygen balance and early postoperative cognitive dysfunction. Neurol Sci. 2013 Dec; 34 (12): 2123–9.
18. Choi JW, JooAhn H, Yang M, Kim JA, Lee SM, Ahn JH. Comparison Between Phenylephrine and Dopamine in Maintaining Cerebral Oxygen Saturation in Thoracic Surgery: A Randomized Controlled Trial. Medicine (Baltimore). 2015 Dec; 94 (49): 2212.
19. Kim SY, Chae DW, Chun YM, Jeong KH, Park K, Han DW. Modelling of the Effect of End-Tidal Carbon Dioxide on Cerebral Oxygen Saturation in Beach Chair Position under General Anaesthesia. Basic Clin Pharmacol Toxicol. 2016 Jul; 119 (1): 85–92.
20. Salazar D, Sears BW, Aghdasi B, Only A, Francois A, Tonino P, et al. Cerebral desaturation events during shoulder arthroscopy in the beach chair position: patient risk factors and neurocognitive effects. J Shoulder Elbow Surg. 2013 Sep; 22 (9): 1228–35.
21. Deiner S, Chu I, Mahanian M, Lin HM, Hecht AC, Silverstein JH. Prone position is associated with mild cerebral oxygen desaturation in elderly surgical patients. PLoS One. 2014 Sep 12; 9 (9): e106387.
22. American Society of Anesthesiologists. New classification of physical status. Anesthesiology. 1963; 24: 111.
23. Sykes MK, Vickers MD, Hull CJ. Principles of measurement and monitoring in anaesthesia and intensive care. 3rd ed. Oxford: Blackwell; 1991. 372 p.
24. Reitan RM. The relation of the trail making test to organic brain damage. J Consult Psychol. 1955 Oct; 19 (5): 393–4.
25. Folstein MF, Folstein SE, McHugh PR. "Mini-mental state". A practical method for grading the cognitive state of patients for the clinician. J Psychiatr Res. 1975 Nov; 12 (3): 189–98.
26. Julayanont P, Tangwongchai S, Hemrungrojn S, Tunvirachaisa-kul C, Phanthumchinda K, Hongsawat J, et al. The Montreal Cognitive Assessment-Basic: A Screening Tool for Mild Cognitive Impairment in Illiterate and Low-Educated Elderly Adults. J Am Geriatr Soc. 2015 Dec; 63 (12): 2550–4.
27. Ozgen ZS, Toraman F, Erkek E, Sungur T, Guclu P, Durmaz S, et al. Cesarean under general or epidural anesthesia: does it differ in terms of regional cerebral oxygenation? Acta Anaesthesiol Taiwan. 2014 Dec; 52 (4): 159–62.
28. Kermany MP, Soltani MH, Ahmadi K, Motiee H, Rubenzadeh S, Nejati V. The impact of anesthetic techniques on cognitive functions after urological surgery. Middle East J Anaesthesiol. 2015 Feb; 23 (1): 35–42.
29. Silbert BS, Evered LA, Scott DA. Incidence of postoperative cognitive dysfunction after general or spinal anaesthesia for extracorporeal shock wave lithotripsy. Br J Anaesth. 2014 Nov; 113 (5): 784–91.
30. Closhen D, Engelhard K, Dette F, Werner C, Schramm P. Changes in cerebral oxygen saturation following prone positioning for orthopaedic surgery under general anaesthesia: a prospective observational study. Eur J Anaesthesiol. 2015 Jun; 32 (6): 381–6.
31. Rasmussen LS, Jonson T, Kuipers HM. Does anesthesia case postoperative cognitive disfunction? A randomized study of regional versus general anesthesia in 438 elderly patients. Acta Anaesthesiol Scand. 2003; 47: 1188–94.
32. Casati A, Aldegheri G, Vinciguerra F. Randomized comparison between sevofluraneanaesthesia and unilateral spinal anaesthesia in elderly patients undergoing orthopaedic surgery. Eur J Anaesth. 2003; 20: 640–6.
33. Crul BJ, Hulstijn W, Burger IC. Influence of the type of anaesthesia on post-operative subjective physical well-being and mental function in elderly patients. Acta Anaesthesiol Scand. 1992; 36: 615–20.
34. Aun CS, McBride C, Lee A, Lau AS, Chung RC, Yeung CK, et al. Short-Term Changes in Postoperative Cognitive Function in Children Aged 5 to 12 Years Undergoing General Anesthesia: A Cohort Study. Medicine (Baltimore). 2016 Apr; 95 (14): e3250.
35. Mayr NP, Hapfelmeier A, Martin K, Kurz A, van der Starre P, Babik B, et al. Comparison of sedation and general anaesthesia for transcatheter aortic valve implantation on cerebral oxygen saturation and neurocognitive outcome. Br J Anaesth. 2016 Jan; 116 (1): 90–9.

USING DIFFERENT DURAPLASTY VARIANTS IN THE TREATMENT OF PATIENTS WITH CHIARI MALFORMATION TYPE I

Kakhkharov RA[1]✉, Flegontov AN[1], Mokhov NV[1,2]

[1] Department of Neurology and Neurosurgery, Faculty of Advanced Training and Professional Retraining, Kazan State Medical University, Kazan, Russia

[2] Interregional Clinical Diagnostic Center, Kazan, Russia

The emergence of modern neuroimaging techniques has allowed for effective identification of patients with Chiari malformation. It is now possible to create a more accurate picture of this anomaly. Different surgical treatments can now be developed but this has led to standardization issues and lack of uniform recommendations for treatment of patients with Chiari malformation. A study conducted by the authors found that surgery involving the opening of the dura mater and subsequent plastic reconstruction by autoplastic graft was the optimal surgery option (with respect to volume of surgical treatment of such patients).

Keywords: Chiari malformation, Arnold–Chiari malformation, dura mater, aseptic meningitis

Acknowledgement: authors thank professor Valery Danilov from Kazan State Medical University for his help in preparing the manuscript.

✉ **Correspondence should be addressed:** Ruslan Kakhkharov
ul. Karbysheva, d. 12a, Kazan, Russia, 420097; ruslan.kahharov@mail.ru

Received: 10.06.2016 **Accepted:** 01.08.2016

ОПЫТ ИСПОЛЬЗОВАНИЯ РАЗЛИЧНЫХ ВАРИАНТОВ ПЛАСТИКИ ТВЕРДОЙ МОЗГОВОЙ ОБОЛОЧКИ В ЛЕЧЕНИИ БОЛЬНЫХ С АНОМАЛИЕЙ (МАЛЬФОРМАЦИЕЙ) КИАРИ I ТИПА

Р. А. Каххаров[1]✉, А. Н. Флегонтов[1], Н. В. Мохов[1,2]

[1] Кафедра неврологии и нейрохирургии ФПК и ППС, Казанский государственный медицинский университет, Казань

[2] Межрегиональный клинико-диагностический центр, Казань

Появление современных методов нейровизуализации позволило эффективно выявлять пациентов с аномалией Киари, сформировать более точную картину аномалии. Возникла возможность развития различных методов хирургического лечения, что в настоящее время приводит к проблемам стандартизации, а также отсутствию единых рекомендаций в лечении пациентов с мальформацией Киари. По результатам проведенного авторами исследования, оптимальной по объему хирургического лечения подобных пациентов была операция со вскрытием твердой мозговой оболочки и последующей ее пластикой аутотрансплантатом.

Ключевые слова: мальформация Киари, аномалия Арнольда–Киари, твердая мозговая оболочка, асептический менингит

Благодарности: профессору Валерию Данилову из Казанского государственного медицинского университета за помощь в подготовке рукописи.

✉ **Для корреспонденции:** Каххаров Руслан Абдуллаевич
420097, г. Казань, ул. Карбышева, д. 12а; ruslan.kahharov@mail.ru

Статья поступила: 10.06.2016 **Статья принята к печати:** 01.08.2016

Chiari malformation is often a congenital defect, characterized by displacement of the cerebellar tonsils below the level of the foramen magnum. This leads to chronic craniovertebral junction compression, blocks the normal flow of cerebrospinal fluid (CSF) and disrupts normal blood circulation in this area (fig. 1) [1, 2].

There are currently 6 types of Chiari malformations (table) [1, 3–6]. The most common are types I and II malformations: type I is observed in 3.3–8.2 cases per 1,000 people, while type II is found in 1–2 cases per 1,000 people [1, 7].

Surgery is the main method of treatment when indicated (syringomyelia and progression of clinical symptoms).

In 1932, Van Houweninge Graftidijk reported the first attempts at surgical correction of this deformity. He tried to restore normal CSF flow at the level of the deformity by resecting the tongue of redundant tissue or by resecting the bone over the posterior surface of the malformation and incising the underlying dura. The treatment did not produce positive results [8–10]. In 1938, Penfield and Coburn described a surgical technique involving resection of the lower part of the cerebellar tonsils at this anomaly [11]. With the emergence of the Gardner and Williams concepts, surgical treatment of syringomyelia (fig. 2) and Chiari malformation became theoretically justified. The name Gardner (or "basic technique")

Types of Chiari malformations

Types	Diagnostic criteria
I	Displacement of the cerebellar tonsils below the level of the foramen magnum by more than 5 mm or presence of spinal cord syringomyelia with displacement of the cerebellar tonsils below the level of the foramen magnum by more than 2 mm
II	The cerebellar tonsils, cerebellar vermis, fourth ventricle and the medulla oblongata shift downward through the spinal canal
III	The contents of the posterior cranial fossa descend into the meningeal sac located in the occipital bone defect
IV	Cerebellar hypoplasia without shift. This Chiari malformation type is not accompanied by herniation of the CNS structures, so it is often not included in conventional classification
0	Cerebellar tonsils fill the entire cisterna magna but do not go beyond it. It is characterized by "overflowing" of the posterior cranial fossa
1,5	Cerebellar tonsillar dystopia, small stretching of the fourth ventricle and brain stem (possible slight flattening or crimping) by minimal changes from oral spinal cord sections. It is a transitional (boundary) type between types I and II, which combines features of both types of deformities, or embryologically incomplete Type II without concomitant myelodysplasia

was given to the surgery procedure described by them for correction of syringomyelia in Chiari malformation in 1965. This surgery technique is used in various modifications to this day. The operation involves suboccipital resection trepanation, anterior cervical laminectomy, dissection of arachnoid adhesions, readjustment of the foramen of Magendie and closure of the entrance to the central canal of the spinal cord with a muscle slice. The surgery involves alignment of the CSF flow pressure at the level of the craniovertebral junction [12, 13].

Currently, Gardner's surgery — in its classical form — is performed rarely. The proposed modifications for this surgery are performed in two ways. The first type is resection trepanation of the posterior cranial fossa, dissection of the dura mater and arachnoid mater with or without resection of the cerebellar tonsils with or without cisterna magna reconstruction. The second type is resection trepanation of the posterior cranial fossa with the opening of the dura mater and manipulations on it [14–17].

There are also other surgery types: Endoscopic third ventriculostomy (ETV), transoral decompression and craniovertebral decompression with occipitospondylodesis [5].

Performance of ETV as a first stage in the treatment of patients with Chiari malformation type I (CM-I) and concomitant hydrocephalus is currently recognized as the gold standard, displacing the previously used shunt system. According to researchers [6], the procedure is up to 95 % effective. There is a small group of CM patients suffering directly from intracranial hypertension symptoms for whom surgical treatment can be limited to only ETV [6]. However, craniovertebral junction compression is subsequently required for most patients with Chiari malformation and concomitant hydrocephalus.

Transoral decompression in CM patients should be used in cases of severe anterior compression and basilar invagination. Most scientists believe that given the injury rate of this method, it is reasonable to use the standard craniovertebral decompression with a one-time stabilizing surgery as the first stage of surgical treatment for patients with a combination of anterior and posterior compressions [18].

One-time performance of craniovertebral decompression and stabilizing surgery is indicated in a relatively small group of patients with CM-I, atlantoaxial dislocation and high risk of cervical spine instability revealed at the pre-surgical examination stage. The provoking factors for spinal instability in patients with CM-I are disruption of neck muscle innervation amidst syringomyelic cysts in the upper cervical level, muscular fibrosis repeating their compression and stretching and improper surgical wound closure [18, 19].

Fig. 1. A T1-weighted sagittal MRI scan, from a patient with Chiari malformation, cerebellar tonsillar prolapse

Fig. 2. A T1-weighted sagittal MRI scan. Syringomyelia — disorder often associated with Chiari malformation

The purpose of the surgery is to decompress the craniovertebral junction in order to free the flow of CSF and blood circulation at this level by easing CSF outflow from the foramen of Magendie and cisterna magna to the spinal subarachnoid space.

There are a number of post-op complications in duraplasty. In our study, we decided to focus on two main complications – aseptic meningitis and pseudomeningocele.

Aseptic meningitis is an inflammatory response by the meninges. It differs from purulent postoperative meningitis by the absence of pyogenic pathogen diagnosed through microscopic examination. This syndrome has a characteristic clinical picture (pyrexia, meningeal symptom, inflammatory changes in the blood and cerebrospinal fluid), which is not significantly different from that of purulent postoperative meningitis. Aseptic meningitis syndrome is accompanied by immunologic phenomena of transient postoperative reactive inflammation associated with lymphocyte activation [20].

Pseudomeningocele is a pathological extradural accumulation of cerebrospinal fluid in the soft tissues, communicating with the subdural space through the dura mater defect (Fig. 3).

There are also a number of other post-operative complications: accumulation of lamellar subdural hygroma in the cerebellar hemisphere, pneumocephalus and arachnoiditis. The patient's sitting position during surgery also leads to such intraoperative complications as air embolism.

Research objective: To determine the role of duraplasty in Chiari malformation surgeries.

Tasks:

– to ascertain the incidence of various clinical symptoms in Chiari malformations;

– to assess the incidence of post-op complications depending on the surgical technique;

– to assess the response to surgical treatment under various duraplasty techniques.

METHODS

The study included 34 patients with Chiari malformations. They were treated at the neurosurgical department of Interregional Clinical and Diagnostic Center in Kazan from 2010 to 2014.

Clinical method, preoperative brain imaging, direct intraoperative imaging and retrospective analysis were all deployed for the study.

All the patients underwent neurological examination in the preoperative and early postoperative periods. The basic neurological functions were assessed.

Preoperative imaging consisted of brain MRI (capturing the craniovertebral junction) and spine MRI along the length depending on the syringomyelia level. MRI scan was performed using the Signa HDxt 1.5T magnetic resonance scanner (General Electric, USA) with at least 1.5 T magnetic field intensity in the axial, sagittal and coronal projections, as well as in hydrography regime to assess the CSF flow dynamics in the craniovertebral junction.

The main criteria for Chiari malformation diagnosis were neuroimaging data (fig. 4) [21–23] and clinical examination based on identification of specific clinical syndromes (cerebellar, hypertension-hydrocephalic, syringomyelic, radicular, bulbar and vertebrobasilar insufficiency syndromes [24]). In most CM-I cases, MRI revealed descent of the cerebellar tonsils below the McRae line, syringomyelia and brain stem compression. In Chiari Malformation type II (CM-II), descent of the cerebellar tonsils, Z-shaped deformation of the medulla oblongata, quadrigeminal adhesion (beak-shaped bend in the quadrigemina), medulla elongation and low brain attachment were also detected. In CM-II cases, MRI revealed hydrocephalus, syringomyelia in the craniovertebral junction, isolated fourth ventricle, cerebellar-medullary compression, and agenesis/ dysgenesis of the corpus callosum [5].

The average age of the patients was 45 years (from 18 to 69 years). The ratio between number of men and female was 1 : 3.2 respectively. It is worth noting that the most common surgical procedure was performed in patients aged 50–60 years. Neurological symptom progression was the indication for surgery.

The surgery procedures were carried out in a sitting position. The soft tissue was dissected according to Naffziger-Towne method (Babchin's modification). In the next step, the lower parts of the squamous part of occipital bone were resected, C1 laminectomy and sometimes C2 was carried out. All the patients were divided into two groups based on the extent of further intervention.

The first group included 8 (23.5 %) patients, whose dura mater was not opened. In this case, distinct pulsation of dura mater could be seen.

The second group had 26 (76.5 %) patients, whose dura mater was opened with a Y-shaped incision. In most cases, the dura mater turned out to be thickened and it did not pulse. Venous sinuses expanded quite often. After dissection of the dura mater, the level of descent of the cerebellar tonsils and subarachnoid space was examined and assessed. In the case of pronounced adhesions, the subarachnoid space was readjusted with release from adhesions of vessels, medulla and cerebellar tonsils. Next, duraplasty was performed to restore the integrity of the dura mater. The second group was divided into two subgroups depending on the type of duraplasty performed:

– 2A: 14 (41.2 %) patients — the dura mater was opened followed by allograft duraplasty surgery. Artificial dura mater DURAFORM (Codman Neuro, USA) was used as the allograft.

– 2B: 12 (35.3 %) patients — the dura mater was opened

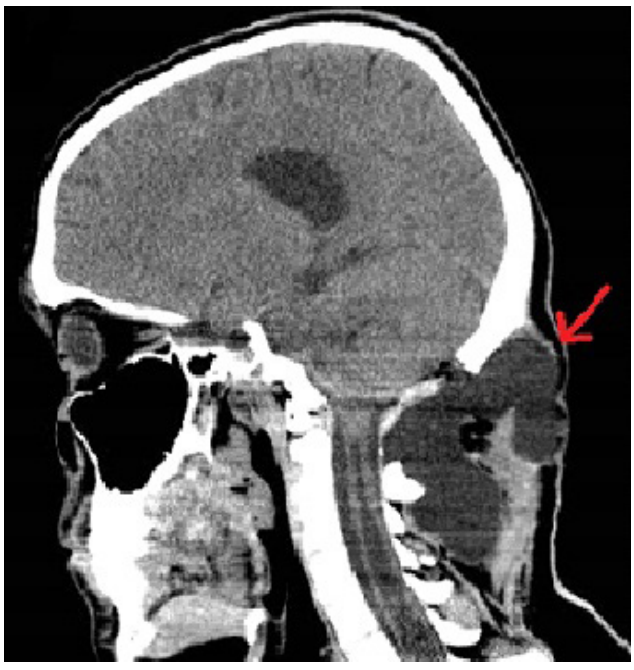

Fig. 3. A sagittal CT scan. Pseudomeningocele (marked by arrow) — one of the post-op complications from Chiari malformation surgery

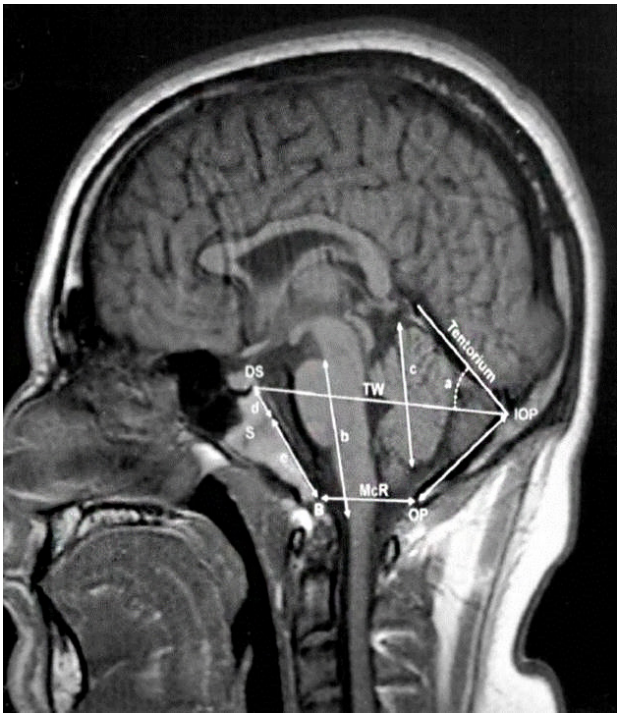

Fig. 4. Reference points of the posterior fossa used in diagnosis of Chiari malformation (Sekula et al., 2005 [21])

d + e — length of clivus; S — sphenooccipital synchondrosis; d — length of basisphenoid between the top of the dorsum sellae and the sphenooccipital synchondrosis of the clivus; e — length of the basiocciput between the synchondrosis and the basion; b — length of the hindbrain between the midbrain-pons junction and the medullocervical junction; a — angle of the cerebellar tentorium to Twining's line; c — length of cerebellar hemispheres; DS — top of the dorsum sellae; IOP — internal occipital protuberance; OP — opisthion; IOP to OP — length of supraocciput; B — basion; TW — Twining's line; McR (B to OP) — McRae's line.

followed by allograft duraplasty surgery. A previously marked occipitalis muscle aponeurosis served as the allograft. On the access point, the soft tissues were dissected up to the occipitalis muscle aponeurosis. The aponeurosis was cut off as a 3 × 5 cm flap, and leaned back to the side. The base of the flap was directed towards the occipitalis muscle. Thus, the aponeurosis flap remained on the pedicle via which it was supplied with necessary nutrients till the end of the operation. Afterwards, dissection was carried out linearly like in other groups. At the duraplasty stage, the pedicle was cut off, and the flap was sutured to the edges of the opened dura mater. So the cisterna magna was increased, which resulted in more craniovertebral junction decompression.

Resection of the cerebellar tonsils was not performed in any of the patients.

Response to surgery in the early postoperative period was analyzed. During comparison, neurological regression, incidence of postoperative complications resulting from duraplasty inefficiency, and dependence on duraplasty technique were first factored in.

Statistical data analysis was performed using Microsoft Office Excel 2010.

RESULTS

Analysis of the medical records of patients with Chiari malformation revealed the incidence of neurological syndromes identified during preoperative clinical examination (fig. 5). Cerebellar syndrome was detected in majority of the cases (88.2 %). Bulbar syndrome and vertebrobasilar insufficiency syndrome were the least observed (in less than half of the patients).

Clinical method and postoperative brain imaging were used in analyzing the response to surgical treatment. Neurological examination took into account regression of the characteristic clinical symptom, whose presence criterion included the following: no complaints from the patient, sensitivity improvement under the corresponding dermatitis and increase in strength in the limbs, reduction in cerebellar symptoms and signs of intracranial hypertension.

Response to treatment was assessed in the early and late post-op periods. After full treatment, all the patients showed a positive response to treatment.

Hypertension-hydrocephalic syndrome regressed faster than others. Within the first days after surgery, characteristic neurological symptoms of intracranial hypertension disappeared in the patients. Within 3–4 months, there was complete or partial disappearance of bulbar, cerebellar and syringomyelic syndromes. Restoration of sensitivity and muscle strength was observed. MRI scans showed that syringomyelic cysts disappeared within 6 months to 1 year.

The following results were obtained (fig. 6).

In the group of patients who underwent craniovertebral junction decompression followed by duraplasty, neurological syndromes regressed in 21 (80.8 %) out of the 26 patients within the first 20 days of surgery: in the first subgroup with allograft duraplasty surgery — in 11 (79 %) out of 14 patients; in the second subgroup with allograft duraplasty surgery — in 10 (83 %) out of 12 patients.

A time limit of 20 days was chosen arbitrarily according to the results obtained from data study.

In the group of patients who underwent craniovertebral junction decompression transition without opening of the dura mater, regression of neurological syndromes in 75 % of cases occurred no earlier than one month from the date of the surgery. In 2 (25 %) out of 8 patients, the main syndromes regressed within the first 20 days.

Post-op complications associated with inefficiency of duraplasty — aseptic meningitis and pseudomeningocele — were found only in patients who underwent craniovertebral junction decompression with the opening of dura mater and subsequent allograft duraplasty surgery (42.9 %). Moreover, of all the patients from this subgroup (n = 14), aseptic meningitis was observed in 5 (35.7 %) patients in the postoperative period, and pseudomeningocele in 1 (7.1 %) patient.

In the subgroup of patients who underwent craniovertebral junction decompression with the opening of dura mater and subsequent allograft duraplasty surgery, the above-mentioned post-operative complications were not observed.

DISCUSSION

Identifying an efficient surgical correction method and standardizing this method is an important task since surgery is the primary treatment for patients with this deformity. However, the decision on extent of surgery in some cases cannot be standardized, and any addition to the main surgery procedure should be determined intraoperatively. The main goal of surgery is to decompress the craniovertebral junction and restore normal flow of cerebrospinal fluid in the area.

In a number of cases, bone decompression is enough to achieve the surgery target. This is evidenced by a clear pulsation of the dura mater, but the sole criterion cannot provide the required reliability. Therefore, we believe that somatosensory evoked potentials should be used intraoperatively. This method

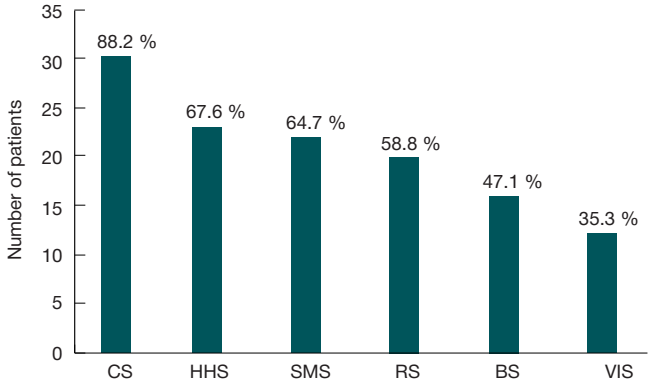

Fig. 5. Incidence of syndromes in Chiari malformationMC — мозжечковый синдром

CS — cerebellar syndrome; HHS — hypertension-hydrocephalic syndrome; SMS — syringomyelic syndrome; RS — radicular syndrome; BS — bulbar syndrome; VIS — vertebrobasilar insufficiency syndrome.

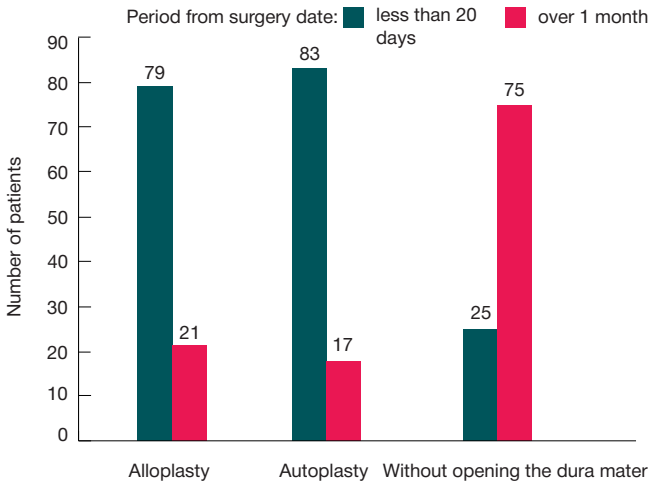

Fig. 6. Duration of neurological syndrome regression under different types of surgery

gives fairly accurate information on possible post-operative regression. The evidence of this includes intraoperative results obtained by us, namely the positive dynamics in 2 out of 8 patients who did not undergo opening of the dura mater. These 2 patients from the first group showed the fastest regression of neurological symptoms.

Our study found that surgery with the opening of the dura mater and subsequent allograft duraplasty surgery is the most optimal extent of surgical treatment of type 1 Chiari malformation. This finding is consistent with the data from world literature [25–27].

CONCLUSIONS

Based on the outcome of surgical treatment of patients with Chiari malformation type I, it can be concluded that craniovertebral junction decompression with the opening of the dura mater and subsequent sealing with autograft is an effective method for surgical treatment of patients with this deformity. This method reduces the risk of post-op complications. The relative majority of patients with the most rapid regression of neurological symptoms serve as a proof that this method is effective.

References

1. Vishnevskii AA, Shuleshova NV. Spinnoi mozg. [Klinicheskie i patofiziologicheskie sopostavleniya]. St. Petersburg: Foliant; 2014. 744 p. Russian.
2. Cahan LD, Bentson JR. Considerations in the diagnosis and treatment of syringomyelia and the Chiari malformation. J Neurosurg. 1982 Jul; 57 (1): 24–31.
3. Mozhaev SV, Skoromets AA, Skoromets TA. Neirokhirurgiya. St. Petersburg: Izdatel'stvo "Politekhnika"; 2001. 355 p. Russian.
4. Reutov AA, Karnaukhov VV. Klinicheskie rekomendatsii po khirurgicheskomu lecheniyu mal'formatsii Kiari u vzroslykh. Klinicheskie rekomendatsii obsuzhdeny i utverzhdeny na Plenume Pravleniya Assotsiatsii neirokhirurgov Rossii; 2015 Apr 16; St. Petersburg. Moscow: Association of Neurosurgeons of Russia; 2015. Russian.
5. Greenberg MS, Arredondo N. Handbook of Neurosurgery. 6th ed. Lakeland, FL, New York: Greenberg Graphics, Thieme Medical Publishers; 2006. 1016 p.
6. Reutov AA. Printsipy diagnostiki i taktika khirurgicheskogo lecheniya bol'nykh s mal'formatsiei Kiari I tipa [dissertation abstract]. Moscow: N N Burdenko Scientific Research Neurosurgery Institute; 2012. Russian.
7. Anikandrov AB, Korelyakova AG. Klinika i diagnostika siringobul'bii i opukholei stvola golovnogo mozga. In: X Vsesoyuznaya konferentsiya molodykh neirokhirurgov; 1974; Kaluga, Russia. Conference proceedings. Vol. 1, Novoe v klinike, diagnostike i lechenii razlichnykh vidov neirokhirurgicheskoi patologii. Moscow; 1974. p. 22–5. Russian.
8. Dzyak LA, Zorin NA, Egorov VF, Cherednichenko YuV. Mal'formatsiya Arnol'da–Kiari: klassifikatsiya, etiopatogenez, klinika, diagnostika (obzor literatury). Ukrainskii neirokhirurgicheskii zhurnal. 2001; (1): 17–23. Russian.
9. Kakhramanov SV. [Chiari malformation]. Zh Vopr Neirokhir Im N N Burdenko. 2005 Jul–Sep; (3): 36–9. Russian.
10. Bejjani GK. Definition of the adult Chiari malformation: a brief historical overview. Neurosurg Focus. 2001 Jul 15; 11 (1): 1–8.
11. Penfield W, Coburn DF. Arnold–Chiari malformation and its operative treatment. Arch Neurol Psychiatry. 1938; 40: 328–36.
12. Larionov SN, Sorokovikov VA. Printsipy rekonstruktivnoi khirurgii mal'formatsii Kiari u detei. In: Materialy II Vserossiiskoi konferentsii po detskoi neirokhirurgii; 2007 Jun 27–29; Yekaterinburg, Russia. Yekaterinburg; 2007. p. 101. Russian.
13. Sevost'yanov DV. Differentsirovannyi podkhod k khirurgicheskomu lecheniyu bol'nykh mal'formatsiei Kiari I tipa [dissertation]. Novosibirsk: NNIITO; 2013. Russian.
14. Oldfield EH, Muraszko K, Shawker TH, Patronas NJ. Pathophysiology of syringomyelia associated with Chiari I malformation of the cerebellar tonsils. Implications for diagnosis and treatment. J Neurosurg. 1994 Jan; 80 (1): 3–15.
15. Mozhaev SV, Sterlikova NV, Skoromets AA, Kostyukevich AV. Operativnoe lechenie anomalii Kiari I tipa. Neirokhirurgiya. 2007; (1): 14–8. Russian.
16. Blagodatskii MD. Khirurgicheskoe lechenie soobshchayushcheisya formy siringomielii. Vopr Neirokhir. 1985; (2): 20–2. Russian.
17. Blagodatskii MD, Larionov SN. Rezul'taty lecheniya progressiruyushchikh form siringomielii. Vopr Neirokhir. 1993; (2): 8–10. Russian.
18. Nishikawa M, Ohata K, Baba M, Terakawa Y, Hara M. Chiari I malformation associated with ventral compression and instability: one-stage posterior decompression and fusion with a new instrumentation technique. Neurosurgery. 2004 Jul; 54 (6): 1430–4; discussion 1434–5.
19. Hurlbert RJ, Crawford NR, Choi WG, Dickman CA. A biomechanical evaluation of occipitocervical instrumentation: screw compared with wire fixation. J Neurosurg. 1999 Jan; 90 (1 Suppl): 84–90.

20. Nemirovskii AM. Sindrom asepticheskogo meningita u bol'nykh s opukholyami golovnogo mozga v rannem posleoperatsionnom periode [dissertation]. St. Petersburg: Rossiiskii nauchno-issledovatel'skii neirokhirurgicheskii institut imeni professora A. L. Polenova; 2008. Russian.
21. Sekula RF Jr, Jannetta PJ, Casey KF, Marchan EM, Sekula LK, McCrady CS. Dimensions of the posterior fossa in patients symptomatic for Chiari I malformation but without cerebellar tonsillar descent. Cerebrospinal Fluid Res. 2005 Dec 18; 2: 1–11.
22. Garland EM, Anderson JC, Black BK, Kessler RM, Konrad PE, Robertson D. No increased herniation of the cerebellar tonsils in a group of patients with orthostatic intolerance. Clin Auton Res. 2002 Dec; 12 (6): 472–6. doi: 10.1007/s10286-002-0051-9.
23. Karagöz F, Izgi N, Kapíjcíjoğlu Sencer S. Morphometric measurements of the cranium in patients with Chiari type I malformation and comparison with the normal population. Acta Neurochir (Wien). 2002 Feb; 144 (2): 165–71; discussion 171. doi: 10.1007/s007010200020.
24. Golubev VL, Vein AM. Nevrologicheskie sindromy. Rukovodstvo dlya vrachei. Moscow: Eidos Media; 2002. 832 p. Russian.
25. Bikmullin TA, Bariev ER, Anisimov VI. Sravnitel'nyi analiz razlichnykh metodov khirurgicheskogo lecheniya anomalii Arnol'da–Kiari. Prakticheskaya meditsina. 2015; 4 (89): 28–30. Russian.
26. Slyn'ko EI, Verbv VV, Pastushin AI, Ermolaev AA. Rezul'taty khirurgicheskogo lecheniya anomalii Kiari u vzroslykh. Ukrainskii neirokhirurgicheskii zhurnal. 2006; (2): 77–89. Russian.
27. Mutchnick IS, Janjua RM, Moeller K, Moriarty TM. Decompression of Chiari malformation with and without duraplasty: morbidity versus recurrence. J Neurosurg Pediatr. 2010 May; 5 (5): 474–8.

Литература

1. Вишневский А. А., Шулешова Н. В. Спинной мозг. Клинические и патофизиологические сопоставления. СПб.: Фолиант; 2014. 744 с.
2. Cahan LD, Bentson JR. Considerations in the diagnosis and treatment of syringomyelia and the Chiari malformation. J Neurosurg. 1982 Jul; 57 (1): 24–31.
3. Можаев С. В., Скоромец А. А., Скоромец Т. А. Нейрохирургия. СПб.: Издательство «Политехника»; 2001. 355 с.
4. Реутов А. А., Карнаухов В. В. Клинические рекомендации по хирургическому лечению мальформации Киари у взрослых. Клинические рекомендации обсуждены и утверждены на Пленуме Правления Ассоциации нейрохирургов России, г. Санкт-Петербург, 16.04.2015. М.: Ассоциации нейрохирургов России; 2015.
5. Greenberg MS, Arredondo N. Handbook of Neurosurgery. 6th ed. Lakeland, FL, New York: Greenberg Graphics, Thieme Medical Publishers; 2006. 1016 p.
6. Реутов А. А. Принципы диагностики и тактика хирургического лечения больных с мальформацией Киари I типа [автореф. дисс.]. М.: НИИ нейрохирургии им. акад. Н. Н. Бурденко; 2012.
7. Аникандров А. Б., Корелякова А. Г. Клиника и диагностика сирингобульбии и опухолей ствола головного мозга. В кн.: X Всесоюзная конференция молодых нейрохирургов; 1974; Калуга. Тезисы докладов. Т. 1, Новое в клинике, диагностике и лечении различных видов нейрохирургической патологии. М.: [б. и.]; 1974. с. 22–5.
8. Дзяк Л. А., Зорин Н. А., Егоров В. Ф., Чередниченко Ю. В. Мальформация Арнольда–Киари: классификация, этиопатогенез, клиника, диагностика (обзор литературы). Укр. нейрохир. журн. 2001; (1): 17–23.
9. Кахраманов С. В. Мальформация Киари I типа. Журн. Вопр. нейрохир. 2005; (3): 36–9.
10. Bejjani GK. Definition of the adult Chiari malformation: a brief historical overview. Neurosurg Focus. 2001 Jul 15; 11 (1): 1–8.
11. Penfield W, Coburn DF. Arnold–Chiari malformation and its operative treatment. Arch Neurol Psychiatry. 1938; 40: 328–36.
12. Ларионов С. Н., Сороковиков В. А. Принципы реконструктивной хирургии мальформации Киари у детей. В кн.: Материалы II Всероссийской конференции по детской нейрохирургии; 27–29 июня 2007 г.; Екатеринбург. Екатеринбург; 2007. с. 101.
13. Севостьянов Д. В. Дифференцированный подход к хирургическому лечению больных мальформацией Киари I типа [диссертация]. Новосибирск: ННИИТО; 2013.
14. Oldfield EH, Muraszko K, Shawker TH, Patronas NJ. Pathophysiology of syringomyelia associated with Chiari I malformation of the cerebellar tonsils. Implications for diagnosis and treatment. J Neurosurg. 1994 Jan; 80 (1): 3–15.
15. Можаев С. В., Стерликова Н. В., Скоромец А. А., Костюкевич А. В. Оперативное лечение аномалии Киари I типа. Нейрохирургия. 2007; (1): 14–8.
16. Благодатский М. Д. Хирургическое лечение сообщающейся формы сирингомиелии. Вопр. нейрохир. 1985; (2): 20–2.
17. Благодатский М. Д., Ларионов С. Н. Результаты лечения прогрессирующих форм сирингомиелии. Вопр. нейрохир. 1993; (2): 8–10.
18. Nishikawa M, Ohata K, Baba M, Terakawa Y, Hara M. Chiari I malformation associated with ventral compression and instability: one-stage posterior decompression and fusion with a new instrumentation technique. Neurosurgery. 2004 Jul; 54 (6): 1430–4; discussion 1434–5.
19. Hurlbert RJ, Crawford NR, Choi WG, Dickman CA. A biomechanical evaluation of occipitocervical instrumentation: screw compared with wire fixation. J Neurosurg. 1999 Jan; 90 (1 Suppl): 84–90.
20. Немировский А. М. Синдром асептического менингита у больных с опухолями головного мозга в раннем послеоперационном периоде [диссертация]. СПб: РНХИ им. проф. А. Л. Поленова; 2008.
21. Sekula RF Jr, Jannetta PJ, Casey KF, Marchan EM, Sekula LK, McCrady CS. Dimensions of the posterior fossa in patients symptomatic for Chiari I malformation but without cerebellar tonsillar descent. Cerebrospinal Fluid Res. 2005 Dec 18; 2: 1–11.
22. Garland EM, Anderson JC, Black BK, Kessler RM, Konrad PE, Robertson D. No increased herniation of the cerebellar tonsils in a group of patients with orthostatic intolerance. Clin Auton Res. 2002 Dec; 12 (6): 472–6. doi: 10.1007/s10286-002-0051-9.
23. Karagöz F, Izgi N, Kapíjcíjoğlu Sencer S. Morphometric measurements of the cranium in patients with Chiari type I malformation and comparison with the normal population. Acta Neurochir (Wien). 2002 Feb; 144 (2): 165–71; discussion 171. doi: 10.1007/s007010200020.
24. Голубев В. Л., Вейн А. М. Неврологические синдромы. Руководство для врачей. М.: Эйдос Медиа; 2002. 832 с.
25. Бикмуллин Т. А., Бариев Э. Р., Анисимов В. И. Сравнительный анализ различных методов хирургического лечения аномалии Арнольда–Киари. Практ. мед. 2015; 4 (89): 28–30.
26. Слынько Е. И., Вербв В. В., Пастушин А. И., Ермолаев А. А. Результаты хирургического лечения аномалии Киари у взрослых. Укр. нейрохир. журн. 2006; (2): 77–89.
27. Mutchnick IS, Janjua RM, Moeller K, Moriarty TM. Decompression of Chiari malformation with and without duraplasty: morbidity versus recurrence. J Neurosurg Pediatr. 2010 May; 5 (5): 474–8.

TROPHIC CHANGES IN THE SKELETAL MUSCLES OF RATS AFTER THERAPY WITH SILDENAFIL AND CEREBROLYSIN IN THE LOWER LIMB ISCHEMIA MODEL

Belous AS[1,2], Biryukova YuK[1], Zatolokina MA[2], Lavrinenko KI[2], Loyko EA[2] ✉, Mal GS[2], Shevelev AB[1], Trubnikova EV[1]

[1] Research Laboratory "Genetics",
Kursk State University, Kursk

[2] Kursk State Medical University, Kursk

For many patients with lower limb ischemia, surgical treatment is not beneficial. We have studied the efficacy of combination therapy with sildenafil (Viagra) by Pfizer, France, and cerebrolysin (Ever Neuro Pharma, Austria) for lower limb ischemia in the Wistar rat model. The animals were divided into 6 groups (20 rats each): intact animals; sham-operated animals; rats with ischemia and no treatment administered (controls); rats with ischemia who received a 28-day monotherapy with sildenafil (2.2 mg/kg orally); rats with ischemia who received a 28-day monotherapy with 0.005 ml cerebrolysin; rats with ischemia who received a combination therapy with 2.2. mg/kg sildenafil for 7 days and 0.005 ml i. m. cerebrolysin for 10 days. Microcirculation in shin muscles was evaluated on days 21 and 28 of the experiment. On the same days, rats were overdosed with anesthetics and sacrificed in tens. Then, histological sections of shin muscles were prepared. Regional blood flow was significantly higher ($p < 0.05$) in three experimental groups, compared to the controls; however, the combination therapy was far more effective than monotherapy, regardless of the medication used. Macroscopically, the muscles of the animals included into the experimental groups did not differ from the muscles of the intact animals; microscopically, no necrotic lesions were observed in the experimental groups that were typical for the ischemized rats who had received no treatment. Neovascularization was also observed in the experimental groups.

Keywords: lower limb ischemia, ischemia treatment, sildenafil, cerebrolysin, pharmacotherapy, combination therapy

Acknowledgements: authors thank professor Victor Lazarenko (Kursk State Medical University) and professor Alexandr Khudin (Kursk State University) for providing research facilities for the experiment.

✉ **Correspondence should be addressed:** Ekaterina Loyko
19 Stepnoy pereulok, d. 14, Kursk, Russia, 305025; katryn.moon@yandex.ru

Received: 20.08.2016 **Accepted:** 27.08.2016

ТРОФИЧЕСКИЕ ИЗМЕНЕНИЯ СКЕЛЕТНОЙ МУСКУЛАТУРЫ КРЫС ПОСЛЕ ФАРМАКОТЕРАПИИ СИЛДЕНАФИЛОМ И ЦЕРЕБРОЛИЗИНОМ ПРИ МОДЕЛИРОВАНИИ ИШЕМИИ НИЖНИХ КОНЕЧНОСТЕЙ

А. С. Белоус[1,2], Ю. К. Бирюкова[1], М. А. Затолокина[2], К. И. Лавриненко[2], Е. А. Лойко[2] ✉, Г. С. Маль[2], А. Б. Шевелев[1], Е. В. Трубникова[1]

[1] Научно-исследовательская лаборатория «Генетика»,
Курский государственный университет, Курск

[2] Курский государственный медицинский университет, Курск

Ишемия нижних конечностей — заболевание, в большом числе случаев не поддающееся хирургическому лечению. Нами была исследована эффективность комбинированной фармакотерапии силденафилом (Viagra, Pfizer, Франция) и «Церебролизином» (EVER Neuro Pharma, Австрия). Ишемию мышц голени моделировали на крысах линии Wistar. Сформировали 6 групп животных по 20 особей: интактные; ложнооперированные; с ишемией и без лечения (контрольная группа); с ишемией и монотерапией силденафилом (перорально 2,2 мг/кг в течение 28 дней); с ишемией и монотерапией «Церебролизином» (внутримышечно 0,005 мл в течение 20 дней); с ишемией и комбинированной терапией (силденафил — перорально 2,2 мг/кг в течение 7 дней, «Церебролизин» — внутримышечно 0,005 мл в течение 10 дней). Измеряли уровень микроциркуляции крови в мышцах голени на 21-е и 28-е сутки. В эти же сроки выводили из эксперимента путем передозировки наркоза по 10 животных и готовили гистологические препараты мышц голени. Уровень регионарного кровотока достоверно ($p < 0,05$) повышался в трех опытных группах по сравнению с контрольной, однако при этом комбинированная терапия была значительно эффективнее монотерапии независимо от препарата. Макроскопически мышцы животных опытных групп не отличались от мышц интактных животных, микроскопически — наблюдалось отсутствие некротических участков, характерных для ишемизированных мышц крыс, не получавших лечения, а также новообразование сосудов.

Ключевые слова: ишемия нижних конечностей, коррекция ишемии, силденафил, церебролизин, фармакотерапия, комбинированная терапия, ФДЭ-5

Благодарности: профессору Виктору Лазаренко из Курского государственного медицинского университета и профессору Александру Худину из Курского государственного университета за возможность выполнения эксперимента на базе научно-исследовательских лабораторий их университетов.

✉ **Для корреспонденции:** Лойко Екатерина Анатольевна
305025, г. Курск, 19-ый Степной переулок, д. 14; katryn.moon@yandex.ru

Статья поступила: 20.08.2016 **Статья принята к печати:** 27.08.2016

Lower limb ischemia is a chronic arterial occlusion occurring in the legs caused by atherosclerosis, obliterating endarteritis and diabetes [1, 2]. Operative techniques used for its treatment include surgery through skin incisions (shunting and endarterectomy) and various minimally invasive interventions (X-ray-controlled angioplasty and stenting) that restore arterial patency in case the artery is totally blocked or improve blood flow if the blockage is incomplete. However, surgery can be recommended for half of patients only [3–6].

A solution to this problem is drug therapy. The most effective medication for treating critical limb ischemia is Vasaprostan by UCB Pharma, Germany; its active ingredient is alprostadil, a synthetic analogue of natural prostaglandin E1. However, it does not work as a vasodilator that typically widens blood vessels and improves peripheral circulation; Vasaprostan induces changes in blood biochemistry when circulating in blood for a long time [7].

There are a number of medications that affect lipid exchange, peripheral vascular beds and rheological properties of blood, but they do not eliminate vasospasm, a key factor in the progression of critical limb ischemia. Hopes are raised by a new class of drugs that facilitate vasodilation using the effect of endogenous nitric oxide (NO); the latter is produced by nerve endings and endothelial cells and intensifies synthesis of intracellular alarmone, namely, cyclic guanosine monophosphate (cGMP). The same effect can be achieved by using sildenafil, a phosphodiesterase type 5 inhibitor (PDE5) and a cGMP-hydrolizing enzyme [1, 2, 8–10].

There has been a growing interest in Cerebrolysin (EVER Neuro Pharma, Austria), a drug used to treat stroke, Alzheimer disease and traumas to the brain. It was shown to reduce enzymatic activity of superoxide dismutase and catalase, which are two basic enzymes activated through oxidative stress. However, Cerebrolysin works indirectly by reducing production of superoxide anion and hydrogen peroxide that are substrates for the above mentioned enzymes. Besides, Cerebrolysin was shown to inhibit formation of hydroxyl radicals [11–13]. Also, studies *in vitro* and *in vivo* demonstrated that the drug inhibits calpain activity by 60 %, which means that fewer cells undergo apoptosis [14].

The aim of this work was to assess efficacy of lower limb ischemia therapy with sildenafil (Viagra, Pfizer, France) and Cerebrolysin in a mouse model.

METHODS

The experiment was carried out in pre-quarantined Wistar rats (age of 4 months, weight of 230–260 g) provided by the Research Institute of Ecological Medicine of Kursk State Medical University. For this study, healthy animals were selected. They were kept in a standard experimental biological cleanroom at 22–24 °C under 12 : 12 cyclic lighting conditions. All rats received food pellets and filtered tap water. Procedures were performed at a fixed time in the afternoon. Anesthesia was performed intra-abdominally using 300 mg/kg of chloral hydrate aqueous solution; animals were sacrificed by its overdose. The experiment was carried out in accordance with the European Convention for the Protection of Vertebrate Animals used for Experimental and Other Scientific Purposes (Strasburg, 1986).

To allocate animals to different groups, stratified randomization was used. Stratification factors were body weight and procedures performed on the animals. The following groups were formed:

1) intact animals (n = 20),
2) sham-operated animals (n = 20),
3) animals with crural muscle ischemia who received no treatment (the control group, n = 20),
4) animals with crural muscle ischemia who received sildenafil (n = 20),
5) animals with crural muscle ischemia who received Cerebrolysin (n = 20),
6) animals with crural muscle ischemia who received sildenafil and Cerebrolysin (n = 20).

The group of sham-operated animals was formed of rats that had been incised lengthwise on the inner thigh under anesthesia, their neurovascular bundle was isolated and the incision was then closed by continuous sutures.

Ischemia of crural muscles was modeled in anesthetized animals in the supine position. The hair on the inner thigh was accurately removed; the skin was washed with 70 % surgical spirit. The incision was done on the inner thigh lengthwise. Elements of the thigh neurovascular bundle were isolated. The artery was separated from the vein and the nerve, a ligature was applied to its upper section where *arteria saphena*, an analogue of deep femoral artery in humans, branches off (under inguinal ligament) [15]. *A. saphena* was ligated and transected. The popliteal artery and upper crural arteries (anterior and posterior tibial arteries) were isolated and transected without ligation. Then, femoral artery was transected 3 mm below the previously applied ligature. The section of the magistral vessel including the femoral and popliteal arteries and upper anterior and posterior crural arteries was removed. No retrograde bleeding from crural arteries was observed. The wound was closed by a continuous suture [16].

The animals from groups 4 and 6 were administered 2.2 mg/kg sildenafil citrate per os for 28 and 7 days, respectively. The animals from groups 5 and 6 received i. m. injections of 0.005 ml Cerebrolysin for 20 and 10 days, respectively [17]. Blood microcirculation in crural muscles was assessed on days 21 and 28 of the experiment using MP100 data acquisition system in LDF 100C laser Doppler flowmetry mode (LDF) and TSD144 needle probe for invasive measurements (all by Biopac Systems, USA). LDF data were recorded and processed using Acqknowledge 3.8.1 software (Biopac Systems); microcirculation was measured in perfusion units (PU). To build a microcirculation curve, data from five different regions of the muscle were recorded for 30 s at each point: the middle point of the muscle longitudinal axis, two points 3–5 mm above it and below, a more lateral and a more medial point with regard to the first point.

The animals were sacrificed in tens by anesthetic overdose on days 21 and 28 of the experiment. In each case, autopsy was performed and crural muscle slices were prepared. Samples for histological analysis were fixed in 10 % formalin for 7 days. Paraffin blocks and microsections were prepared using a standard technique. Slices were stained with hematoxylin, eosin and Van Gieson's stain, and then studied with the Levenhuk 320 microscope (Levenhuk, USA). For morphological analysis, sections were imaged using Levenhuk C310 digital camera and ScopeTek ScopePhoto 3.1.268 software (Hangzhou Scopetek Opto-Electronic Co., China). Using 4 × 20 × 6 magnification, quantitative changes in the vessels were studied within the field of view.

Considering reports on compensatory restoration of regional blood flow in the model selected for this study, we concluded that the most comprehensive data were obtained on day 28 of the experiment. Data obtained on day 21 were considered interim [18].

Statistical processing was done using Microsoft Excel 10.0. Mean values (M) and standard error of mean (m) were

calculated. To compare measurement values obtained from different groups and to determine if differences between them were significant, we used a two-sample t-test with variances. Differences were considered significant with $p < 0.05$.

RESULTS

The mean perfusion value in the crural muscles of the intact animals on day 21 of the experiment was 527 ± 13 PU. Histological analysis revealed densely packed bundles of monocytes, with plethoric venules and arterioles inside containing very few erythrocytes. Lumens were wide; no degrading changes in endothelial cells were observed (fig. A).

In the group of sham-operated animals, mean perfusion value did not differ significantly from that of the intact group, and was 519 ± 13 PU on day 21 of the experiment ($p = 0.66$) and 521 ± 16 PU on day 28 of the experiment ($p = 0.77$). No difference in tissue morphology was detected (fig. B).

In the group of animals with untreated crural muscle ischemia, mean perfusion values were significantly lower, compared to the group of intact animals: 325 ± 3 PU on day 21 of the experiment ($p < 0.05$) and 371 ± 2 PU on day 28 of the experiment ($p < 0.05$). On day 21 damaged muscles were swollen, with large grey and brown patches. Histological analysis showed that those were necrotic foci with resorbed necrotic fibers and proliferating granulation tissue. On day 28, the color went back to normal, but the muscles still looked hypotrophic. Areas of resorbed necrotic tissue were considerably smaller. Formation of individual capillaries and vascular plethora were observed in the microcirculatory bed. There were patches of atrophied muscle fibers close to the necrotic foci (fig. C).

Sildenafil contributed to a statistically significant increase in regional blood flow to the ischemized crural muscles, compared to group 3: perfusion was 425 ± 4 PU on day 21 ($p < 0.05$) and 803 ± 10 PU on day 28 ($p < 0.05$). Perfusion values in group 4 on day 21 were close to those in the group

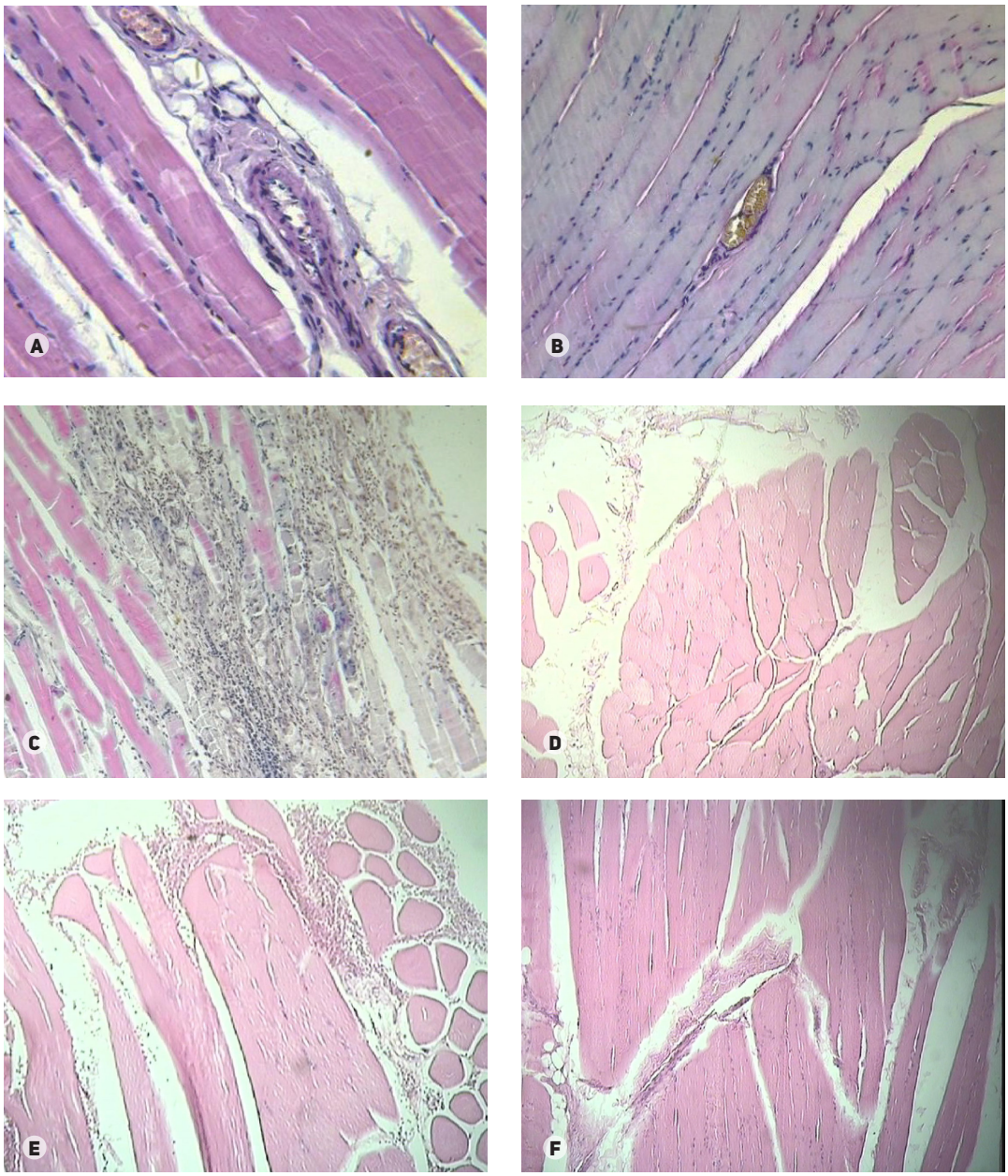

Morphological analysis of rat crural muscles. **(A)** Intact rats. **(B)** Sham-operated rats (group 2). **(C)** Controls. **(D)** Rats treated with sildenafil (group 4). **(E)** Rats treated with Cerebrolysin (group 5). **(F)** Rats treated with sildenafil and Cerebrolysin (group 6). Staining: hematoxylin and eosin, ×140

of intact animals; on day 28 they were considerably higher. Macroscopically, ischemized muscles did not differ in color or appearance from the muscles of the intact rats. No necrotic changes were detected by microscopy, but we observed rare patches of atrophic myocytes and cell proliferation (fig. D).

In the group of animals with crural muscle ischemia treated with Cerebrolysin, a statistically significant increase in perfusion was observed, compared to group 3: 429 ± 12 PU on day 21 ($p < 0.05$) and 767 ± 8 PU on day 28 ($p < 0.05$). On day 21, we noticed grey and brown patches — large necrotic foci with resorbed necrotic fibers and proliferating granulation tissue. On day 28 ischemized muscles did not differ in color or appearance from the muscles of the intact rats. Microscopy did not detect any necrotic changes in the. Formation of individual capillaries and vascular plethora were observed in the microcirculatory bed (fig. E).

In rats treated with a combination of sildenafil and Cerebrolysin, mean perfusion value was 754 ± 9 PU on day 21 ($p < 0.05$ compared to the control group); on day 28 it went up to 1004 ± 13 PU ($p < 0.05$). Morphologically, the muscles here did not differ from those treated with sildenafil (fig. F).

DISCUSSION

The obtained results indicate that both treatment types — a combination therapy of sildenafil and Cerebrolysin and monotherapy - significantly stimulate regional blood flow in rats with crural muscle ischemia. However, a combination therapy is more effective in stimulating formation of collateral blood vessels.

Sildenafil is a PDE5 inhibitor, an enzyme involved in different biochemical processes inside the cell. Over the past decades it has been discovered that PDE5 inhibitors can be used for treating various pathologies [19]. Sildenafil triggers a cascade that activates protein kinase C and elevates intracellular levels of cGMP in cardiomyocytes due to the activation of inducible and endothelial nitric oxide synthases. A resulting cardioprotective effect is mediated by the opening of mitochondrial ATP-sensitive potassium channels (mitoKATP-channels) [20]. The opening of mitoKATP-channels increases membrane potential of the myocardial cells and accelerates ATP synthesis and Ca^{2+} transport across the membrane. Smooth muscle cells relax, arterial lumens widen and blood flow increases [21].

It is the mitoKATP-channels that play a key role in the mechanism of anti-ischemic protection. They are found in many organs, including the vasculature. Their activity was first observed in sarcolemma (sarcKATP-channels) and then in mitochondria. In both cases, their activity is affected by physiological concentrations of ATP. The channels open when ATP concentration goes down significantly or the adenine nucleotide content decreases. Thus, the channels are a sensor of oxygen and glucose (ATP sources) supply. We think that cytoprotective effect of sildenafil can be explained by the activity of KATP-channels [21]. Perhaps, sildenofil also stimulates neoangiogenesis in the ischemized rat muscle. The evidence here is the results of LDF and the morphological analysis: on day 28 compensatory restoration occurred followed by the increase in regional blood flow to the ischemized muscles of the experimental animals caused by angiogenesis. Earlier we mentioned that Cerebrolysin inhibits enzymic activity of superoxide dismutase and catalase (antioxidative effect) and exhibits anti-apoptotic properties. Besides, the drug has an anti-inflammatory effect [22, 23]. Thus, Cerebrolysin facilitates sildenafil-induced stimulation of natural mechanisms of angiogenesis.

CONCLUSIONS

We have demonstrated high efficacy of a combination therapy with sildenafil and Cerebrolysin in rats with lower limb ischemia. Measured in perfusion units, perfusion in the ischemized muscles of experimental rats on day 28 was almost twice as high as in the control group.

References

1. Kirichenko AA, Novichkova N. Khronicheskaya ishemicheskaya bolezn' nog. Moscow; 1998. 24 p. Russian.
2. Pokrovsky MV, Kolesnik IM, Chodov SV, Intercession TG, Dolzhikov AA, Ephremenkova DA, et al., inventors; Kursk State Medical University, assignee. Sposob farmakologicheskoy korrektsii ishemii skeletnoy myshtsy sildenafilom, v tom chisle pri l-name-indutsirovannom defitsite oksida azota. Patent RU 2497203. 2013 Oct 27. Russian.
3. Knyazev VV. Mikroskopicheskoe issledovanie reparativnoy regeneratsii nervnykh volokon posle khimicheskoy desimpatizatsii. In: Universitetskaya nauka: Vzglyad v budushchee. Sbornik trudov 72 nauchnoy konferentsii KGMU i sessii Tsentral'no-Chernozemnogo nauchnogo tsentra RAMN. Rossiyskiy simpozium «Zakonomernosti integratsii fiziologicheskikh funktsiy v norme i ikh dezintegratsiya v patologii»; 2007 Feb 1–2; Kursk, Russia. Vol. 1. Kursk: KGMU; 2007. p. 116–9. Russian.
4. Kovalenko V, Kalitko I, Temrezov M, Chemurziev R, Petrov A. Vozmozhnosti lecheniya bol'nykh s aterotromboticheskim porazheniem arteriy nizhnikh konechnostey. Vrach. 2010; (3): 55–8. Russian.
5. Sepiashvili RI, Shubich MG, Karpyuk VB. Oksid azota pri astme i razlichnykh formakh immunopatologii. Astma. 2009; 2 (2): 5–14. Russian.
6. Chervyakov YuV, Staroverov IN, Nersisyan EG, Isaev AA, Deev RV. [Therapeutic angiogenesis in treatment of patients with chronic obliterating diseases of lower limb arteries]. Angiology and Vascular Surgery. 2012. 18 (3): 19–27. Russian.
7. Rowe VL, Lee W, Weaver FA, Etzioni D. Patterns of treatment for peripheral arterial disease in the United States: 1996–2005. J Vasc Surg. 2009 Apr; 49 (4): 910–7.
8. Gorchakov VD, Sergienko VI, Vladimirov VG. Selektivnye gemosorbenty. Moscow: Meditsina; 1989. 221 p. Russian.
9. Pokrovskaja TG, Chuljukova TN, Pokrovskii TV [Endothelioprotective effects of sildenafil and tadalafil at experimental model of the l-name-induced deficiency of nitric oxide]. Kubanskii nauchnyi meditsinskii vestnik. 2009. 4: 136–9. Russian.
10. Pokrovskaya TG, Chulyukova TN, Pokrovskiy MV, Filippenko NG. Endotelioprotektivnye dozozavisimye effekty sildenafila v kombinatsiyakh s L-argininom pri eksperimental'nom modelirovanii L-NAME-indutsirovannogo defitsita oksida azota. Biomedicine. 2010. 1 (5): 118–20. Russian.
11. Masliah E, Díez-Tejedor E. The pharmacology of neurotrophic treatment with Cerebrolysin: brain protection and repair to counteract pathologies of acute and chronic neurological disorders. Drugs Today (Barc.). 2012. 48 Suppl A: 3–24.
12. González ME, Francis L, Castellano O. Antioxidant systemic effect of short-term Cerebrolysin administration. J Neural Transm Suppl. 1998. 53: 333–41.
13. Sugita Y, Kondo T, Kanazawa A, Itou T, Mizuno Y. [Protective effect of FPF 1070 (cerebrolysin) on delayed neuronal death in the gerbil-detection of hydroxyl radicals with salicylic acid]. No To

Shinkei. 1993. 45 (4): 325–31. Japanese.
14. EVER Neuro Pharma. Cerebrolysin — product monograph. 2010. 84 p.
15. Gambaryan PP, Dukelskaya NM. Krysa. Moscow: Sovetskaya nauka; 1955. 254 p. Russian.
16. Artyushkova EB, Pashkov DV, Pokrovsky MV, Faitelson AV, Gudyrev OS, Pokrovskaya TG, et al. [Possibilities of pharmacological correction of experimental chronic limb ischemia]. Éksperimentalnaya i Klinicheskaya Farmakologiya. 2008; 71 (3): 23–5. Russian.
17. Young W, Keck WM. Tserebrolizin: obzor klinicheskikh i eksperimental'nykh issledovaniy. Prakticheskaya angiologiya [Internet]. 2009 [cited 2016 Sep 1]; 8 (27): [about 8 p.]. Available from: http://angiology.com.ua/ru-issue-article-273. Russian.
18. Kolesnik IM, Lasarenko VA Pokrovskiy MV. [The influence of pharmacological preconditioning with sildenafil and vardenafil on condition of microvasculature in the ischemic skeletal muscle]. Kursk Scientific and Practical Bulletin "Man and His Health". 2015; (1): 83–6. Russian.
19. Beyer S, Speich R, Fischler M, Maggiorini M, Ulrich S. Long-term experience with oral or inhaled vasodilator combination therapy in patients with pulmonary hypertension. Swiss Med Wkly. 2006 Feb 18; 136 (7–8): 114–8.
20. Das S, Maulik N, Das DK, Kadowitz PJ, Bivalacqua TJ. Cardioprotection with sildenafil, a selective inhibitor of cyclic 3',5'-monophosphate-specific phosphodiesterase 5. Drugs Exp Clin Res. 2002; 28 (6): 213–9.
21. Vertkin AL. Klinicheskaya farmakologiya ingibitorov FDE 5: vzglyad klinicheskogo farmakologa. Consilium medicum. 2004; 6 (7): 502–5. Russian.
22. Alvarez XA, Lombardi VR, Fernández-Novoa L, Garciá M, Sampedro C, Cagiao A, et al. Cerebrolysin reduces microglial activation in vivo and in vitro: a potential mechanism of neuroprotection. J Neural Transm. Suppl. 2000; 59: 281–92.
23. Lombardi VR, Windisch M, García M, Cacabelos R. Effects of Cerebrolysin on in vitro primary microglial and astrocyte rat cell cultures. Methods Find Exp Clin Pharmacol. 1999; 21 (5): 331–8.

Литература

1. Кириченко А. А., Новичкова Ю. Н. Хроническая ишемическая болезнь ног. М.; 1998. 24 с.
2. Покровский М. В., Колесник И. М., Ходов С. В., Покровская Т. Г., Должиков А. А., Ефременкова Д. А. и др., авторы; Курский государственный медицинский университет, патентообладатель. Способ фармакологической коррекции ишемии скелетной мышцы силденафилом, в том числе при l-name-индуцированном дефиците оксида азота. Патент РФ RU 2497203 от 27.10.2013.
3. Князев В. В. Микроскопическое исследование репаративной регенерации нервных волокон после химической десимпатизации. В сб.: Университетская наука: Взгляд в будущее. Сборник трудов 72-й научной конференции КГМУ и сессии Центрально-Черноземного научного центра РАМН. Российский симпозиум «Закономерности интеграции физиологических функций в норме и их дезинтеграция в патологии»; 1–2 февраля 2007 г.; Курск. Т. 1. Курск: КГМУ; 2007. с. 116–9.
4. Коваленко В., Калитко И., Темрезов М., Чемурзиев Р., Петров А. Возможности лечения больных с атеротромботическим поражением артерий нижних конечностей. Врач. 2010; (3): 55–8.
5. Сепиашвили Р. И., Шубич М. Г., Карпюк В. Б. Оксид азота при астме и различных формах иммунопатологии. Астма. 2009; 2 (2): 5–14.
6. Червяков Ю. В., Староверов И. Н., Нерсесян Е. Г., Исаев А. А., Деев Р. В. Терапевтический ангиогенез в лечении больных с хроническими облитерирующими заболеваниями артерий нижних конечностей. Ближайшие и отдаленные результаты. Ангиол. и сосуд. хир. 2012. 18 (3): 19–27.
7. Rowe VL, Lee W, Weaver FA, Etzioni D. Patterns of treatment for peripheral arterial disease in the United States: 1996–2005. J Vasc Surg. 2009 Apr; 49 (4): 910–7.
8. Горчаков В. Д., Сергиенко В. И., Владимиров В. Г. Селективные гемосорбенты. М.: Медицина: 1989. 221 с.
9. Покровская Т. Г., Чулюкова Т. Н., Покровский М. В. Эндотелиопротективные эффекты силденафила и тадалафила при экспериментальном моделировании L-NAME-индуцированного дефицита оксида азота. Кубанский науч. мед. вест. 2009. 4: 136–9.
10. Покровская Т. Г., Чулюкова Т. Н., Покровский М. В., Филиппенко Н. Г. Эндотелиопротективные дозоза- висимые эффекты силденафила в комбинациях с L-аргинином при экспериментальном моделировании L-NAME-индуцированного дефицита оксида азота. Биомедицина. 2010. 1 (5): 118–20.
11. Masliah E, Díez-Tejedor E. The pharmacology of neurotrophic treatment with Cerebrolysin: brain protection and repair to counteract pathologies of acute and chronic neurological disorders. Drugs Today (Barc.). 2012. 48 Suppl A: 3–24.
12. González ME, Francis L, Castellano O. Antioxidant systemic effect of short-term Cerebrolysin administration. J Neural Transm Suppl. 1998. 53: 333–41.
13. Sugita Y, Kondo T, Kanazawa A, Itou T, Mizuno Y. [Protective effect of FPF 1070 (cerebrolysin) on delayed neuronal death in the gerbil-detection of hydroxyl radicals with salicylic acid]. No To Shinkei. 1993. 45 (4): 325–31. Japanese.
14. EVER Neuro Pharma. Cerebrolysin — product monograph. 2010. 84 p.
15. Гамбарян П. П., Дукельская Н. М. Крыса. М.: Советская наука; 1955. 254 с.
16. Артюшкова Е. Б., Пашков Д. В., Покровский М. В., Файтельсон А. В., Гудырев О. С., Покровская Т. Г. и др. Возможности фармакологической коррекции хронической ишемии конечности в эксперименте. Экспер. и клин. фармакол. 2008; 71 (3): 23–5.
17. Young W, Keck WM. Церебролизин: обзор клинических и экспериментальных исследований. Практ. ангиол. [Интернет]. 2009 [дата обращения: 1 сентября 2016 г.]; 8 (27): [ок. 8 стр.]. Доступно по ссылке: http://angiology.com.ua/ru-issue-article-273.
18. Колесник И. М., Лазаренко В. А., Покровский М. В. Влияние фармакологического прекондиционирования силденафилом и варденафилом на состояние микроциркуляторного русла в ишемизированной скелетной мышце. Курский научно-практический вестник «Человек и его здоровье». 2015; (1): 83–6.
19. Beyer S, Speich R, Fischler M, Maggiorini M, Ulrich S. Long-term experience with oral or inhaled vasodilator combination therapy in patients with pulmonary hypertension. Swiss Med Wkly. 2006 Feb 18; 136 (7–8): 114–8.
20. Das S, Maulik N, Das DK, Kadowitz PJ, Bivalacqua TJ. Cardioprotection with sildenafil, a selective inhibitor of cyclic 3',5'-monophosphate-specific phosphodiesterase 5. Drugs Exp Clin Res. 2002; 28 (6): 213–9.
21. Верткин А. Л. Клиническая фармакология ингибиторов ФДЭ 5: взгляд клинического фармаколога. Consilium medicum. 2004; 6 (7): 502–5.
22. Alvarez XA, Lombardi VR, Fernández-Novoa L, Garciá M, Sampedro C, Cagiao A, et al. Cerebrolysin reduces microglial activation in vivo and in vitro: a potential mechanism of neuroprotection. J Neural Transm. Suppl. 2000; 59: 281–92.
23. Lombardi VR, Windisch M, García M, Cacabelos R. Effects of Cerebrolysin on in vitro primary microglial and astrocyte rat cell cultures. Methods Find Exp Clin Pharmacol. 1999; 21 (5): 331–8.